Towards deterministic heralded single photon sources at telecommunication wavelengths

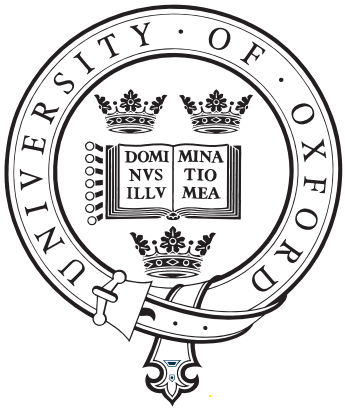

Submitted for the degree of Doctor of Philosophy
Trinity term 2018

Supervised by
Professor Ian A Walmsley

Clarendon Laboratory
University of Oxford
United Kingdom

First Published in 2018

Single Library Version

A catalogue record for this publication is probably available somewhere.

Reproduced from the author's mind and the stated references.

Printed and bound in Great Britain by a printer and a binder.

Towards deterministic heralded single photon sources at telecommunication wavelengths

Submitted for the degree of Doctor of Philosophy
Hilary Term 2018

Abstract

The field of optical quantum information processing uses and manipulates the state of light to implement computational tasks. Knill, Laflamme, and Milburn presented a scheme that allows computations in linear optical networks with only single photon sources, single photon detectors and feed forward control. This approach relies on the probabilistic interference of photons in pure states and requires many iterations to establish the result of a computation. It is therefore essential that photons are readily available to ensure a fast and efficient implementation of the scheme. Further to this, probabilistic photon-pair emission by parametric non-linear optical processes such as parametric down-conversion and four-wave mixing forms the basis of the most highly developed and common source of single photons. Due to the probabilistic nature of photon generation one must wait for a long time for multiple independent sources to simultaneously deliver photons to the experiment. This thesis focuses on approaches of generating heralded single photons with increased success probability.

The first part of this thesis presents a pulsed, heralded single photon source, with continuous frequency multiplexing, operating at telecommunication wavelengths. Multiplexing increases the probability of delivering a photon for each pump laser pulse without an addition of noise. We have studied the spectral characteristics and investigated the photon number statistics of the multiplexed source. Overall we have demonstrated an improvement by a factor of two in the probability of delivering a heralded photon, without a correspond-ing increase in the noise in the output mode in comparison to an equivalent single mode source. A Hong-Ou-Mandel interference measurement of the heralded photon provides an estimate of the purity $P = 61.3 \pm 4.4$ %. A theoretical model of the source was developed and shows good agreement with the measurements and indicates directions for possible future improvements.

In the second part we will discuss developments of a chip based spontaneous four-wave mixing source of heralded single photons in direct ultraviolet written waveguides in Silica-on-Silicon chips. We present the demonstration of photon-pair generation at telecommuni-cation wavelengths in these waveguides, made possible by increasing the waveguide birefrin-gence and operating with a pump field wavelength of $\sim$ 1064 nm. The performance of this novel source was characterised through measurements of the spectral properties and photon number statistics of the generated light. This will help to reveal new insights for future improvements to the source design.

Acknowledgements

There is no doubt that I owe thanks to many people, who enabled me to work on many research projects, who supported me during this endeavour and whose knowledge formed the base of my research.

I am grateful to my supervisor Ian Walmsley for giving me the chance to develop my knowledge of non-linear processes and single photon sources and for forming the inspiring group environment in which all of us explore new ideas and thoughts.

I want to thank Steve Kolthammer and Andreas Eckstein for their daily supervision and advice. Your help and insights inspired me and shaped my approach to experimental physics. You taught me how to progress with experiments and how to analyse and solve problems. I also thank you Andreas for all the software packages you wrote for the experiments, especially for the data acquisition of time stamps from various time taggers.

I want to thank Johannes, Peter and Mark for their contribution to the frequency multiplexed source. The multiplexed source would not be running without your ground work, the FPGA development, your ideas, and the initial testing. I also want to say thank you to Tom for all your critical questions, your help, and your insight into the theoretical model of the experiment. I look forward to continuing to work with you and to explore new improvements to the source set-up.

I also want to thank Matt and our collaborators at the Optoelectronics Research Centre of the University of Southampton for the close collaboration in optimising the FWM photon source chips.

Obviously, there are many other people I have not mentioned by name. Some of those are my fellow Ultrafast group members, friends and family who I want to thank for the company and support during my studies and work.

Contents

List of Figures

List of Tables

List of abbreviations

APD	Avalanche Photo-Diode
a.u.	Arbitrary units
B	Boron
BBO	Beta Barium Borate
CAR	Coincidence to Accidentals Ratio
cm	Centimetre
CW	Continuous-Wave
DAQ	Data Acquisition
dB	Decibel
DFG	Difference Frequency Generation
DUW	Direct UV-Writing
EDFA	Erbium-Doped Fibre Amplifier
EOM	Electro-Optical Modulator
FBG	Fibre Bragg Grating
FHD	Flame Hydrolysis Deposition
FPGA	Field-Programmable Gate Array
FWHM	Full Width at Half Maximum
FWM	Four-Wave Mixing
fs	Femtosecond
Ge	Germanium
GHz	Gigahertz
$g^{(2)}$	Second order correlation function

$g_{\mathrm{H}}^{(2)}$	Heralded second order correlation function
HOM	Hong, Ou, and Mandel
HSPS	Heralded Single Photon Source
Hz	Hertz
InGaAs	Indium Gallium Arsenide
JSA	Joint Spectral Amplitude
JSI	Joint Spectral Intensity
KDP	Potassium Dihydrogen Phosphate
kHz	Kilohertz
KLM	Knill, Laflamme, and Milburn
KTP	Potassium Titanyl Phosphate
LASER	Light Amplification by Stimulated Emission of Radiation
LN	Lithium Niobate
LOQC	Linear Optical Quantum Computing
LUT	Lookup-Table
LVTTL	Low Voltage Transistor-Transistor Logic
m	Metre
MHz	Megahertz
mm	Millimetre
μm	Micrometre
μs	Microsecond
μW	Microwatt
mW	Milliwatt
NIM	Nuclear Instrumentation Module
nm	Nanometre
ns	Nanosecond
NV	Nitrogen-Vacancy
Ω	Ohm

OPA Optical Parametric Amplifier

OSA Optical Spectrum Analyser

P Phosporus

PBS Polarising Beam Splitter

PC Personal Computer

PDC Parametric Down-Conversion

PM Polarisation-Maintaining

ps Picosecond

QD Quantum Dot

RF Radio Frequency

s Second

SHG Second-Harmonic Generation

Si Silicon

SiO_2 Silica

SiV Silicon-vacancy

SNSPD Superconducting Nanowire Single Photon Detector

SPDC Spontaneous Parametric Down-Conversion

SVD Singular Value Decomposition

TDC Time to Digital Converter

TES Transition-Edge Sensor

THz Terahertz

Ti:Sapphire Titanium Sapphire

TMSV Two-Mode Squeezed Vacuum

TOF Time of Flight

TTL Transistor-Transistor Logic

UV Ultraviolet

V Volt

vac. Vacuum

W Watt

WSi Tungsten Silicide

List of symbols

$\chi^{(n)}$	n-th order electric susceptibility
ϵ_0	Vacuum permittivity
∞	Infinity
$\|vac.\rangle$	Vacuum state
$\hbar$	Reduced Planck constant
c_0	Speed of light in vacuum
$c.c.$	Complex conjugate
$h.c.$	Hermitian conjugate
$\mathbb{1}$	Identity operator
n	Index of refraction
T_0	Melting point
V_π	Voltage applied to an EOM which induces a π phase shift on an optical field.

Chapter 1

Introduction

In 1982 R Feynman discussed the simulation of physics with computers [1]. Feynman realised, that a classical computer can not simulate physical systems, which are described by quantum mechanics, because an excessively large amount of resources would be required. He therefore proposed a new universal simulator capable of simulating such systems which also uses quantum mechanics, a quantum computer. D Deutsch followed this idea and established a formal definition of a universal quantum computer [2].

A computer based on a more general theory than classical mechanics, such as quantum mechanics, has new capabilities of solving tasks. It is therefore expected, that this machine outperforms a classical computer in some tasks. Deutsch already realised that a quantum computer can execute some tasks faster than a classical computer. P Shore [3] and L Grover [4] presented in 1994 and 1996 algorithms for quantum computers which demonstrate this capability for the computation of discrete logarithms and factoring as well as database searches.

In 2000, D DiVincenzo established a set of requirements that a system needs to meet to

be sufficient to build a quantum computer[5]. These requirements are:

1. “that the physical system is scalable with well characterized qubits”
2. “that the qubit has to be initialized in a specific state”
3. “that the decoherence times are much longer than the gate operation time”
4. “that a universal set of quantum gates can be implemented”
5. “that the qubit can be read out”

He also listed two further requirements for quantum communication, which are the requirement for converting stationary qubits into flying qubits and vice versa as well as the requirement to reliably transmit flying qubits between distinct locations. Many different platforms are capable of satisfying these requirements[6–13] and basic operations have been demonstrated in various systems such as:

- atoms[14–16],
- atomic ensembles[17–20],
- ions[21–23],
- nuclear magnetic resonance[24–27],
- defects in crystal lattices such as Nitrogen-Vacancy (NV) or other colour centres in diamond[28–30],
- photons[31–39],
- quantum dots[40–42],

- solid state systems and doped crystals [43–47],
- superconducting devices [48].

The variety of platforms is astonishing and no single superior one has yet emerged.

Any implementation has to ensure that it is isolated from the environment to unveil the necessary quantum effects. This often requires vacuum systems, magnetic and electric shielding, and cooling to cryogenic temperatures. Light fields in quantum optics are in this aspect unique, since the background in our environment does not require any additional shielding. A thermal photon at room temperature has an energy of $\sim 10^{-21}$ J which is much lower than the energy of a photon in the visible spectral range, or around 1550 nm which is $\sim 10^{-19}$ J. The black body radiation only becomes significant at temperatures beyond 1000°C thus, at normal conditions, optically-based experiments remain unperturbed if housed in a simple enclosure. This facilitates many experimental implementation in quantum optics.

In 2001 Knill, Laflamme, and Milburn (KLM) introduced a scheme that enables quantum computations with linear optical networks, single photon sources, single photon detectors, and feed forward control [49]. With this scheme all-optical quantum computation is possible and all of the requirements posed by DiVincenzo are satisfied. Approaches based on optical qubits can also meet the two additional requirements for quantum communication. This thesis investigates one component necessary for the KLM scheme, the photon source.

1.1 The generation of single photons

The invention and demonstration of the maser [50] in 1955, shortly followed by the realisation of the laser [51] in 1960, opened up many new possibilities to study the properties of light. Amongst others, the field of non-linear optics profited greatly by the availability of intense coherent light fields [52–54]. Notably, for this thesis, is also the observation of photon number correlations in Parametric Down-Conversion (PDC) in 1970 [55] and the generation of a Two-Mode Squeezed Vacuum (TMSV) state.

Since then, many different approaches to photon generation have been developed, which we will discuss in the following sections. These approaches can be grouped into two classes, the deterministic single photon emitters and the spontaneous single photon emitters. For any type of photon source we can impose some general requirements. First of all single photons have to be emitted from such a source and the photon has to be available when required, i.e. on demand. For experiments it is also beneficial if photons are frequently obtainable and identical every time [56].

1.1.1 Deterministic emitting single photon sources

Deterministic single photon sources share the common characteristic, that they emit deterministically exactly one photon following an excitation within a characteristic relaxation time [56–59]. Photon sources in this class are based on atomic systems or ensembles, which are excited and emit a photon when relaxing back to the ground state.

Single atoms and ions can be used to generate single photons in this manner [8,60–62], however these implementations require the atom to be trapped in some way to be held in place. This often includes complex vacuum systems and magnetic-optical traps or optical

dipole traps[56,57]. Photons emitted from atoms have a narrow and well defined spectral line width and are therefore naturally suited to interface with atomic quantum memories. One drawback of such approaches is that an atom radiates in any direction after excitation. Experiments often use cavities to favour the emission into a specific spatial mode. In addition such systems are often cooled to reduce atomic motion and increase the coherence time.

Similarly molecules can be stimulated to emit single photons[56,63,64]. For some approaches room temperature operation has been demonstrated and broadband emission at various wavelengths is possible. A challenge is photo bleaching of the molecule which stops the molecule from emitting photons. Similarly blinking can occur where the molecule is sometimes in a state where it does not emit light.

Colour centres in diamond, such as NV or Silicon-vacancy (SiV) centres, form another platform for photon generation[59,65,66]. These defects in the diamond lattice exhibit similar behaviours as single atoms and can be addressed optically. In that way it can be optically excited to emit a single photon. Since the defects are embedded in a solid, optical trapping-fields are not necessary. A drawback of this, is that phonons interact with the colour centre and lead to shorter coherence times. Cooling of the diamond reduces the phonon contribution but increases the experimental complexity. The energy level splitting of the defect depends on the surrounding lattice and leads to variations between the emitted photons from different centres[65]. Another issue is the relatively high refractive index of diamond which makes it challenging to couple the emitted light to optical fibres. Here the development of nanostructures and cavities enhance the emission into a specific mode and

improve photon collection efficiencies [67,68].

The last platform that we will discuss is Quantum Dots (QDs) [41,69–71]. QDs are semiconductor structures that act as artificial atoms [56]. This gives the platform large versatility because different configurations can be implemented. The manufacturing process for these devices is still under development and the construction of identical devices is precluded by process variations. The environment of each QD influences its characteristics similarly to the colour centres and cryogenic temperatures are necessary to decouple the QD from the phonon population. The semiconductor structures used for QDs have a high refractive index making the coupling to optical fibres challenging. An advantage of this platform is that light guiding nanostructures and cavities can be built around the QDs to yield higher collection efficiencies, and also some degree of tuneability. The highest photon generation rates of $3.6 - 6.5 \cdot 10^6$ photons per second, have been observed for resonant excitation of QDs [41,72]. This approach with an optical excitation, has the drawback that the emitted photons are in the same mode as the pump field and techniques to separate these two fields lead to loss of half the emitted photons. Current investigations develop approaches to circumvent this difficulty [73].

We can see that single photons [74,75] are generated in a variety of platforms in the class of deterministic emitters. All approaches are capable, in principle, of single photon emission with high certainty. Nevertheless, a common challenge is to efficiently couple the emitted photon into a desired spatial mode such as an optical fibre while suppressing background noise. Several design approaches have been investigated to reduce photon loss to reach near deterministic photon delivery [60,66,76–78].

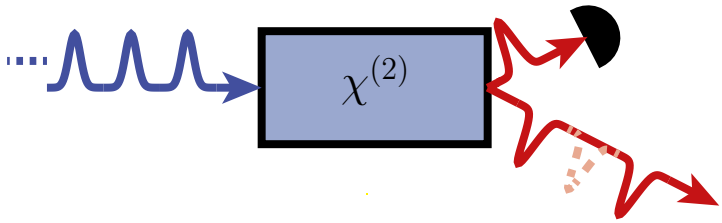

Figure 1.1: A spontaneous emitting heralded single photon source consist usually of a pump field and a optical non-linear material, e.g. $\chi^{(2)}$. The successful generation of a photon pair is heralded by a photon detector.

All platforms have to spend extra efforts to reduce the impact of noise processes by decoupling the system from the environment such as by cooling to cryogenic temperatures. The challenge for embedded atomic-like systems in solids is the impact of phonons and the local environment changing the properties of the emitted photons by the same device over time or similar but distinct devices.

1.1.2 Spontaneously emitting single photon sources

Spontaneously emitting single photon sources are the most ubiquitous photon source in quantum optics[56,57]. They established themself in the field quickly due to their comparatively low complexity and versatility. Spontaneous emitting photon sources generate photons in a large spectral range spanning from Ultraviolet (UV) up to infrared wavelengths. In addition no cooling to cryogenic temperatures or vacuum systems are required. The basic set-up of a spontaneous emitting single photon source consists of a pump laser and an optical non-linear material as depicted in Fig. 1.1 for the case of a pulsed pump field.
The figure already indicates, that the non-linear process does not emit deterministically a single photon but rather probabilistically emits a photon pair. Besides the vacuum state and a single photon pair, multiple photon pairs can also be generated. This makes a heralding scheme necessary, where a herald detector registers one photon of the pair to determine the

instances when photons are generated. The other partner of the pair is then the desired single photon. Photon number resolving detectors or weak pump fields ensure that when a herald occurs, the heralded photon output is mostly a single photon.

The photon pair emission by non-linear processes is directional such that collection efficiencies of the generated photons can be high[79]. This is not only necessary to enable high photon rates but also to achieve high heralding efficiencies. The heralding efficiency is the probability of detecting a heralded photon once its partner has been detected as the herald. For this thesis we consider the heralding efficiency to include the coupling and detection efficiencies of the set-up. Identical spontaneous emitting single photon sources can be built due to the high uniformity and consistency between batches of the non-linear materials[36,80].

There are many materials that are used for spontaneously emitting single photon sources. Spontaneous Parametric Down-Conversion (SPDC) processes in Beta Barium Borate (BBO)[81–83], Potassium Titanyl Phosphate (KTP)[84–86], Potassium Dihydrogen Phosphate (KDP)[87,88], and periodically poled Lithium Niobate (LN)[39,89–91] amongst others are used to generate photon pairs. Alternatively Four-Wave Mixing (FWM) processes in e.g. Silica[80,92–94], Silicon[95–97] and Silicon-nitride[96,97] have also been used to generate photon pairs.

Many of these platforms, such as LN[39,91], Silicon[38,98–100] and Silica[33,91,97,101–103] are commonly integrated with waveguiding structures, simplifying the optical alignment and phase stability of experiments. For photon sources, it also increases the brightness due to modal control and higher collection efficiencies from waveguides[104–106]. Interfacing such sources with linear optical networks on the same platform enables better scalability of experiments. Mode shaping can also improve the coupling efficiencies from interfaces to

optical fibres.

The relative simplicity of many of these materials allows flexibility in choosing the properties of the heralded photons. With this they meet the requirements of high photon flux and indistinguishability between photons emitted by the same or separate sources. This is the reason why spontaneous emitting single photon sources are the technology of choice for this thesis and we will investigate approaches to increase the availability of photons from these sources.

1.1.3 Multiplexed photon sources

We just learned that even though spontaneous emitting single photon sources generated photon pairs probabilistically, they are the most common approach to creating single photons. We will learn in Chapter 2 that the photon state generated is a TMSV state and that the single photon generation probability per trial of these sources is therefore fundamentally limited to 25 %[107]. This is detrimental for experiments that rely on the interference of several independent single photons, such as any implementation of the KLM scheme in quantum information processing[108]. To overcome these limitations multiplexing schemes have been introduced to increase the single photon emission probability[109,110].

Multiplexing of photon sources is an approach in which the emission of multiple sources is combined into a single output, as depicted in Fig. 1.2. Here the successful generation of a photon from at least one source is detected and the heralded photon is routed to the common output of the multiplexed source. This increases the probability of delivering a single photon to a subsequent experiment.

As an example we consider now the waiting time necessary to have N single photons

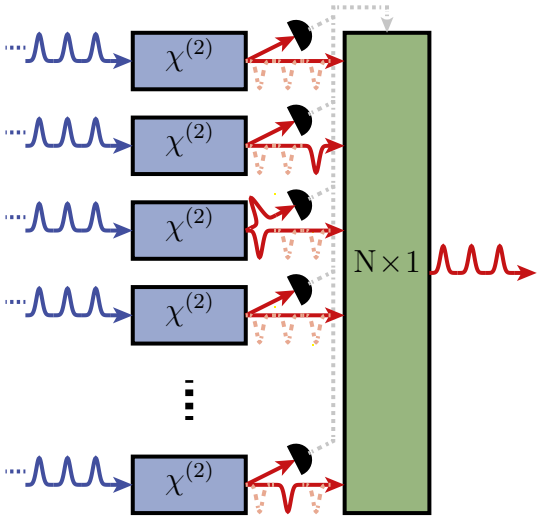

Figure 1.2: One approach to multiplexing is an array of N independent heralded single photon sources which are combined with a switching network, $N \times 1$. The herald detection information determines the setting for the switching network to route a generated photon to the output port.

available at the same time for an interference experiment [111], see Fig. 1.3. As in an experiment we assumed imperfections, such as a herald path efficiency of 25 %, a signal path efficiency of 15 %, a single photon fidelity of 90 %, and a repetition rate of the experiment of 10 MHz. The waiting time increases exponentially if the number of interfering photons is increased. Multiplexing of κ photon sources increases the availability of photons and therefore decreases the waiting time. This improvement is limited by loss and the heralding efficiency of the specific implementation.

1.2 Summary

The field of quantum information processing is aiming to implement new approaches to simulate quantum mechanical systems and to solve some computational problems faster than current classical machines Also new secure communication protocols are available with this technologies [112–115]. For hybrid and all optical approaches, photon sources constitute

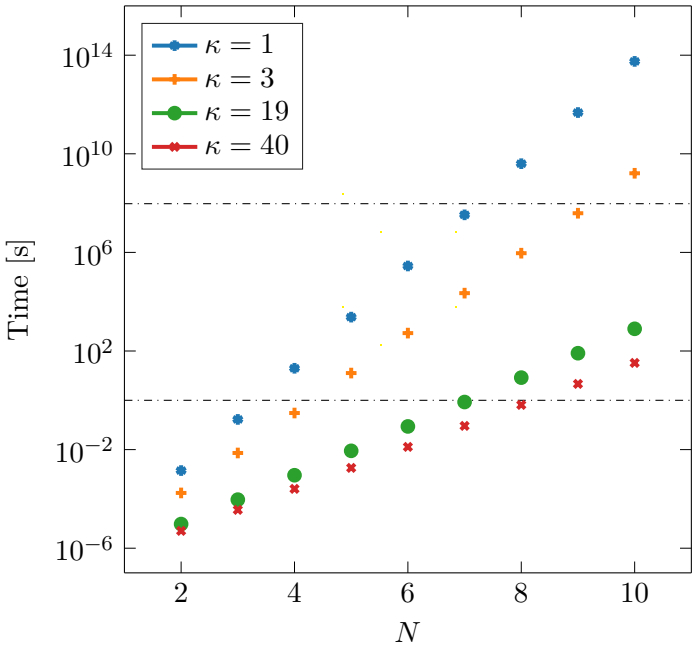

Figure 1.3: The waiting time for N simultaneous available photons for interference experiments increases significantly if the number of necessary photons increases. This waiting time can be decreased by multiplexing κ photon sources, which increases the probability of delivering a photon. The two dashed lines indicate a waiting time of 1 s and 3 years. The simulation takes a herald path efficiency of 25 %, a signal path efficiency of 15 %, and a single photon fidelity of 90 % into account. The repetition rate of the experiment is set to 10 MHz.

a fundamental resource for these devices.

The requirements for an optimal photon source used in such applications are:

1. that the single photons are in a pure state,

2. that the photons are delivered on demand,

3. and that photons are indistinguishable from one another.

In addition photons at telecommunication wavelength in the range of $1310 - 1550$ nm are preferred for long distance transmission, due to low propagation loss in optical fibres.

In this thesis we study the generation of pure heralded single photons based on non-linear processes. We investigate approaches to improve the inherent probabilistic photon generation, by frequency multiplexing, and discuss photon generation in direct UV-written Silica

waveguides, to reduce photon loss and increase system integration.

Chapter 2

Theoretical foundations of non-linear optical processes

Non-linear optical processes form the underlying mechanisms for the single photon sources studied in this thesis. In this chapter we will introduce a theoretical framework to describe these processes that are mediated by non-linear optical materials. We will also discuss different approaches to characterising the quantum state of light emitted by a single photon source.

To gain an understanding of non-linear optical processes, we first consider an electro-magnetic wave propagating through a material. This field interacts with the electrons bound to atoms in the material inducing an electric dipole moment and polarisation [116]. This time-varying electro-magnetic field leads to a time-varying polarisation which can in turn be a source of electro-magnetic radiation. If the exciting field is strong the polarisation response of the material is no longer described by a linear function of the applied electric field strength. The newly arising non-linear terms of the polarisation response can therefore

be the origin of fields at new frequencies. These newly arising fields are the phenomenon which we are interested in.

2.1 Light matter interaction and non-linear processes

Non-linear processes are well known [74,87,116–118] and a similar approach to their description is taken here. We write the polarisation response $\mathbf{P}(\vec{r},t)$ of a dielectric material to a strong electro-magnetic wave as a power series in the electric field strength $\mathbf{E}(\vec{r},t)$,

$$\mathbf{P}(\vec{r},t) = \epsilon_0 \left(\boldsymbol{\chi}^{(1)} \mathbf{E}(\vec{r},t) + \boldsymbol{\chi}^{(2)} \mathbf{E}^2(\vec{r},t) + \boldsymbol{\chi}^{(3)} \mathbf{E}^3(\vec{r},t) + \dots \right), \tag{2.1}$$

where ϵ_0 is the vacuum permittivity and $\boldsymbol{\chi}^{(n)}$ is the n-th order electric susceptibility.

Starting with Maxwell's equations one can derive the optical wave equation which contains the non-linear components of the material polarisation as source terms for the newly created fields [116]. We can understand this by considering that a single oscillating atom radiates as a dipole. A material consists of a large number of atoms, if these atoms oscillate collectively at a frequency with the correct phase relation they emit a directed electro-magnetic field at that frequency.

We now investigate how the non-linear terms in the polarisation lead to fields at new frequencies. For simplicity the lowest order non-linear term, the second-order non-linearity $\boldsymbol{\chi}^{(2)}$, is considered, assuming that the contribution of all other higher order terms is vanishingly small. For this example the exciting electric field has two frequency components of

amplitude E_n at central frequencies ω_n,

$$P^{(2)}(t) = \epsilon_0 \boldsymbol{\chi}^{(2)} E^2(t), \tag{2.2}$$

$$E(t) = E_1 \exp(-\imath\omega_1 t) + E_2 \exp(-\imath\omega_2 t) + \text{c.c.}, \tag{2.3}$$

where c.c. denotes the complex conjugate and we assume for simplicity that the field amplitudes are real values. Substituting the electric field in eq. (2.3) into eq. (2.2) results in the second order polarisation,

$$P^{(2)}(t) = \epsilon_0 \boldsymbol{\chi}^{(2)} \left(E_1^2 + E_2^2 + E_1^2 \exp(-\imath 2\omega_1 t) + E_2^2 \exp(-\imath 2\omega_2 t) + 2E_1 E_2 \exp(-\imath(\omega_1 + \omega_2)t) + 2E_1 E_2 \exp(-\imath(\omega_1 - \omega_2)t) + \text{c.c.}\right). \tag{2.4}$$

In the net material polarisation new frequencies arise, namely the second harmonic frequencies at $2\omega_1$ and $2\omega_2$ as well as the sum and difference frequencies at $\omega_1 + \omega_2$ and $\omega_1 - \omega_2$ respectively. This is the origin of new optical fields at these frequencies.

Centro symmetric materials, such as amorphous Silica, do not posses a 2^{nd} order electric susceptibility due to their inversion symmetry. The lowest order non-linear term is therefore the 3^{rd} order[116]. A similar approach can be taken as above to demonstrate the generation of a 4^{th} optical field from three input frequencies.

In a classical picture, the energy density of the electric field in a dielectric is given by,

$$\mathbf{U}(\vec{r}, t) = \frac{1}{2}\mathbf{E}(\vec{r}, t) \cdot \mathbf{D}(\vec{r}, t), \tag{2.5}$$

with the displacement field,

$$\mathbf{D}\left(\vec{r},t\right)=\epsilon_0\mathbf{E}\left(\vec{r},t\right)+\mathbf{P}\left(\vec{r},t\right). \tag{2.6}$$

We substitute the displacement field of equation (2.6) into eq. (2.5) and isolate the non-linear terms to write the interaction Hamiltonian as,

$$\mathbf{H}_I=\frac{1}{2}\int \mathrm{d}^3\vec{r}\,\mathbf{P}^{(n)}\left(\vec{r},t\right)\mathbf{E}\left(\vec{r},t\right), \tag{2.7}$$

where we only take the first non-linear order of the polarisation into account, and assume again that higher non-linear orders are vanishingly small. This is the case for low field strengths driving the non-linear processes. For SPDC, only the 2^{nd} order polarisation is relevant. In Silica the lowest order is $\mathbf{P}^{(3)}\left(\vec{r},t\right)$, giving rise to FWM. The mathematical description of both processes is very similar. For this reason, we only derive the expressions for the second order non-linearity where the approach for the third order non-linearity follows analogously.

In the case of SPDC, we write the interaction Hamiltonian explicitly in the form,

$$\mathbf{H}_I=\frac{1}{2}\int \mathrm{d}^3\vec{r}\,\epsilon_0\chi^{(2)}\mathbf{E}^3\left(\vec{r},t\right), \tag{2.8}$$

where $\chi^{(2)}$ is taken to be constant in the propagation direction of the optical field. The electric field that participates in the non-linear process is a sum of the driving pump field $\mathbf{E}_\mathrm{P}$ and the generated signal $\mathbf{E}_\mathrm{S}$ and idler $\mathbf{E}_\mathrm{I}$ fields. We refer to the field with the higher frequency component as the signal field. This superposition of the different fields is written

as,

$$\mathbf{E}\left(\vec{r},t\right)=\frac{1}{2}\sum_{m=\{\mathrm{P,S,I}\}}\left(\mathbf{E}_{m}^{(+)}\left(\vec{r},t\right)+\mathbf{E}_{m}^{(-)}\left(\vec{r},t\right)\right), \tag{2.9}$$

where $\mathbf{E}_{m}^{(-)}\left(\vec{r},t\right)=\left(\mathbf{E}_{m}^{(+)}\left(\vec{r},t\right)\right)^{\star}$ is the according Complex conjugate. The pump field is, compared to the generated fields, a strong optical field that we define classically as,

$$\mathbf{E}_{\mathrm{P}}\left(\vec{r},t\right)=A_{\mathrm{P}}\,g\left(x,y\right)\int\mathrm{d}\omega\,\alpha\left(\omega\right)\exp\left(-\imath\left(\omega t-k_{\mathrm{P}}\left(\omega\right)z\right)\right), \tag{2.10}$$

where A_{P} is the pump field amplitude, $k\left(\omega\right)=\frac{n(\omega)\omega}{c_0}$ is the wave-number, with $n\left(\omega\right)$ the refractive index of the material at angular frequency ω, c_0 is the speed of light in vacuum, and $\alpha\left(\omega\right)$ is the pump spectral envelope function. We assume that the pump field is not depleted in the process. All participating fields propagate in the z direction and are confined in a wave-guiding structure. $g\left(x,y\right)$ is the transverse spatial mode, normalised to

$$\int\int\mathrm{d}x\mathrm{d}y\;\left|g\left(x,y\right)\right|^{2}=1. \tag{2.11}$$

As an approximation the spectral-temporal pump pulse envelope, such as those emitted from a mode-locked laser, can be described by a Gaussian function. The pump spectral envelope function is therefore given as

$$\alpha\left(\omega_{\mathrm{P}}\right)=\exp\left(-\frac{\left(\omega_{\mathrm{P}}-\omega_{\mathrm{CP}}\right)^{2}}{2\sigma_{\mathrm{P}}^{2}}\right), \tag{2.12}$$

with ω_{CP} the central pump angular frequency and σ_{P} the spectral standard deviation of the pump field. We quantise the weak signal and idler fields and introduce the operator notation accordingly. Operators are distinct from the classical fields through the introduction of the

hat ˆ.

$$\hat{\mathbf{E}}_{\mathrm{S,I}}^{(+)}(\vec{r},t) = \imath g(x,y) \int \mathrm{d}\omega\, l(\omega) \exp\left(-\imath\left(\omega t - k_{\mathrm{S,I}}(\omega)\, z\right)\right) \hat{a}(\omega)\,, \tag{2.13}$$

describes the positive frequency components of the signal and idler fields as plane-waves, with

$$l(\omega) = \sqrt{\frac{\hbar\omega}{2\epsilon_0 c_0\, n(\omega)}}, \tag{2.14}$$

and $\hat{a}(\omega)$ is the photon annihilation operator. The according negative frequency components are given by the Hermitian conjugate ($h.c.$) such that $\mathbf{E}_m^{(-)}(\vec{r},t) = \left(\mathbf{E}_m^{(+)}(\vec{r},t)\right)^{\dagger}$. The photon creation and annihilation operators act on a photon state as usual, such that

$$\hat{a}^{\dagger}|n\rangle = \sqrt{n+1}\,|n+1\rangle\,, \tag{2.15}$$

$$\hat{a}|n\rangle = \sqrt{n}\,|n-1\rangle\,, \tag{2.16}$$

and follow the bosonic commutator relation. To be fully accurate, it is important to note that quantising the electric instead of the displacement field leads to an error of a factor $\frac{1}{2}$ [119]. We ignore this fact since only relative amplitudes are of importance here.

To find the generated output state we need to solve the Schrödinger equation for the time evolution of the input state $|\psi_{\mathrm{in}}\rangle = |vac.\rangle = |0_{\mathrm{S}}, 0_{\mathrm{I}}\rangle$ under the application of the interaction Hamiltonian,

$$|\psi_{\mathrm{out}}\rangle = \hat{T} \exp\left(\frac{1}{\imath\hbar}\int_0^t \mathrm{d}t'\, \hat{\mathbf{H}}_{\mathrm{I}}\left(t'\right)\right)|\psi_{\mathrm{in}}\rangle\,. \tag{2.17}$$

The time ordering operator $\hat{T}$ can be neglected for weak pump powers [120,121].

The output state takes a similar form to a TMSV state defined by

$$|TMSV\rangle = \exp\left(\xi \hat{a}^{\dagger}\hat{b}^{\dagger} + h.c.\right)|vac.\rangle\,,$$

where $\xi = r\exp(\imath\phi)$, with r the squeezing parameter and ϕ the optical phase [74,104,122]. We will investigate the TMSV state further in Section 2.2.1.

Equation (2.17) is solved by taking a Taylor expansion and truncating after the first order [120,121],

$$|\psi_{\text{out}}\rangle = \left(\mathbb{1} + \frac{1}{\imath\hbar}\int_0^t \mathrm{d}t'\,\hat{\mathbf{H}}_{\text{I}}\left(t'\right)\right)|\psi_{\text{in}}\rangle\,. \tag{2.18}$$

The interaction Hamiltonian is proportional to $\hat{\mathbf{E}}^3\left(\vec{r},t\right)$ and consists of $6^3 = 216$ terms covering all possible combinations of the creation and annihilation of photons in the signal and idler fields in combination with the pump field. For unpopulated signal and idler modes the input state is the vacuum state $|vac.\rangle$, therefore all terms that contain an annihilation operator must vanish. This leads to 3! remaining terms of the form $\hat{E}_{\text{P}}^{(+)}\hat{E}_{\text{S}}^{(-)}\hat{E}_{\text{I}}^{(-)}$. We can now write the output state as,

$$|\psi_{\text{out}}\rangle = \left(\mathbb{1} + \frac{1}{\imath\hbar}\frac{3\epsilon_0\chi^{(2)}}{8}\int_0^t\int \mathrm{d}t'\mathrm{d}\vec{r}\,\hat{\mathbf{E}}_{\text{P}}^{(+)}\left(\vec{r},t'\right)\hat{\mathbf{E}}_{\text{S}}^{(-)}\left(\vec{r},t'\right)\hat{\mathbf{E}}_{\text{I}}^{(-)}\left(\vec{r},t'\right)\right)|vac.\rangle\,. \tag{2.19}$$

The first term results in the vacuum component of the output state and the second term describes the photon pair state which is now discussed further.

2.1.1 Energy conservation

We start by substituting the pump (2.10), signal and idler fields (2.13) into the second term of eq. (2.19).

$$|\psi_{\text{pair,out}}\rangle = \frac{1}{\imath\hbar}\frac{3\epsilon_0\chi^{(2)}}{8}A_{\text{P}}\int_0^t\int\int\int\int \mathrm{d}t'\mathrm{d}\vec{r}\,\mathrm{d}\omega_{\text{P}}\,\mathrm{d}\omega_{\text{S}}\,\mathrm{d}\omega_{\text{I}}\,g_{\text{P}}(x,y)\,g_{\text{S}}^*(x,y)\,g_{\text{I}}^*(x,y)$$
$$l(\omega_{\text{S}})\,l(\omega_{\text{I}})\exp\left(-\imath\left(\omega_{\text{P}}-\omega_{\text{S}}-\omega_{\text{I}}\right)t'\right)\exp\left(-\imath\left(k_{\text{S}}(\omega_{\text{S}})+k_{\text{I}}(\omega_{\text{I}})-k_{\text{P}}(\omega_{\text{P}})\right)z\right)$$
$$\alpha_{\text{P}}(\omega_{\text{P}})\,\hat{a}_{\text{S}}^\dagger(\omega_{\text{S}})\,\hat{a}_{\text{I}}^\dagger(\omega_{\text{I}})\,|vac.\rangle\,. \quad (2.20)$$

The integration limits of the temporal integral can be extended to $\pm\infty$ due to the fact that the pump pulse duration is much shorter than the transit time of the pulse through the dielectric material of length L. With the new integration limits we simplify the integration to a delta function,

$$\int_{-\infty}^{\infty}\mathrm{d}t'\exp\left(-\imath\left(\omega_{\text{P}}-\omega_{\text{S}}-\omega_{\text{I}}\right)t'\right)=2\pi\delta\left(\Delta\omega\right), \quad (2.21)$$

where $\Delta\omega=\omega_{\text{S}}+\omega_{\text{I}}-\omega_{\text{P}}$. The delta function enforces energy conservation such that the energy of a photon in the pump field is equal to the sum of the signal and idler photon energies. We can picture the process in an energy level diagram with a ground state and an excited state, as illustrated in Fig. 2.1. In the PDC process, one pump photon excites the ground state and the generation of two daughter photons converts the system back to the ground state. A defining feature of the parametric process is that there is no change of the mediating material. The pump photon annihilation as well as the signal and idler photon creation is assumed to be instantaneous. Figure 2.1a displays the degenerate case

Figure 2.1: Energy level diagrams of degenerate SPDC (a) and degenerately pumped FWM (b): The energy of the converted pump field photons matches the energy of the emitted signal and idler photon pair.

with signal and idler photons of equal energy. FWM processes convert two pump photons to a signal and an idler photon such that the energy contained in those four fields is conserved. Figure 2.1b depicts this case for a degenerate pump configuration.

We enforce energy conservation on the spectrum of the down-converted photon pairs by substituting $\omega_\mathrm{P} = \omega_\mathrm{S} + \omega_\mathrm{I}$ in the spectral pump envelope function (2.12), such that,

$$\alpha_\mathrm{P}\left(\omega_\mathrm{P}\right) \rightarrow \alpha_\mathrm{P}\left(\omega_\mathrm{S} + \omega_\mathrm{I}\right). \tag{2.22}$$

Figure 2.2 shows the intensity distribution of the spectral pump envelope function $\left|\alpha_\mathrm{P}\left(\omega_\mathrm{S} + \omega_\mathrm{I}\right)\right|^2$ for two pump configurations. The pump spectral envelopes are assumed to be Gaussian functions with different bandwidths of 12 nm and 1.6 nm, and are centred at 1070 nm and 775 nm respectively.

2.1.2 Phase-matching condition

As a next step we perform the spatial integration in eq. (2.20). We assume that the down-conversion takes place within the fundamental spatial mode of a waveguide. The collinear process is therefore describe with field modes of a finite spatial extension in the x and y plane, as defined by $g\left(x, y\right)$. We also assume that $g\left(x, y\right)$ has a Gaussian shaped profile

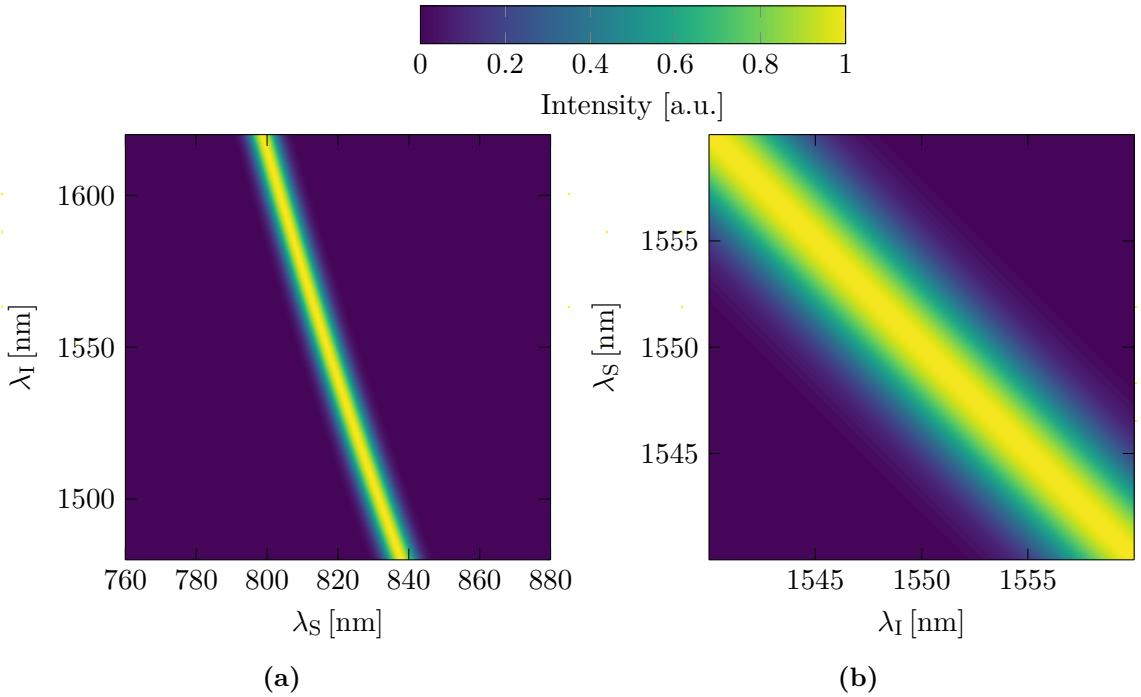

Figure 2.2: (a) displays an example of the intensity distribution of the pump envelope function for FWM and (b) for PDC versus the signal and idler wavelength.

confined in the waveguide core. Integrating along the x and y coordinate therefore leads to a constant factor which is combined with all other constants in the parameter ζ.

The remaining spatial integration along the propagation z-axis for the length L of the dielectric material is given by,

$$\int_0^L \mathrm{d}z \, \exp\left(-\imath \left(k_\mathrm{S}\left(\omega_\mathrm{S}\right) + k_\mathrm{I}\left(\omega_\mathrm{I}\right) - k_\mathrm{P}\left(\omega_\mathrm{P}\right)\right) z\right) = L \exp\left(\frac{\imath L \Delta k}{2}\right) \mathrm{sinc}\left(\frac{L\Delta k}{2}\right), \tag{2.23}$$

where $\Delta k = k_\mathrm{P}\left(\omega_\mathrm{P}\right) - k_\mathrm{S}\left(\omega_\mathrm{S}\right) - k_\mathrm{I}\left(\omega_\mathrm{I}\right)$ is the propagation constant mismatch. We obtain the phase-matching function $\Phi\left(\omega_\mathrm{S}, \omega_\mathrm{I}\right)$ by taking energy conservation, $\omega_\mathrm{P} = \omega_\mathrm{S} + \omega_\mathrm{I}$, into account,

$$\Phi\left(\omega_\mathrm{S}, \omega_\mathrm{I}\right) = \exp\left(\frac{\imath L \Delta k\left(\omega_\mathrm{S}, \omega_\mathrm{I}\right)}{2}\right) \mathrm{sinc}\left(\frac{L\Delta k\left(\omega_\mathrm{S}, \omega_\mathrm{I}\right)}{2}\right). \tag{2.24}$$

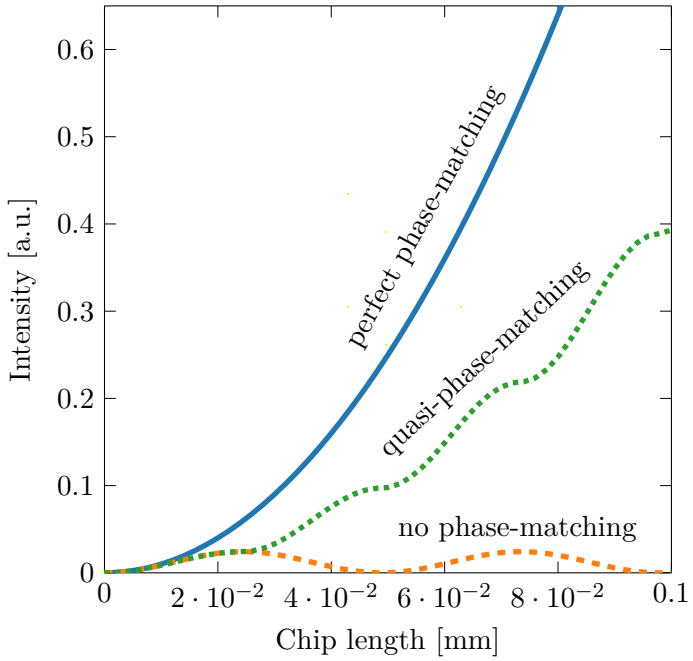

Figure 2.3: The output intensity increases for phase-matched processes with respect to the chip length, while it oscillates for a non-phase-matched process.

Perfect phase-matching requires that the propagation constant $k\vec{z}$ of the signal, idler, and pump fields are conserved such that $\Delta k = 0$. This means that the generated fields are in phase with one another. In general, optical dispersion results in $\Delta k \neq 0$ at the energy-matching point of the pump, signal, and idler fields. This non-phase-matched case limits the energy from remaining in the signal and idler fields and transfers the energy back to the fundamental pump field. Figure 2.3 displays these two scenarios for varying length of the non-linear material. Perfect phase-matching leads to a quadratic increase in the output field intensity, whereas the output field intensity oscillates for the non-phase-matched case. To fulfil the phase-matching condition at particular desired wavelengths, despite an unfavourable material dispersion, two different strategies are used in this thesis [56,116,118,123]. For birefringent materials, with different refractive indices for the ordinary and extraordinary axes, phase-matching can be maintained by choosing suitable polarisations of the

optical fields. We use this approach for FWM in Silica waveguides, where the signal and idler fields are orthogonally linearly polarised along these axes. The birefringence, Δn, increases the refractive index for one polarisation such that,

$$k(\omega) = \frac{(n(\omega) + \Delta n)\,\omega}{c_0}. \tag{2.25}$$

For non birefringent materials or materials where the birefringence is insufficient another strategy is chosen to guarantee phase-matching. Considering the non-phase-matched case in Fig. 2.3, we observe that the output field intensity oscillates periodically with the length of the non-linear material. If one can change the phase relationship of the fields and the non-linear polarisation at the maxima, further increases in the output intensity could be possible. This is exactly the strategy of quasi-phase-matching. The sign of the non-linear coefficient is inverted periodically to ensure further gain in the non-linear process. For a periodically poled material, with poling period Λ, the phase-matching condition changes to,

$$\Delta k = k_{\mathrm{P}}(\omega_{\mathrm{P}}) - k_{\mathrm{S}}(\omega_{\mathrm{S}}) - k_{\mathrm{I}}(\omega_{\mathrm{I}}) - \frac{2\pi}{\Lambda}. \tag{2.26}$$

The adjustment of the poling period enables phase-matched processes previously not accessible[116,124]. In Chapter 4, we use periodic poling for SPDC in KTP waveguides.

In a similar way to the energy level diagram, momentum conservation can also be pictured, as in Fig. 2.4. The wave-vector of the pump field matches the sum of the wave-vectors of the generated signal and idler fields. For quasi-phase-matching the poling period is added to the pump wave-vector to compensate for the phase-mismatch.

The phase-matched signal and idler wavelength are computed by incorporating the disper-

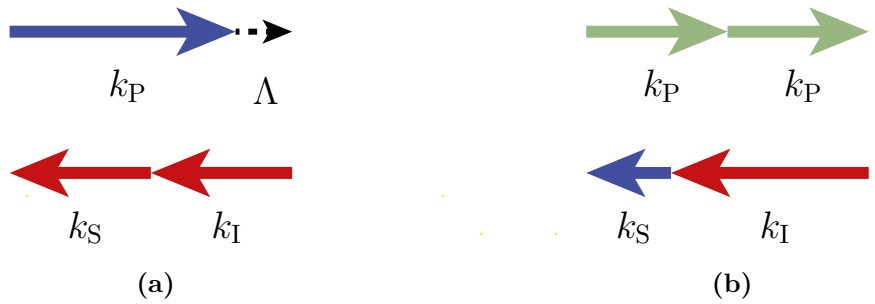

Figure 2.4: The arrows indicate momentum conversation for PDC with a periodic poling Λ (a) and FWM (b).

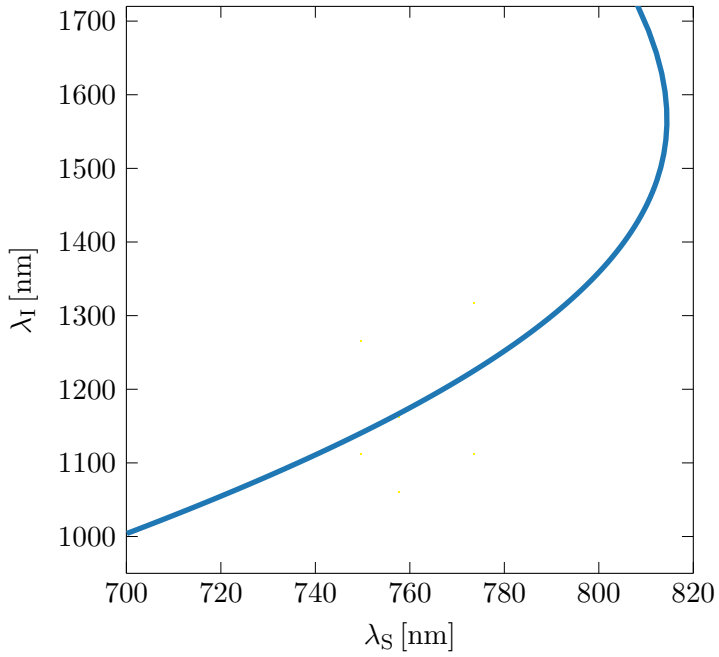

Figure 2.5: The solutions to the phase-matching condition $\Delta k = 0$ for birefringent phase-matched FWM in Silica.

sion for a specific material in the phase-matching condition. Figure 2.5 depicts the solutions of $\Delta k = 0$ for Silica glass. The refractive index of glass at various wavelengths is derived from the Sellmeier equations[125,126] and a constant birefringence of $3.7 \cdot 10^{-4}$ is added.

Figure 2.6 displays the absolute value squared of the phase-matching function in the signal and idler wavelength plane for Silica as well as KTP[127]. Here we represent the

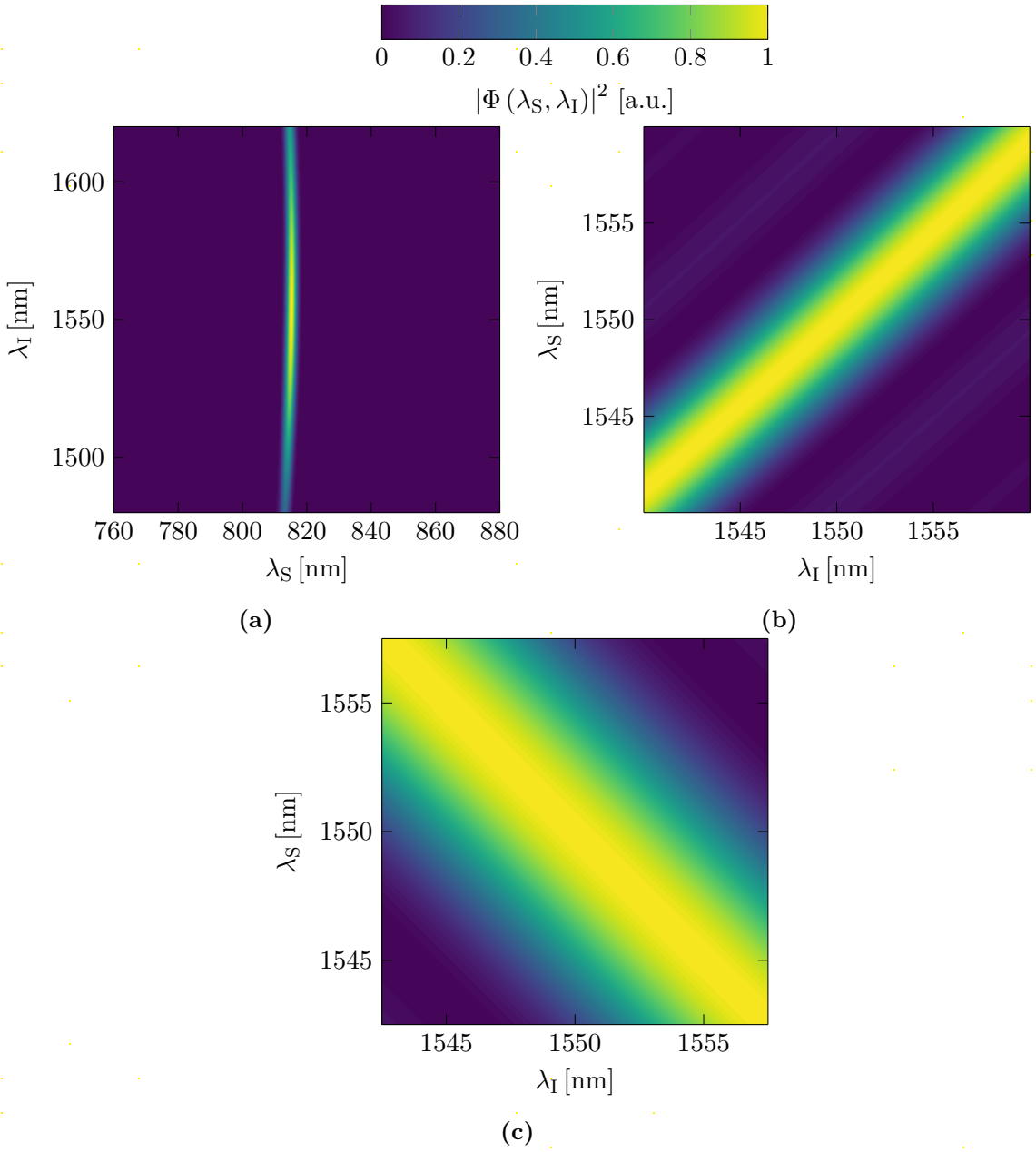

Figure 2.6: Examples of the phase-matching functions $|\Phi(\omega_S, \omega_I)|^2$ for (a) birefringent phase-matched FWM in Silica, (b) type-II SPDC and (c) type-0 SPDC in KTP: The angle of the phase-matching function depends on the group velocity of the fields in the material.

phase-matching function for two configurations for SPDC in KTP. Figure 2.6b displays the type-II phase-matching function where the signal and idler fields are orthogonally linearly polarised. In comparison Fig. 2.6c shows type-0 phase-matching where the pump, signal, and idler fields are all in the same linear polarisation, leading to a different slope of the phase-matching function. The angle of the phase-matching function in the (ω_S, ω_I) plane is dependent on the group velocity ν of the pump signal and idler fields and is approximated by[104,128],

$$\tan(\theta_\Phi) = -\frac{\nu_S^{-1} - \nu_P^{-1}}{\nu_I^{-1} - \nu_P^{-1}}. \tag{2.27}$$

A change in the field polarisations, such as between type-II and type-0 phase-matching or additional birefringence, therefore alters the angle of the phase-matching function. The width of $\Phi(\omega_S, \omega_I)$ is determined by the length L of the non-linear material. Longer non-linear materials result in narrower phase-matched solutions than shorter ones, as over shorter distances more frequencies remain nearly phase-matched.

2.1.3 The Joint Spectral Amplitude

To finalise this description of the emitted photon pair state, we compute the integration over the pump frequency in eq. (2.20). The delta function from the energy conservation leads to a simple replacement of the variables and constant factors are again combined into the factor ζ. We also assume that $l(\omega)$ does not vary significantly over the spectral ranges of the different fields and is therefore evaluated at the respective central frequencies. The

resulting expression of the two photon output state is,

$$\begin{aligned} |\psi_{\text{pair,out}}\rangle &= \zeta \int\int \mathrm{d}\omega_{\mathrm{S}}\, \mathrm{d}\omega_{\mathrm{I}}\, \Phi\left(\omega_{\mathrm{S}}, \omega_{\mathrm{I}}\right) \alpha_{\mathrm{P}}\left(\omega_{\mathrm{S}} + \omega_{\mathrm{I}}\right) \hat{a}_{\mathrm{S}}^{\dagger}\left(\omega_{\mathrm{S}}\right) \hat{a}_{\mathrm{I}}^{\dagger}\left(\omega_{\mathrm{I}}\right) |vac.\rangle \\ &= \zeta \int\int \mathrm{d}\omega_{\mathrm{S}} \mathrm{d}\omega_{\mathrm{I}}\, F\left(\omega_{\mathrm{S}}, \omega_{\mathrm{I}}\right) \hat{a}_{\mathrm{S}}^{\dagger}\left(\omega_{\mathrm{S}}\right) \hat{a}_{\mathrm{I}}^{\dagger}\left(\omega_{\mathrm{I}}\right) |vac.\rangle\,, \end{aligned} \tag{2.28}$$

with $F\left(\omega_{\mathrm{S}}, \omega_{\mathrm{I}}\right)$ the Joint Spectral Amplitude (JSA). The JSA describes the spectral-temporal properties of the emitted two photon state and will be discussed in more detail below.

In the previous section we saw how the phase-matching condition determines the phase-matched frequencies and how it can be satisfied to achieve phase-matching in desired frequency ranges. The JSA is the product of the phase-matching function eq. (2.24) and the pump envelope function eq. (2.12). Modifying these two functions leads to changes in the properties of the photon pair state.

In the previous Chapter 1.2, one of the conditions for an ideal single photon source was the requirement of generating photons in a pure state. This is important as it enables high interference visibilities, beyond the classical interference visibility of 50 %, between photons produced from independent sources or photons from consecutive pulses. Photon sources based on the described non-linear processes are inherently probabilistic sources. This means that for each pump pulse there is a finite probability of generating a photon pair. A heralding measurement, on either the signal or idler field, determines the instance in which a photon pair is generated. If the photon pair state is not factorisable, the heralding measurement projects the heralded photon into a mixture of the different spectral temporal

modes. The purity $\mathcal{P}$ of the heralded state is determined, e.g. for the signal field, by,

$$\mathcal{P} = \mathrm{Tr}\left(\hat{\rho}_{\mathrm{S}}^{2}\right)_{\mathrm{S}}, \tag{2.29}$$

where the density operator $\hat{\rho}_{\mathrm{S}}$ is defined as

$$\hat{\rho}_{\mathrm{S}} = \mathrm{Tr}\left(\hat{\rho}_{\mathrm{out}}\right)_{\mathrm{I}}, \tag{2.30}$$

with

$$\hat{\rho}_{\mathrm{out}} = |\psi_{\mathrm{out}}\rangle\langle\psi_{\mathrm{out}}|. \tag{2.31}$$

To circumvent this problem, photon sources have to be designed such that the output photon pair state is factorisable. The JSA captures all relevant properties of the output state and carefully setting the pump field properties as well as the phase-matching strategy determines the factorisability of the output state. For illustration purposes, the phase information is removed from the JSA and the Joint Spectral Intensity (JSI), $|F(\omega_{\mathrm{S}}, \omega_{\mathrm{I}})|^2$, is displayed instead. Figure 2.7 depicts several examples for possible JSI shapes for the presented experiments. The dispersion of the non-linear material, the material length, the phase-matching strategy, and the pump specifications all influence the properties of the JSA. The JSA corresponds to a pure state if it is factorisable into two functions such as,

$$F(\omega_{\mathrm{S}}, \omega_{\mathrm{I}}) = A(\omega_{\mathrm{S}})\, B(\omega_{\mathrm{I}}). \tag{2.32}$$

Type-0 phase-matched SPDC in KTP gives rise to a spectrally correlated JSI, see Fig. 2.7a, because of the parallel pump envelope and phase-matching functions. Here the

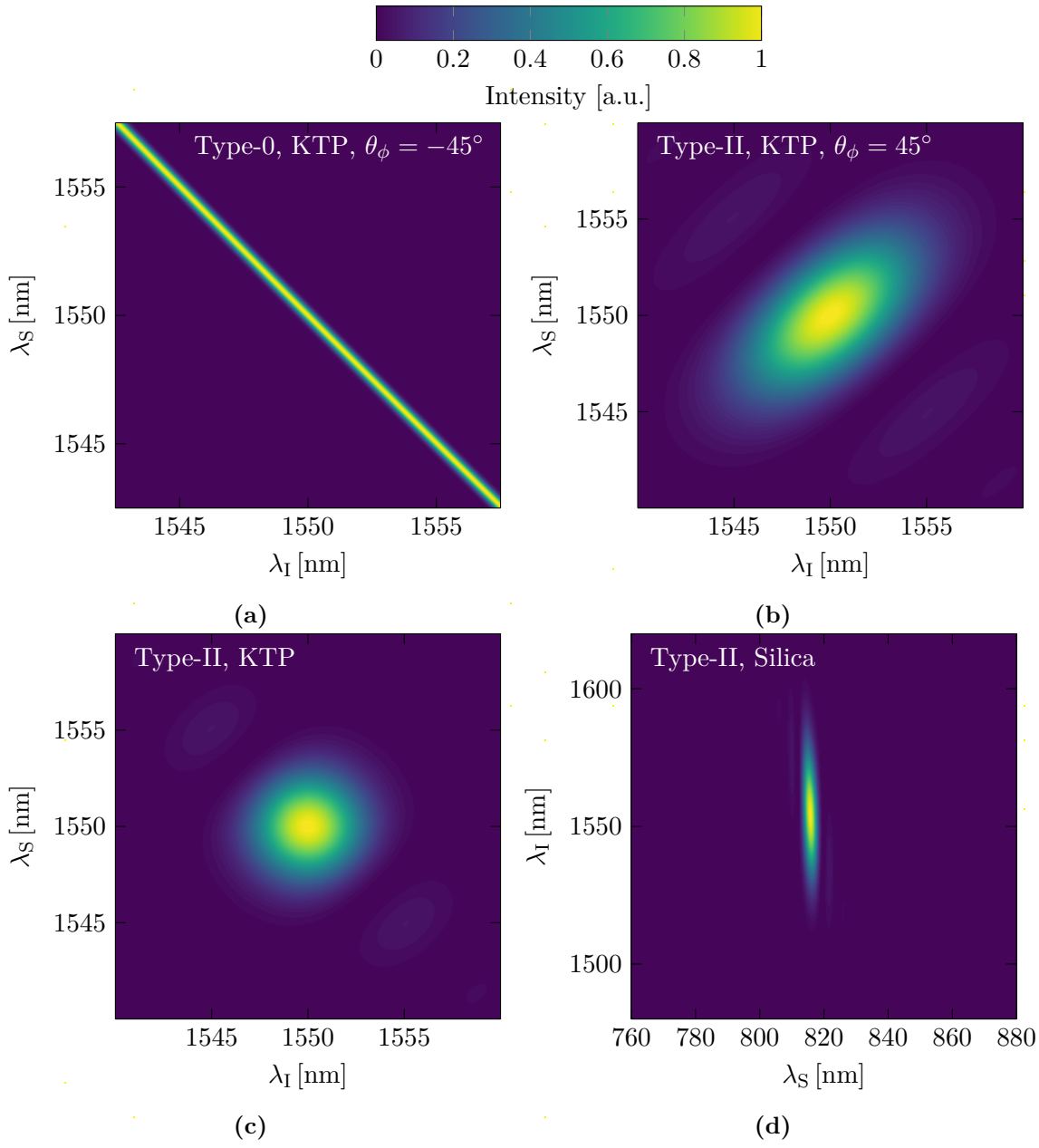

Figure 2.7: For type-0 phase-matched PDC in KTP the pump-envelope function and phase-matching function overlap over a wide range, establishing a frequency correlated JSI (a). The joint intensity distribution for type-II phase-matched PDC in KTP has a phase phase-matching function with a slope close to 45°. This gives access to (b) non-factorisable and (c) factorisable joint spectra dependent on the relation between the pump bandwidth and length of the non-linear material. (d) depicts a JSI for FWM in Silica with some spectral correlation.

angle of the phase-matching function is $\theta_\phi = -45°$ because $\nu_S^{-1} = \nu_I^{-1}$. The joint spectrum is also correlated if the pump bandwidth and the interaction length are not well matched as for the example of type-II PDC in Fig. 2.7b. Optimising these settings results in a factorisable JSA such as the one in Fig. 2.7c. In these configurations a phase-matching angle of $\theta_\phi = 45°$ is guaranteed by $\nu_S^{-1} = 2\nu_P^{-1} - \nu_I^{-1}$. The second platform of interest, to the discussion in this thesis, is FWM in Silica, which also shows a nearly decorrelated JSI for some parameters sets where $\theta_\phi = 90°$ and thus $\nu_I^{-1} = \nu_P^{-1}$ [129], see Fig. 2.7d. From a simple visual inspection of the JSI one can already tell if these configurations are spectrally correlated or not. Elliptical shapes are factorisable if the axes of the ellipse are horizontal and vertical, whilst diagonal ones are not.

Mathematically the amount of correlations can also be determined by performing a Singular Value Decomposition (SVD) of the JSA [128,130,131]. The SVD also gives insight into the mode structure and can be applied to joint spectral measurements to place an upper bound to the state purity.

The SVD is a eigenvalue decomposition and separates the JSA into a set of orthonormal basis functions such that,

$$F(\omega_S, \omega_I) = \sum_{i=1}^{N} \lambda_i A_i(\omega_S) \cdot B_i(\omega_I), \tag{2.33}$$

where λ_i are the eigenvalues corresponding to each set of eigenfunctions $A_i(\omega_S) \cdot B_i(\omega_I)$. For the case where the JSA is factorisable, the SVD returns a single mode as expected from equation (2.32).

For a correlated JSA, the SVD results in the mode structure displayed in Fig. 2.8. The SVD

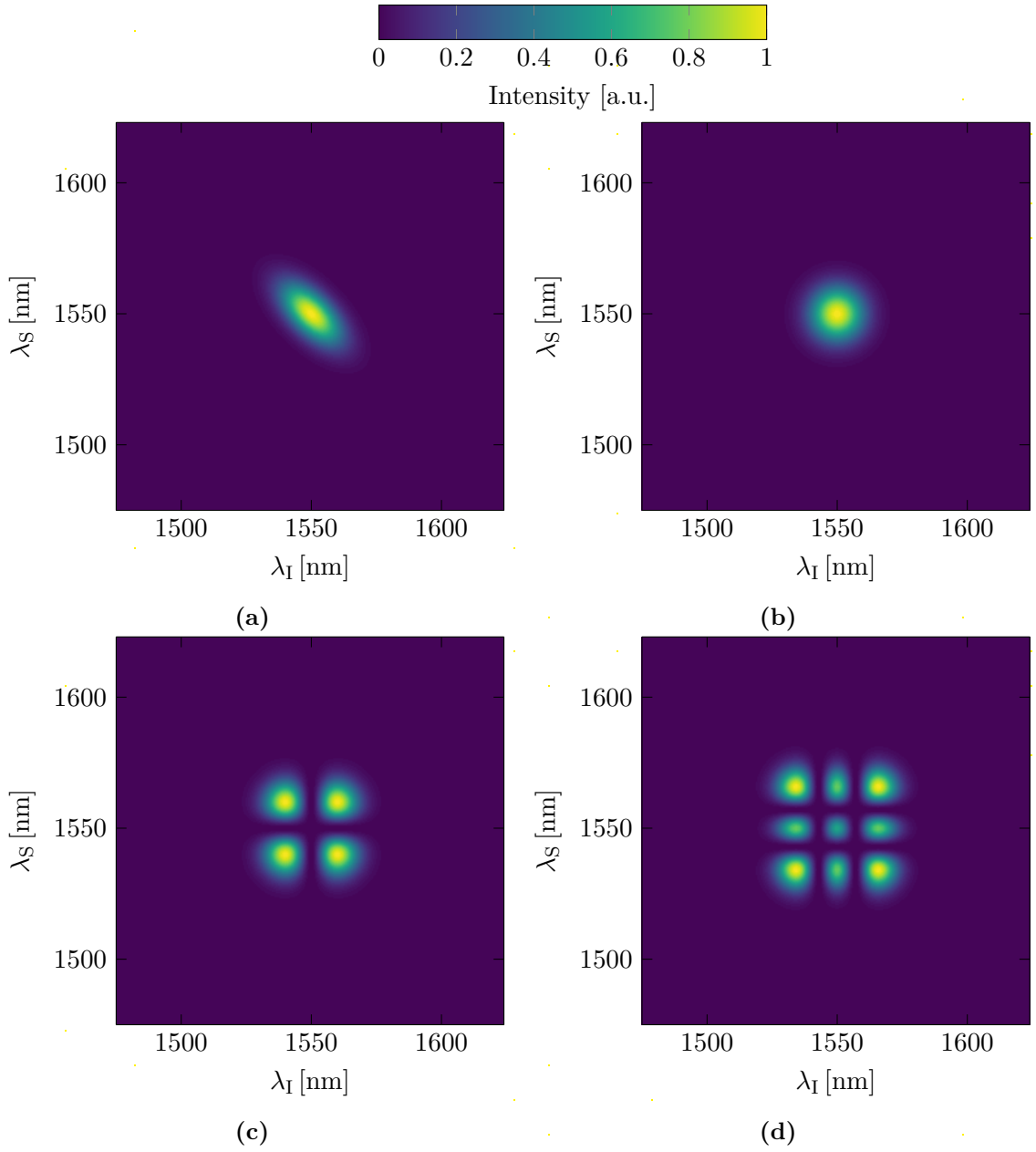

Figure 2.8: The mode decomposition of a correlated JSA. (a) displays the according correlated JSI and (b-d) represent the first three reconstructed eigenmodes with normalised amplitudes.

decomposes the correlated spectrum in Fig. 2.8a into its eigenmodes, where the first three are displayed with normalised amplitudes. Each of these modes individually corresponds to a factorisable state with unit purity. If the heralding measurement can not distinguish between these modes, as it is often the case, the heralded state is projected into a mixture of all modes.

Figure 2.9 shows the individual eigenfunctions for the first three modes of the signal 2.9a and idler 2.9b fields. It is apparent that those functions overlap spectrally and cannot be distinguished by spectrally resolving measurements. Figure 2.9c also displays the magnitudes of the corresponding eigenvalues. One notes that the eigenvalues for each mode decreases, such that for this example, modes beyond the 4^{th} form a minor contribution. We define an effective mode number, K, as a measure of the relative number of modes that contribute to the JSA. This effective mode number is given by[128],

$$K = \frac{\left(\sum_{i=1}^{N} \lambda_i^2\right)^2}{\sum_{i=1}^{N} \lambda_i^4}, \tag{2.34}$$

and represents the number of modes, with equal squeezing, contributing to the photon statistics emitted by the source. For the example displayed in Fig. 2.8 and 2.9, the effective mode number is $K = 1.25$. The inverse of the effective mode number also corresponds to the purity of the generated state

$$\mathcal{P} = \frac{1}{K}. \tag{2.35}$$

In the presented case, the purity is 80 %.

With these tools at hand we now investigate how changing some properties of the JSA influences the purity or effective mode number of the generated state. Again we use as

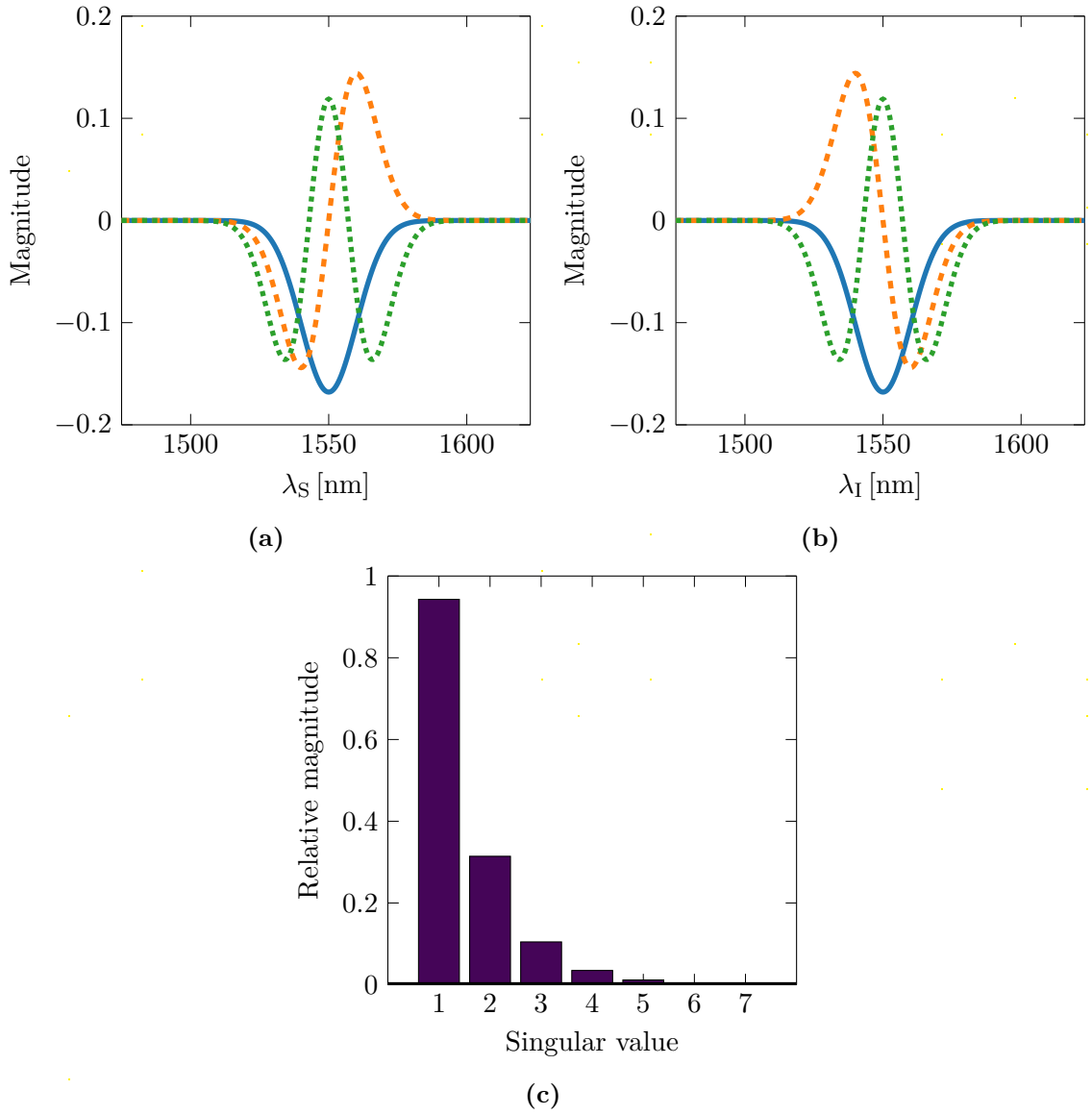

Figure 2.9: The decomposition of the correlated JSA as depicted in 2.8 results in a set of orthogonal eigenfunctions. The first three eigenfunctions for the signal (a) and idler (b) fields are displayed. The solid blue lines correspond to the first eigenfunction, where the dashed orange and the dotted green lines represent the second and third eigenfunctions. The relative magnitude of the corresponding eigenvalues decreases quickly (c).

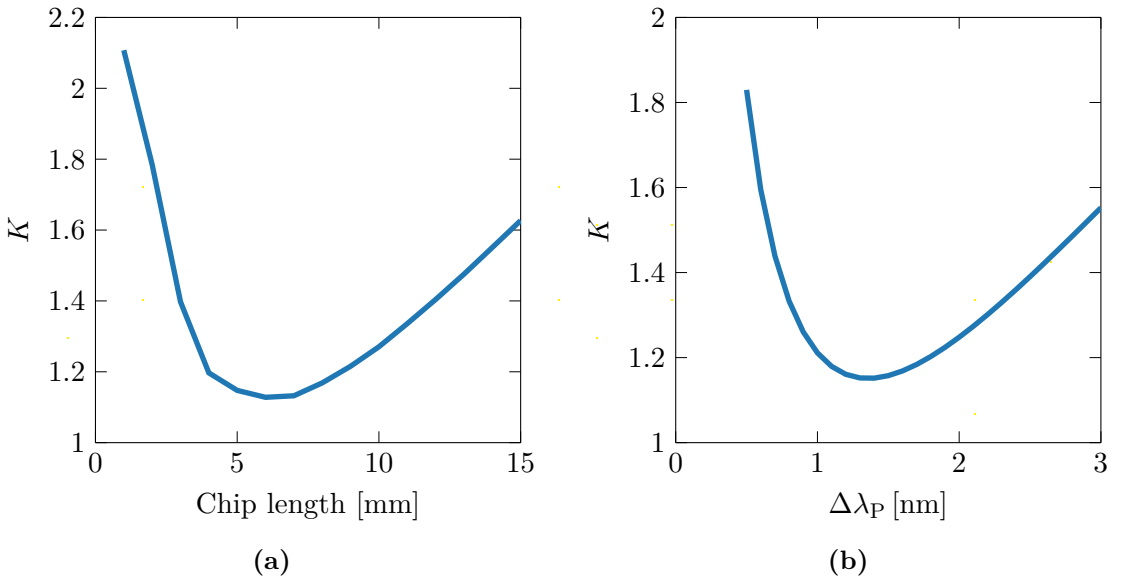

Figure 2.10: The chip length and bump bandwidth can be matched such that the effective mode number K, for type-II PDC in KTP, is minimized and the purity of the heralded photon optimized. The pump bandwidth remains fixed to 1.6 nm, when the chip length is varied and the chip length is set to 8 mm, while $\Delta\lambda_P$ is changed.

an example type-II PDC in KTP. We vary independently first the medium length and second the pump bandwidth $\Delta\lambda_P$ and derive the effective mode number, see Fig. 2.10. As expected a specific chip length and pump bandwidth minimizes the mode number.

2.2 Photon number statistics

The previous discussion focused on the spectral-temporal properties of the generated output state. Besides this, we must also study the photon number statistics of the output state if we aim to produce a high quality source of heralded single photons. In this section, we will learn which characteristics to expect and how these can inform us about the properties of the non-linear process and the quality of the output state.

2.2.1 The two mode squeezed vacuum state

Going back to equation (2.17) and focusing on the terms of the interaction Hamiltonian which we are interested in leads to an expression for the output state of the form,

$$|\psi_{\text{out}}\rangle = \hat{T}\exp\left(\frac{1}{\imath\hbar}\frac{3\epsilon_0\chi^{(2)}}{8}\int_0^t\int \mathrm{d}t'\mathrm{d}\vec{r}\,\hat{E}_{\text{P}}\left(\vec{r},t'\right)\hat{E}_{\text{S}}^{(-)}\left(\vec{r},t'\right)\hat{E}_{\text{I}}^{(-)}\left(\vec{r},t'\right)+h.c.\right)|vac.\rangle\,. \quad (2.36)$$

This equation shows close resemblance with a Two-Mode Squeezed Vacuum (TMSV) state and is one if the JSA is factorisable,

$$|TMSV\rangle = \exp\left(\xi\hat{a}^\dagger\hat{b}^\dagger + h.c.\right)|vac.\rangle\,, \quad (2.37)$$

where $\hat{a}^\dagger$ and $\hat{b}^\dagger$ are the creation operators of the two modes a and b and $\xi = r\exp(\imath\phi)$. r is the squeezing parameter and ϕ the optical phase[74,104,122]. The TMSV state is also expressed in the photon number basis as,

$$|TMSV\rangle = \text{sech}\,(r)\sum_{n=0}^{\infty}\left(-\imath\tanh\left(r\right)\right)^n|n_a,n_b\rangle\,, \quad (2.38)$$

where $r = |\xi|$ and n denotes the number of photons in mode a and b. In contrast to the previous section, this also takes into account all higher order photon number terms that have been truncated in the Taylor expansion previously. The TMSV state has perfect photon number correlation between the two output fields. This correlation enables the heralding procedure to select the occasions when photon-pairs are emitted. We write the probability

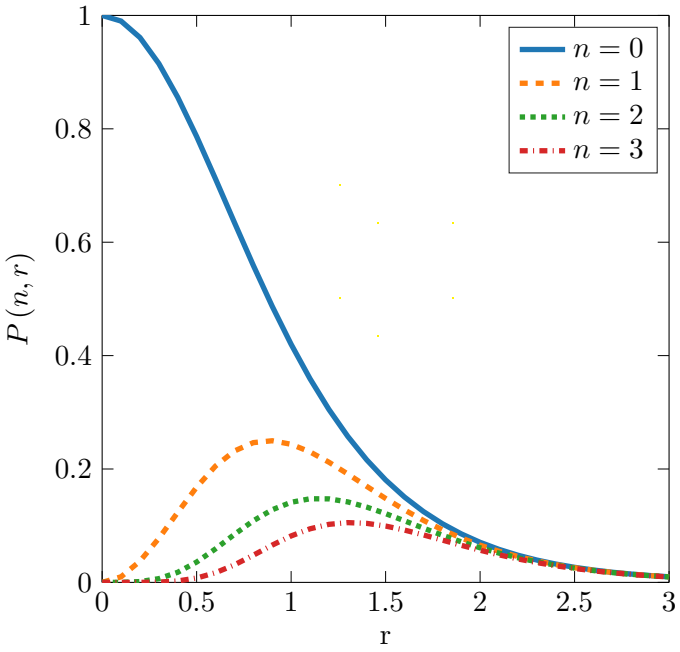

Figure 2.11: The probability $P(r,n)$ of generate no photons $n=0$ decreases steadily with increased squeezing r. At first the probabilities of emitting $n=1,2$ and 3 photons increases and later decreases again for large squeezing values. Notably the maximal probability of generating one photon $n=1$ is 25 % at a squeezing strength where higher photon number terms such as the one corresponding to two photons $n=2$ contribute significantly as well.

of generating a n photon state for a given squeezing strength r as,

$$P(r,n) = \langle n,n|TMSV\rangle \langle TMSV|n,n\rangle = \operatorname{sech}^2(r)\tanh^{2n}(r). \tag{2.39}$$

Figure 2.11 compares the probabilities of generating pairs with $n=0,1,2$ and 3 photons with respect to the squeezing strength. This plot reveals the previously mentioned 25 % limit of generating single photon pairs. It is also apparent that the vacuum component decreases with increasing squeezing and that the contribution of higher order photon number pairs $n>1$ increases. All curves in the plot tend towards small values for large squeezing because of other photon number terms arising which are not displayed.

Correlation functions

We gain further insight into the photon number distribution by studying correlations[74,131–134]. The correlation of a field at two times, t and $t+\tau$ is given by,

$$\begin{aligned} g^{(2)}(t,t+\tau) &= \frac{G^{(2)}(t,t+\tau)}{G^{(1)}(t,t)\,G^{(1)}(t+\tau,t+\tau)} \\ &= \frac{\left\langle \hat{E}^{(-)}(t)\,\hat{E}^{(-)}(t+\tau)\,\hat{E}^{(+)}(t)\,\hat{E}^{(+)}(t+\tau)\right\rangle}{\left\langle \hat{E}^{(-)}(t)\,\hat{E}^{(+)}(t)\right\rangle \left\langle \hat{E}^{(-)}(t+\tau)\,\hat{E}^{(+)}(t+\tau)\right\rangle}, \end{aligned} \tag{2.40}$$

where $\langle\cdot\rangle$ denotes the expectation value. Substituting the electric field (2.13) leads to the correlation function with no time offset $\tau = 0$ at $t = 0$,

$$g^{(2)}(0,0) = \frac{\langle \hat{a}^\dagger \hat{a}^\dagger \hat{a}\hat{a}\rangle}{\langle \hat{a}^\dagger \hat{a}\rangle \langle \hat{a}^\dagger \hat{a}\rangle} = \frac{\langle n^2\rangle - \langle n\rangle}{\langle n\rangle^2}. \tag{2.41}$$

We evaluate this quantity for one mode of the TMSV state and conclude that,

$$g^{(2)}(0) = \frac{\sum_{n=0}^{\infty} n\,(n-1)\;P(r,n)}{\left(\sum_{n=0}^{\infty} n\,P(r,n)\right)^2}. \tag{2.42}$$

It has been shown[131] that this Second order correlation function ($g^{(2)}$) value at zero time offset is directly related to the effective number of two-mode squeezers contributing to the output photon statistics, introduced earlier in equation (2.34),

$$g^{(2)}(0) = 1 + \frac{1}{K}. \tag{2.43}$$

In the following, the term mode refers to the number of TMSV states contributing to the output statistics and not to the two modes $\left(\hat{a}^\dagger, \hat{b}^\dagger\right)$ of the two mode-squeezer.

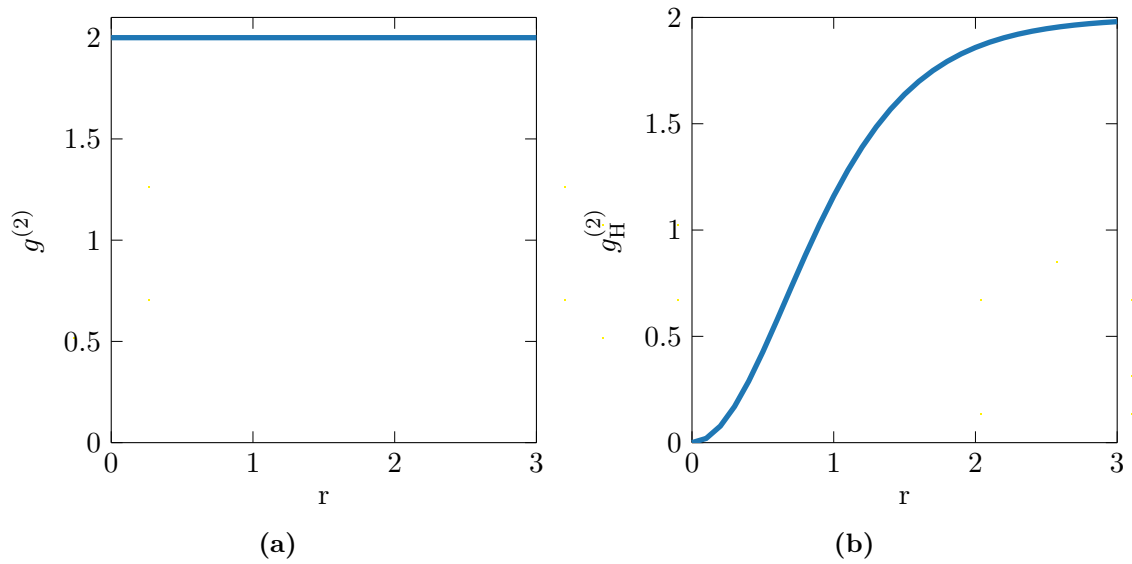

Figure 2.12: The unheralded $g^{(2)}$ is constant with respect to squeezing in the single mode case. The $g^{(2)}_{\mathrm{H}}$ is a measure of the contribution of higher order photon terms and should remain small for heralded photon sources without photon number resolving herald detectors.

Figure 2.12a displays a plot of the unheralded $g^{(2)}$ versus the squeezing. Unsurprisingly it is constant and equal to 2 in the ideal single mode case.

Another type of correlation that we investigate is the conditional correlation of detecting a photon in the heralded field of the TMSV state. The equation for the Heralded second order correlation function ($g^{(2)}_{\mathrm{H}}$) is similar to equation (2.42) only requiring the conditional probability of detecting a herald, H, photon,

$$g^{(2)}_{\mathrm{H}}(0) = \frac{\sum_{n=1}^{\infty} n\,(n-1)\; P\,(r,n\,|\,\mathrm{H})}{\left(\sum_{n=1}^{\infty} n\,P\,(r,n\,|\,\mathrm{H})\right)^2}, \tag{2.44}$$

assuming perfect photon number resolving detectors and no noise. The conditional proba-

bility for n photons given a herald has been detected $P(r, n > 0 \,|\, \mathrm{H})$ is,

$$P(r, n > 0 \,|\, \mathrm{H}) = \frac{P(r, n > 0)}{P_{\mathrm{H}}(r)}, \tag{2.45}$$

with

$$P_{\mathrm{H}}(r) = 1 - P(r, n = 0). \tag{2.46}$$

The pollution of higher order photon pairs in the heralded output state is assessed by measuring the $g_{\mathrm{H}}^{(2)}$. This is an important measure especially if non photon number resolving detectors are used, as is the case for most measurements presented in this thesis. For weak squeezing the $g_{\mathrm{H}}^{(2)}(0) \cong 0$ and increases as higher photon number terms start to contribute, see Fig. 2.12b.

The two correlation measurements we introduced, help to assess the performance of single photon sources. A single mode source $K = 1$ with $g^{(2)} = 2$ and a small $g_{\mathrm{H}}^{(2)}$ close to zero represents the optimal condition.

Multiple two mode squeezers

In a previous section we saw that designing a perfect source with no correlations is rather difficult to achieve and that some contributions from other modes modify the output state. Now we will investigate how the output photon statistics and the correlation measurements change if more than one mode contributes to the output.

We start by considering that κ independent modes of TMSV states emit photons. All permutations of the κ modes contribute to the probability of generating n photon pairs. One way of capturing all these permutations is with generating functions[135]. A power-

series defines the generating function for each mode i with squeezing r_i,

$$g_i(\zeta) = \sum_n P(r_i, n)\,\zeta^n = \frac{\operatorname{sech}^2(r_i)}{1 - \zeta \tanh^2(r_i)}. \tag{2.47}$$

The probability distribution for all κ modes takes then the form,

$$P(r, n, \kappa) = \frac{1}{n!}\left(\frac{\partial^n}{\partial \zeta^n}\prod_{i=1}^{\kappa} g_i(\zeta)\right)\Bigg|_{\zeta=0}, \tag{2.48}$$

where each eigenvalue of the SVD weights the squeezing r such that,

$$r_i = r\lambda_i. \tag{2.49}$$

With this formulation for generating n photons from multiple modes we define P_{H}, the $g^{(2)}$, and the $g^{(2)}_{\mathrm{H}}$ for the multi mode case in a similar manner as before in equations (2.42), (2.44) and (2.46).

Figure 2.13 displays the $g^{(2)}$ and $g^{(2)}_{\mathrm{H}}$ versus the squeezing r, where the squeezing parameter is constant for each mode $r_i = \frac{1}{\kappa}r$. Again the $g^{(2)}$ is constant for each scenario but decreases with the mode number as expected, see equation (2.43). The $g^{(2)}_{\mathrm{H}}$ increases as well as before, but the increase is slower for more modes since the squeezing per mode is reduced. Figure 2.13c represents the $g^{(2)}_{\mathrm{H}}$ versus the coincidence detection probability (P_{CC}). We assume no loss and every generated photon is detected. In that case P_{CC} is equal to the herald detection probability P_{H}. The detection probability increases with mode number while the contribution of higher order terms is reduced, as this is the advantage of combining

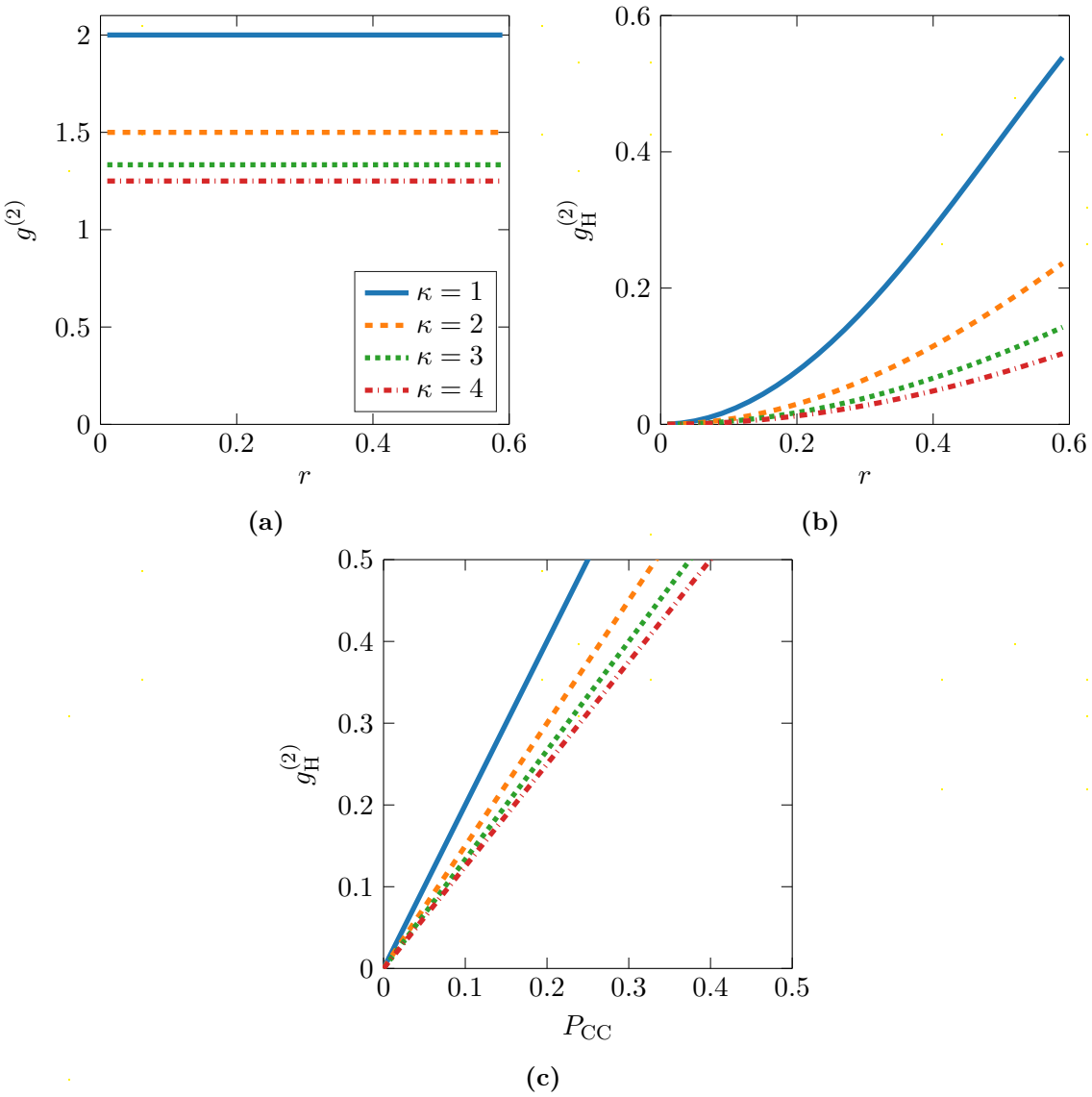

Figure 2.13: The (a) $g^{(2)}$ decreases for an increased mode number κ as expected. For (b) the $g^{(2)}_{\mathrm{H}}$ is also smaller for an increased mode number. This is due to the fact, that the squeezing r is now distributed amongst several modes. The $g^{(2)}_{\mathrm{H}}$ increases linearly with respect to the coincidence detection probability P_{CC} (c). Here the $g^{(2)}_{\mathrm{H}}$ is again smaller for more modes due to the decreased squeezing per mode.

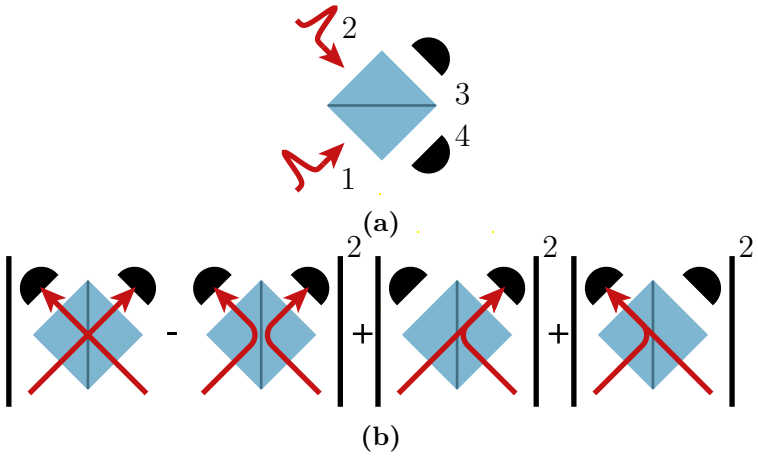

Figure 2.14: (a) in a HOM interference experiment two indistinguishable photons impinge on either input of a balanced beam splitter. (b) the coincidence detection probability amplitudes of two of the four possible outcomes interfere destructively, leading to the HOM effect.

multiple modes which is harnessed in multiplexed single photon sources.

2.3 The Hong, Ou and Mandel interference effect

If two indistinguishable photons impinge on the two inputs of a beam splitter an interference effect occurs as first observed and later named after HOM[136]. We start to investigate this phenomenon by depicting in Fig. 2.14 two photons entering a beam splitter on the two entrance facets labelled 1 and 2[117,137,138]. The transformation matrix for a perfect 50 : 50 beam splitter relates the input ports 1 and 2 to the outputs 3 and 4 by,

$$\begin{pmatrix} \hat{a}_1^\dagger \\ \\ \hat{a}_2^\dagger \end{pmatrix} = \sqrt{\frac{1}{2}} \begin{pmatrix} 1 & 1 \\ \\ -1 & 1 \end{pmatrix} \begin{pmatrix} \hat{a}_3^\dagger \\ \\ \hat{a}_4^\dagger \end{pmatrix}. \tag{2.50}$$

Starting with the state at the input ports, $\hat{a}_1^\dagger \hat{a}_2^\dagger |vac.\rangle$, and performing the mode operation of the beam splitter results in,

$$\begin{aligned} \hat{a}_1^\dagger \hat{a}_2^\dagger |vac.\rangle &= \frac{1}{2}\left(\hat{a}_3^\dagger + \hat{a}_4^\dagger\right)\left(-\hat{a}_3^\dagger + \hat{a}_4^\dagger\right)|vac.\rangle \\ &= \frac{1}{2}\left(-\hat{a}_3^{\dagger 2} + \hat{a}_4^{\dagger 2} + \hat{a}_3^\dagger \hat{a}_4^\dagger - \hat{a}_4^\dagger \hat{a}_3^\dagger\right)|vac.\rangle . \end{aligned} \tag{2.51}$$

Using the bosonic commutator relation $\left[\hat{a}_\alpha^\dagger, \hat{a}_\beta^\dagger\right] = 0$ simplifies the expression to,

$$\begin{aligned} &= \frac{1}{2}\left(-\hat{a}_3^{\dagger 2} + \hat{a}_4^{\dagger 2} + \hat{a}_3^\dagger \hat{a}_4^\dagger - \hat{a}_3^\dagger \hat{a}_4^\dagger\right)|vac.\rangle \\ &= \frac{1}{2}\left(-\hat{a}_3^{\dagger 2} + \hat{a}_4^{\dagger 2}\right)|vac.\rangle \end{aligned} , \tag{2.52}$$

where the terms of photons in separate output ports destructively interfere due to the π-phase shift acquired on reflection. This explains the fact, that an experiment two indistinguishable inputs and with two detectors monitoring the output ports does not record any coincident detection events.

If the photons are distinguishable, or are in a mixed state, the interference of the photon detection probability amplitudes will not be perfect. In a HOM experiment a time delay between the photons on the input ports is tuned to scan the temporal distinguishability of the photons. This gives rise to an interference dip as depicted in Fig. 2.15. The visibility V of this interference pattern is a measure of the state purity and indistinguishability. We define the visibility as [87],

$$V = \frac{\mathrm{CC}(\infty) - \mathrm{CC}(0)}{\mathrm{CC}(\infty)}, \tag{2.53}$$

for the coincidence detection events CC at time delay $\Delta\tau$. Classical fields show a maximum

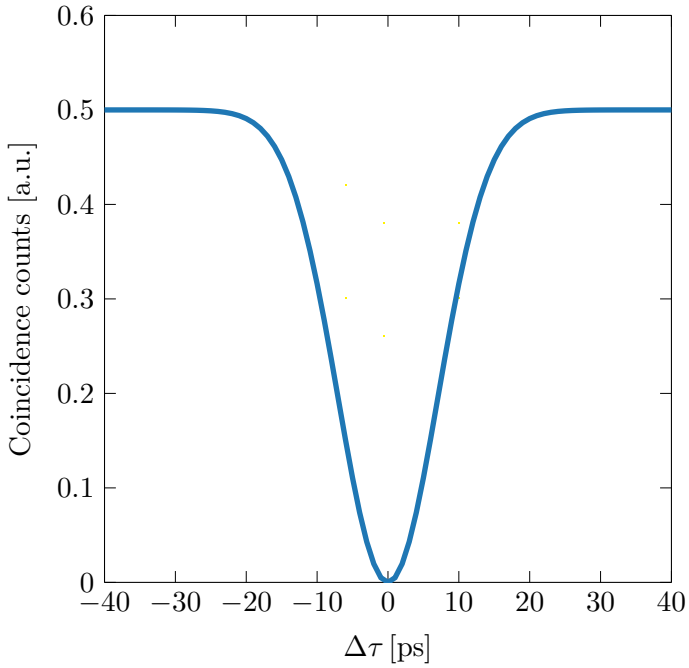

Figure 2.15: The rate of detecting a heralded coincidence event is constant if the two input single photons to a beam splitter are distinguishable, e.g. due to a time offset $\Delta\tau \neq 0$. If this time offset is reduced, the coincidence detection rate decreases due to the HOM effect, reaching a minimum at zero time delay.

interference visibility of 50 %[136].

We calculate the HOM interference dip for the state generated in the non-linear process in the following way. The starting point is the output two photon state described in eq. (2.28),

$$|\psi_{\text{pair,out}}\rangle = \zeta \int\int \mathrm{d}\omega_{\mathrm{S}}\mathrm{d}\omega_{\mathrm{I}}\, F\left(\omega_{\mathrm{S}},\omega_{\mathrm{I}}\right) \hat{a}_{\mathrm{S}}^{\dagger}\left(\omega_{\mathrm{S}}\right) \hat{a}_{\mathrm{I}}^{\dagger}\left(\omega_{\mathrm{I}}\right) |vac.\rangle\,.$$

The HOM interference is measured, in the presented experiment, by a four photon detection event of the two heralding photons, i.e. the idler photons, and the two interfering heralded photons, i.e. the signal photons, as depicted in Fig. 2.16. We can write the combined four

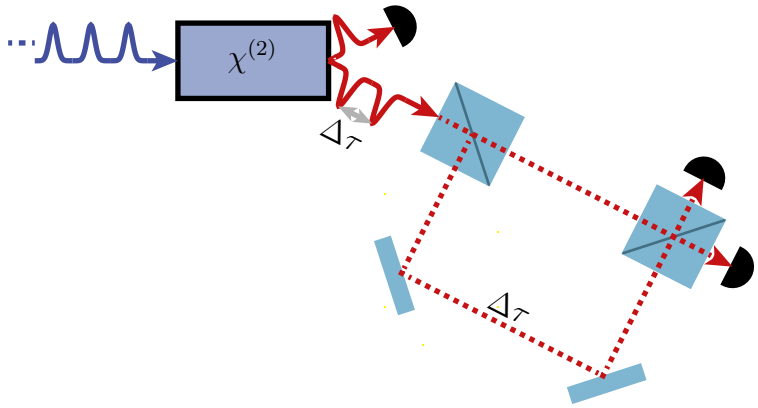

Figure 2.16: In the presented experiment, the four fold coincidence measurement of the HOM dip is between two consecutive herald photons and the heralded signal photons, which enter the interferometer.

photon state as

$$|\psi_4\rangle = \zeta\tilde{\zeta}\int\int\int\int \mathrm{d}\omega_\mathrm{S}\mathrm{d}\omega_\mathrm{I}\mathrm{d}\tilde{\omega}_\mathrm{S}\mathrm{d}\tilde{\omega}_\mathrm{I}\, F\left(\omega_\mathrm{S},\omega_\mathrm{I}\right)\tilde{F}\left(\tilde{\omega}_\mathrm{S},\tilde{\omega}_\mathrm{I}\right)\hat{a}^\dagger_{\mathrm{S},1}\left(\omega_\mathrm{S}\right)\hat{a}^\dagger_{\mathrm{I}1}\left(\omega_\mathrm{I}\right) \\ \hat{a}^\dagger_{\mathrm{S},2}\left(\tilde{\omega}_\mathrm{S}\right)\hat{a}^\dagger_{\mathrm{I}2}\left(\tilde{\omega}_\mathrm{I}\right)|vac.\rangle\,, \tag{2.54}$$

where the signal photon of the emission denoted by $\sim$ enters the beam splitter in the second port. The modes of the herald photons are distinguished by the labels I1 and I2. The measurement operator of the four photon event between the two herald detections and the output ports of the beam splitter is given by,

$$\hat{\Pi}_4 = \int\int\int\int \mathrm{d}\omega_3\mathrm{d}\omega_{\mathrm{H}1}\mathrm{d}\omega_4\mathrm{d}\tilde{\omega}_{\mathrm{H}2}\,\hat{a}^\dagger_3\left(\omega_3\right)\hat{a}^\dagger_{\mathrm{H}1}\left(\omega_{\mathrm{H}1}\right)\hat{a}^\dagger_4\left(\omega_4\right)\hat{a}^\dagger_{\mathrm{H}2}\left(\tilde{\omega}_{\mathrm{H}2}\right)|vac.\rangle \\ \langle vac.|\,\hat{a}_3\left(\omega_3\right)\hat{a}_\mathrm{H}\left(\omega_\mathrm{H}\right)\hat{a}_4\left(\omega_4\right)\hat{a}_\mathrm{H}\left(\tilde{\omega}_\mathrm{H}\right). \tag{2.55}$$

We use the beam splitter relation to convert the output mode operators to the input mode

operators where we assume a time delay $\Delta\tau$ in input mode 1,

$$\hat{a}_3(\omega_3) = \exp(-\imath\omega_3\Delta\tau)\,\hat{a}_1(\omega_3) - \hat{a}_2(\omega_3), \tag{2.56}$$

$$\hat{a}_4(\omega_4) = \exp(-\imath\omega_4\Delta\tau)\,\hat{a}_1(\omega_4) + \hat{a}_2(\omega_4). \tag{2.57}$$

By combining these expressions, the probability of a four fold event is given by

$$\begin{aligned} P_4 &= \mathrm{Tr}(\rho_4\Pi_4) = \langle\psi_4|\,\hat{\Pi}_4\,|\psi_4\rangle \\ &\propto \int \mathrm{d}\omega_3\,\mathrm{d}\omega_4\,\mathrm{d}\omega_{\mathrm{H1}}\,\mathrm{d}\omega_{\mathrm{H2}}\,\Big(|F_1(\omega_4,\omega_{\mathrm{H1}})\,F_2(\omega_3,\omega_{\mathrm{H2}})|^2 + |F_1(\omega_3,\omega_{\mathrm{H1}})\,F_2(\omega_4,\omega_{\mathrm{H2}})|^2 \\ &\quad - F_1(\omega_4,\omega_{\mathrm{H1}})\,F_2(\omega_3,\omega_{\mathrm{H2}})\,F_1^*(\omega_3,\omega_{\mathrm{H1}})\,F_2^*(\omega_4,\omega_{\mathrm{H2}})\exp(\imath(\omega_3-\omega_4)\Delta\tau) \\ &\quad - F_1(\omega_3,\omega_{\mathrm{H1}})\,F_2(\omega_4,\omega_{\mathrm{H2}})\,F_1^*(\omega_4,\omega_{\mathrm{H1}})\,F_2^*(\omega_3,\omega_{\mathrm{H2}})\exp(-\imath(\omega_3-\omega_4)\Delta\tau)\Big). \end{aligned} \tag{2.58}$$

For no time delay $\Delta\tau = 0$, and indistinguishable heralded photons $F_1 = F_2$, the minimum of the fourfold event probability $P_4 = 0$ is reached, and therefore 100% visibility is recovered. The visibility represents the state purity if F_1 and F_2 are equal as does the previously introduced SVD method and a measured $g^{(2)}$. The difference of these methods is, that the $g^{(2)}$ measurement is very sensitive to noise where as the HOM interference is more robust. A HOM dip measurement can also be used to compare the outputs from different photon sources, and hence determine the indistinguishability and suitability of different sources to realise complex multi-photon interference experiments.

Chapter 3

Frequency multiplexing: concept and theory

Following the general introduction and description of probabilistic heralded single photon sources in the previous chapters we now want to focus our attention on a specific implementation. More precisely, we are going to learn about a Heralded Single Photon Source (HSPS) design that implements a frequency multiplexing scheme that aims to address the fundamental limitations of traditional HSPSs. We saw previously in Chapter 2.2.1 that the state of an emitted photon from a non-linear interaction is a TMSV state, which we described mathematically by

$$|TMSV\rangle = \operatorname{sech}(r) \sum_{n=0}^{\infty} (-\imath \tanh(r))^n |n,n\rangle .$$

This state is composed of different photon number contributions $|n,n\rangle$, with weighting determined by the squeezing parameter r. It is therefore, also possible that the source

not only emits a single photon pair but also vacuum or higher order photon pairs. The probability distribution, described by Bose-Einstein statistics of Bosons, for a two-mode squeezer is the reason why the probability of generating a single photon pair does not exceed 25% [107].

Overcoming this fundamental limitation is relevant if one considers the interference of N independently generated single photons where the probability of the N photons coinciding decreases exponentially as $P(r, n = 1)^N$. This is already a limiting factor in current relatively small scale photonic experiments with $N = 10$ [139]. Fault tolerant Linear Optical Quantum Computing (LOQC) schemes require $10^5 - 10^6$ photons to encode a physical qubit [108]. In light of such demands, the problem of making such a large number of photons simultaneously available becomes daunting. Addressing and solving this problem is far out of scope for this thesis but highlights the importance of investigating approaches that increase the photon emission probability for HSPS and minimise overhead costs. We are therefore interested in developing the techniques for continuous frequency multiplexed single photon sources which can help reduce the challenge posed.

3.1 The concept of multiplexing

In the introduction of this thesis the concept of multiplexing was presented. It is a way of increasing the channel capacity by adding additional degrees of freedom. This concept can also be used to improve the performance of probabilistically emitting heralded single photon sources, since various degrees of freedom such as spatial modes, polarisation, frequency and time exist, as we will see in the following sections.

Multiplexing is implemented for photon sources to increase the emission probability of

a heralded single photon [109,110]. For this, the emission of a single photon is attempted over multiple trials. One of the successful trials is identified and routed to the output with a switching network. This active step, of feed forward control, which identifies the successful event and routes it to a common output, is the essential component that improves the performance of a multiplexed source in comparison to a passive one. The additional degree of freedom is needed to enable the identification of a successful photon generation on one specific attempt. We can see that the probability of at least one out of N trials successfully generating a single photon pair is much higher than the chance of generating a single photon pair in one attempt

$$P(n=1) \leq P(n=1,N) = 1-(1-P(n=1))^N . \tag{3.1}$$

In the case of $N = 19$ distinct modes and the maximal photon generation probability of $P(n=1) = 25\%$ this expression evaluates to $P(n=1,N=19) = 99.6\%$ [107]. Even for a much smaller number of modes $N = 3$ the improvement is still significant with $P(n=1,N=3) = 57.8\%$. It is important to mention that to reach the probability of $P(n = 1) = 25\%$, perfect photon number resolving detectors and no loss in the optical circuit are required. Despite the fact that implementations will always fall short of the perfect scenario this is motivation enough for the development of a multiplexed heralded single photon source.

3.1.1 Spatial multiplexing

In 2002 Migdall et al. [110] proposed a scheme of spatially multiplexed HSPS to increase the single photon generation rate. Several groups [140–142] have now implemented this approach.

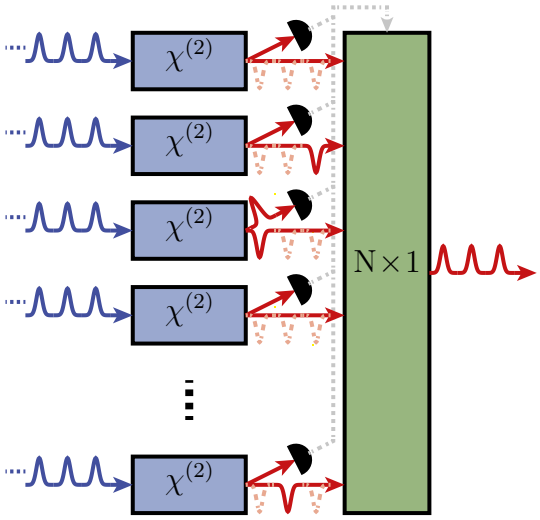

Figure 3.1: Spatial multiplexing schematic: In each of the N photon sources the generation of a photon pair is attempted. The detection of a herald photon identifies the sources that successfully generated a photon and the information is used to set a N×1 switching network to route one heralded photon to the common output port.

The set-up relies on multiple indistinguishable photon pair sources emitting pairs into different spatial modes, as depicted in Fig. 3.1. Heralding detectors register the successful photon emission of each source separately. The $N \times 1$ switching network then routes a successful mode to the common output. In the optimal case, such a source can deliver a single photon at its output in greater than 99 % of attempts for $N \geq 17$.

An implementation of spatial multiplexed single photon sources can profit from the developments and improvements accomplished for normal spontaneous emitting single photon sources by re-using a source design multiple times [110]. Despite this advantage, in most implementations a lot of effort is required to build each individual source, currently limiting experiments to 5 sources [139]. Here, on chip integration of source arrays could improve the development time and maintenance of each individual source [80,140].

A second challenge is the switching network. Current optical switches have losses of ~ 1 dB and switching rates of up to 1 MHz, which overall limits high photon flux rates [108,142].

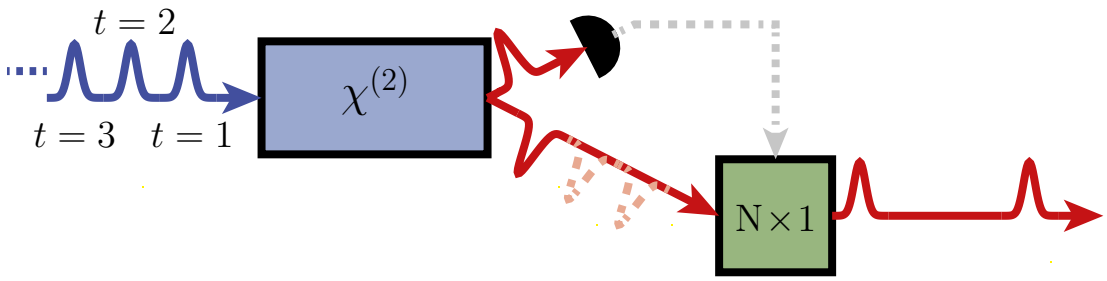

Figure 3.2: A temporal multiplexed single photon source consists of a single photon source which is pumped in multiple time bins to generate single photons. Successful generation is detected in a time resolving herald detector. The N×1 switching network that first stores and then releases the photon at a predefined time can be implemented by a memory or delay loop and a switch.

The simplest N×1 switch design consists of multiple layers of 2×2 switches which combine adjacent spatial modes, reducing the number of modes by a factor of $\frac{1}{2}$ in each layer[143], called log-tree. This approach leads to significant losses due to the fact that photons need to pass through several layers of 2×2 switches. Additionally, an increase in the number of modes requires a larger number of individual 2×2 switching layers, which introduces further losses.

3.1.2 Temporal multiplexing

At the same time, as Migdall et al., Pittman et al.[109] also proposed an approach to multiplexing, based on the temporal degree of freedom. As depicted in Fig. 3.2, multiple attempts in time are undertaken to generate single photons. A memory, often a delay line with a round-trip time matched to the timing interval of the trials in combination with a 2×2 switch, is used as a temporal version of the N×1 switch. Again feed forward control uses the herald detection to store the photon from the appropriate time bin and later release it into the common output time slot. This approach was refined in recent implementations[83,141,144–147].

When studying the details of the temporal multiplexing approach we can find some

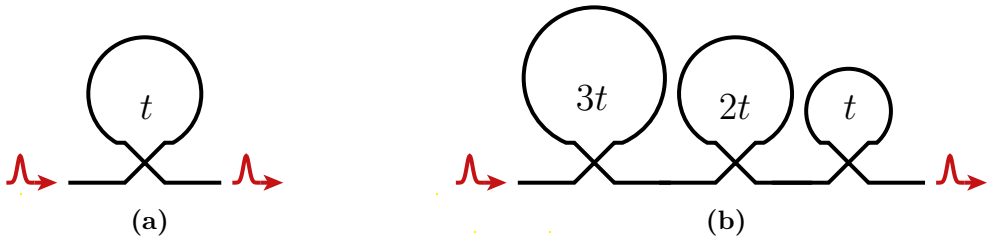

Figure 3.3: Combining several delay lines with varying storage times reduces the number of passes, that a stored photon makes through 2×2 switches. This approach improves optical loss.

advantages compared to the spatial approach. Now only one heralded single photon source is used and the switching network consist of only one switch. This decreases the number of physical resources significantly and eases the design and maintenance of such set-ups. Despite this, multiple passes of the photon trough the switch or the memory lifetime degrades the efficiency with increased storage time. Depending on the design of the storage loop even more passes through the 2×2 switch are needed compared to the spatial approach, where some delay line designs try to mitigate this effect [141], as illustrated in Fig. 3.3. A consequence of the temporal multiplexing scheme is that the internal clock rate of the source needs to be higher with respect to the external clock rate at which photons are released.

3.1.3 Frequency multiplexing

Now we turn our attention to the frequency multiplexing scheme on which the results presented in this thesis are based. As in the temporal multiplexing approach only a single source generates a photon pair spontaneously, as can be seen in Fig. 3.4. Instead of combining several time bins, the joint spectrum of this source is now designed in such a way that multiple spectral modes may emit photons. A spectrally resolved heralding measurement identifies the modes that successfully generated photons. The N×1 switch acts on the spectral degree of freedom and shifts the emitted photon into the common output spectral

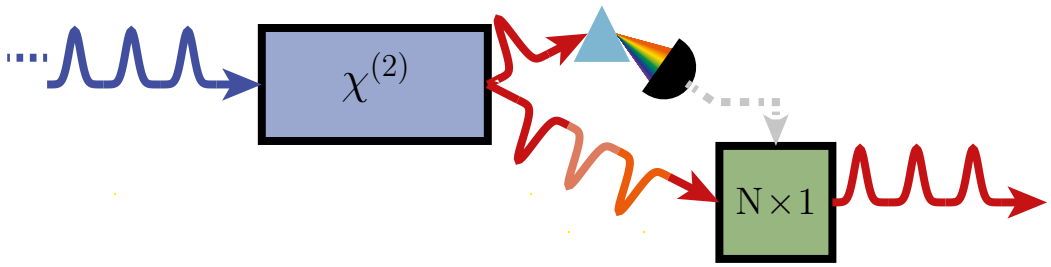

Figure 3.4: A frequency multiplexed single photon source probabilistically generates photons in different frequency bins. Spectral resolved herald detection determines which frequency bin successfully generated a photon. The information of the successful photon creation is passed to the N ×1 switch which shifts the according frequency bin to the pass-band of a output filter.

mode of the multiplexed source.

Compared to the previous two approaches, this scheme now requires a specific source design which is not usually used for HSPS. In addition, a different kind of heralding detector is needed to spectrally resolve the herald photons. A drawback of a more complex heralding detector is, that it is likely to be less efficient compared to the previously employed detectors, adding to the loss budget. An advantage of this scheme in comparison to the previous ones lies in the switch. It interacts only once with the photon and the loss is in principal independent of the number of multiplexed modes. In this, as well as the following chapters, we will study the implementation of a frequency multiplexed source. Similar approaches to frequency multiplexing to the one presented in this thesis have been published recently by Puigibert et al.[148] and C Joshi et al.[149].

3.2 Modelling the components of the frequency multiplexed single photon source

Now we take a closer look at the specific components required to build a frequency multiplexed source and introduce their behaviour in a theoretical model. For this we first describe

the adaptations made to the down-conversion source before we look at the frequency resolved herald measurement and the frequency switch.

3.2.1 Frequency correlations and the Joint Spectral Amplitude

In the previous chapter we learned that pure heralded single photon sources are optimised for as little correlations as possible to ensure that pure single photons are heralded. For a frequency multiplexed source, a different approach is followed. Instead spectral correlations are purposefully introduced to generate photons in different frequency modes. The properties of the non-linear material determines the orientation and shape of the phase-matching function, see Section 2.1.2. One such example is type-0 phase-matched PDC in a KTP crystal, which gives rise to spectral correlations as desired for a frequency multiplexed source.

In type-0 phase-matched processes the pump field as well as the signal and idler fields share the same linear polarisation. This leads to a phase-matching function which is anti-correlated with a slope of $-45°$ in the signal and idler frequency plane. In Fig. 3.5 the JSI function for this case is displayed. The phase-matching, as well as the pump-envelope function, overlap over a wide spectral range leading to a long extend of spectral correlations. The simulation of the JSI function uses the Sellmeier equation for KTP [150,151] that describes the refractive index in the z-direction through the crystal.

$$n_z(\lambda) = \sqrt{3.3134 + \frac{0.05694}{\lambda^2 - 0.05658} - 0.01682\lambda^2}. \tag{3.2}$$

The chip length is 3.29 mm and the pump field is centred at 775 nm with a bandwidth of 0.12 nm.

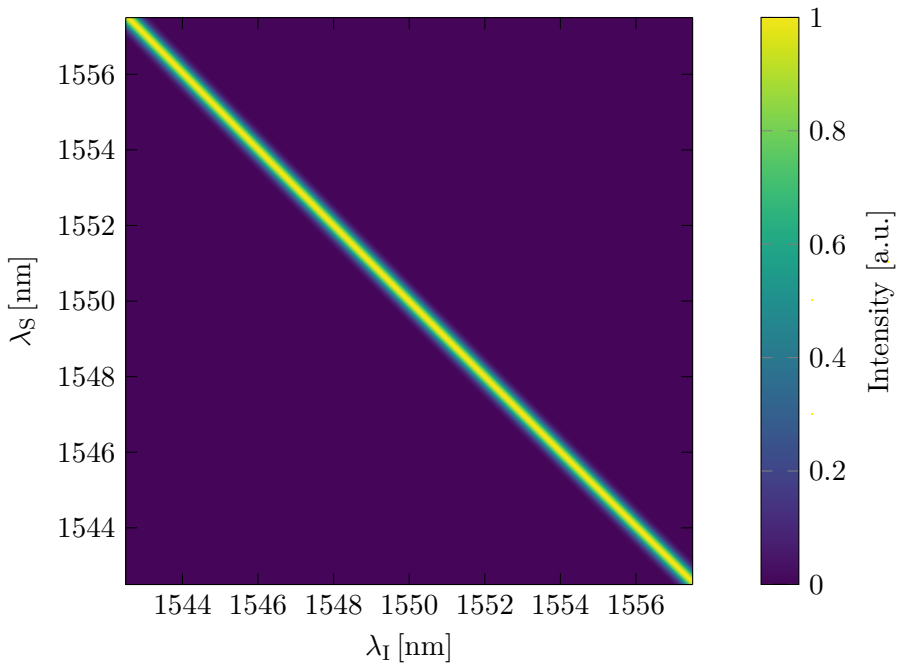

Figure 3.5: In type-0 SPDC all fields have the same polarisation and the phase-matching function for KTP crystals is parallel to the pump-envelope function over a large range in the signal and idler frequency plane.

3.2.2 Spectrally resolved heralding

As shown in Chapter 2.1.3 the correlated output spectrum of the photon source leads to mixedness in the heralded output state. To prevent this impurity, we want to gain all possible information from the herald measurement, in particular, we want to measure the frequency information of the herald photon.

One way of measuring the frequency of photons from a pulsed non-linear process is a Time of Flight (TOF) spectrometer[152]. A schematic of the TOF spectrometer is displayed in Fig. 3.6. Photons are generated in the non-linear crystal by a pulsed pump laser. This pulse train also serves as a time reference for the spectrometer. The generated photons propagate through a dispersive element and experience frequency dependent group velocity dispersion, which delays the photons with respect to the reference clock. A time

Figure 3.6: An optical pulse propagates through a dispersive element, i.e. a chirped Bragg grating. Depending on its spectral properties the pulse is chirped and acquires a time delay with respect to a reference clock. By measuring the arrival time of the optical pulse spectral information is gained, due to the induced temporal spectral correlations.

resolved measurement made with respect to the reference clock then reveals the frequency information. The spectral correlation between the signal and idler fields allows one to determine the frequency of the signal photon form the result of the frequency measurement on the heralding idler photon.

We will now take a brief look at the mathematical description of the spectrally resolved herald measurement and the consequences for the heralded state purity. In the previous chapter we derived the expression for the heralded state (2.30) without frequency resolution. If, in turn, a perfect frequency resolving detector heralds a photon of frequency ω the projection operator $\hat{\Pi}_{\mathrm{I}}(\omega)$ for the spectral resolved measurement of the idler photon is given by

$$\hat{\Pi}_{\mathrm{I}}(\omega) = \hat{a}_{\mathrm{I}}^{\dagger}(\omega)\,|vac.\rangle\langle vac.|\,\hat{a}_{\mathrm{I}}(\omega)\,. \tag{3.3}$$

The measurement therefore projects the heralded signal photon into the state given by

$$\begin{aligned}\hat{\rho}_{\mathrm{S}} &= \mathrm{Tr}\left(\hat{\Pi}_{\mathrm{I}}(\omega)\,\hat{\rho}_{\mathrm{pair,out}}\right)_{\mathrm{I}} \\ &= N\int \mathrm{d}\omega_{\mathrm{S}}\,\mathrm{d}\omega'_{\mathrm{S}}\,F(\omega_{\mathrm{S}},\omega)\,\hat{a}_{\mathrm{S}}^{\dagger}(\omega_{\mathrm{S}})\,|vac.\rangle\langle vac.|\,\hat{a}_{\mathrm{S}}\left(\omega'_{\mathrm{S}}\right)F^{*}\left(\omega'_{\mathrm{S}},\omega\right),\end{aligned} \tag{3.4}$$

with the normalisation constant N. In the experiment the spectrally resolved measurement is not perfect due to jitter on the arrival time measurement. This converts the heralded state into a incoherent mixture of possible detection outcomes ω_{H}, given by the probability distribution $P(\omega|\,\omega_{\mathrm{H}})$. This probability distribution of heralding a photon of frequency ω given that the measurement outcome is ω_{H} can as good approximation be a Gaussian function such as

$$P(\omega|\,\omega_{\mathrm{H}}) = \frac{1}{\sqrt{2\pi}\sigma_{\mathrm{TOF}}} \exp\left(-\frac{(\omega-\omega_{\mathrm{H}})^2}{2\sigma_{\mathrm{TOF}}^2}\right), \tag{3.5}$$

where σ_{TOF} is defined by the spectrometer resolution due to temporal jitter of the detector and time-tagger module. By taking the detection jitter into account the heralded state is now given by

$$\hat{\rho}_{\mathrm{S}} = N \int \mathrm{d}\omega\, P(\omega|\,\omega_{\mathrm{H}}) \int \mathrm{d}\omega_{\mathrm{S}}\, \mathrm{d}\omega'_{\mathrm{S}}\, F(\omega_{\mathrm{S}},\omega)\, \hat{a}_{\mathrm{S}}^{\dagger}(\omega_{\mathrm{S}})\, |vac.\rangle\langle vac.|\, \hat{a}_{\mathrm{S}}\left(\omega'_{\mathrm{S}}\right) F^*\left(\omega'_{\mathrm{S}},\omega\right). \tag{3.6}$$

The resulting purity of the heralded state is therefore

$$\mathcal{P} = \mathrm{Tr}\left(\hat{\rho}_{\mathrm{S}}^2\right)_{\mathrm{S}} = |N|^2 \int \mathrm{d}\omega\, \mathrm{d}\omega'\, P(\omega|\,\omega_{\mathrm{H}})\, P\left(\omega'\middle|\,\omega_{\mathrm{H}}\right) \left| \int \mathrm{d}\omega_{\mathrm{S}}\, F(\omega_{\mathrm{S}},\omega)\, F^*\left(\omega_{\mathrm{S}},\omega'\right)\right|^2. \tag{3.7}$$

With the mathematical framework we have developed so far we can now investigate how the pump bandwidth and the resolution of the TOF spectrometer effect the purity of the heralded photon. In Fig. 3.7 this trade-off is displayed. For a fixed TOF resolution an increase in pump bandwidth increases the purity of the heralded state. Accordingly, for a fixed pump bandwidth, a higher resolution of the TOF spectrometer increases the purity of the heralded photon. In Chapter 4 we will learn how well the experiment performs with

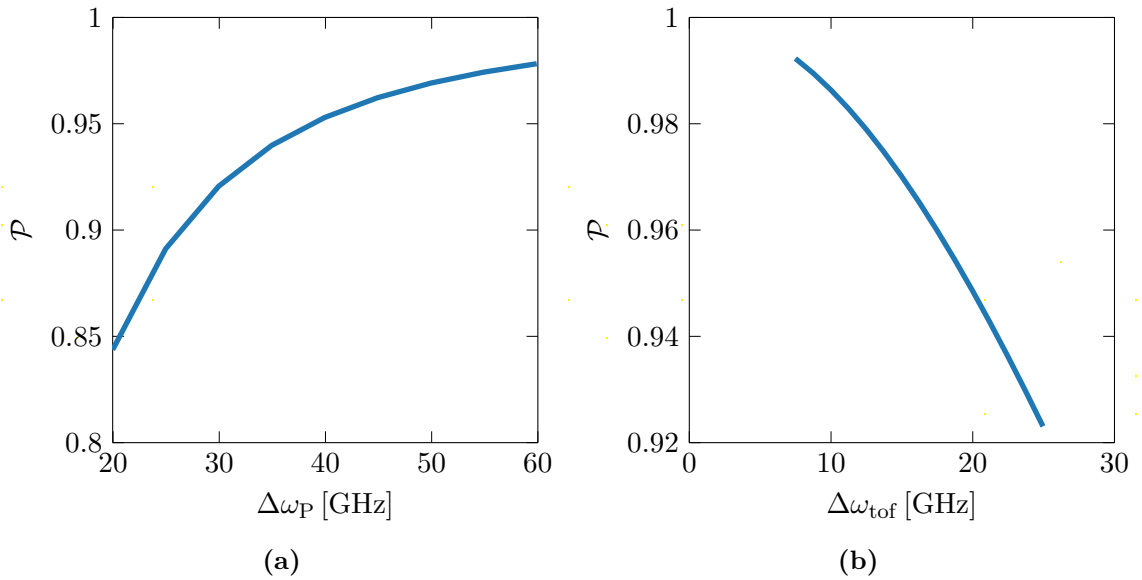

Figure 3.7: Selecting the pump bandwidth and the resolution of the TOF spectrometer determines the purity of the heralded photon state. In (a) the pump bandwidth is varied with respect to a fixed spectrometer resolution of 12.7 GHz whilst in (b) the TOF resolution is varied respectively with a fixed pump bandwidth of 59.9 GHz.

respect to this measure.

3.2.3 Applying a frequency shift

The third crucial component of the frequency multiplexed source is the switch or the implementation of the frequency shift which we will discuss now. For simplicity we mathematically describe here the translation of a Gaussian function. We define a Gaussian wave-packet in the spectral domain as

$$\tilde{f}(\omega) = A \exp\left(-\frac{\omega^2}{2\sigma^2}\right), \tag{3.8}$$

with amplitude A and bandwidth σ. Performing the inverse Fourier transformation converts this function into its equivalent in the time domain which is again a Gaussian,

$$f(\tau) = \int \mathrm{d}\omega\, \tilde{f}(\omega) \exp(-\imath\omega\tau) = \sigma \exp\left(-\frac{\sigma^2\tau^2}{2}\right). \tag{3.9}$$

Next, we modulate this pulse by applying a time varying phase $\phi(\tau)$

$$f(\tau) = f(\tau)\exp(\imath\phi(\tau)) \tag{3.10}$$

and perform an inverse Fourier transform back to the frequency domain. The resulting spectrum is in the case of an applied linear phase

$$\tilde{f}'(\omega) = \exp\left(-\frac{(\omega+\phi)^2}{2\sigma^2}\right), \tag{3.11}$$

which is exactly the original pulse translated in frequency by ϕ.

This frequency translation can be implemented by a travelling wave Electro-Optical Modulator (EOM) [153,154]. In the EOM a time-varying electric field modulates the refractive index. The optical pulse propagates at the same speed with this field in the EOM material. Due to the refractive index change, and the same propagation speed, different parts of the optical pulse acquire a different temporal phase. In principle, the amplitude of the electric field can have any temporal shape but in the case of a linear slope it implements a linear frequency translation on the optical pulse as depicted in Fig. 3.8. In the displayed example, the linear section of a Radio Frequency (RF) field is used as the driving electric field. A non-linear field profile applies higher order phase and chirps or compresses the optical pulse [155]. For later discussions we should remember that the applied frequency shift is proportional to the temporal gradient of the electric field profile in time.

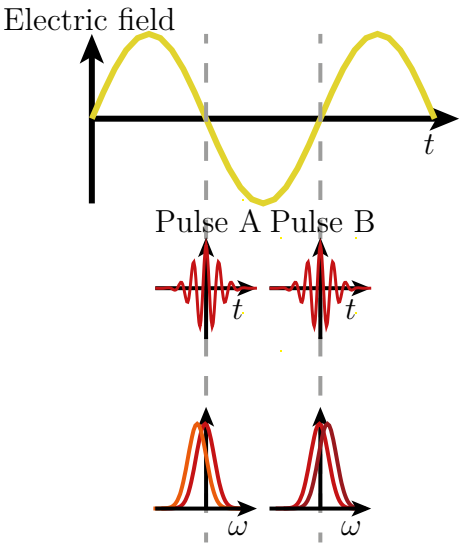

Figure 3.8: The RF signal co-propagates with the optical pulse, modulating the refractive index of the EOM material. This difference of refractive index for different parts of the pulse leads to the accumulation of a time varying phase. The pulse is spectrally shifted if the phase is linear in time.

3.3 Detection and feed forward control

Binary detectors, such as Avalanche Photo-Diodes (APDs) and Superconducting Nanowire Single Photon Detectors (SNSPDs), are most commonly used to detect photons. These are single photon sensitive and able to discriminate between no and at least one photon. Crucially for us, such a detector converts the arrival of a photon at the input of the detector into an electrical pulse at the output. This acts as a triggering event for the feed forward control of the multiplexing source. Feed forward means that information gained from a measurement is used in the apparatus to determine the correct setting of a following operation. For us this is the appropriate amount of frequency shift to apply to the heralded photons.

Looking at Fig. 3.9, we can understand the feed forward step phenomenologically. The detection of a photon in the idler path determines the arrival-time of the herald photon with respect to the reference clock. We can infer the frequency of the detected herald photon due to the arrival-time frequency correlation introduced by the TOF spectrometer.

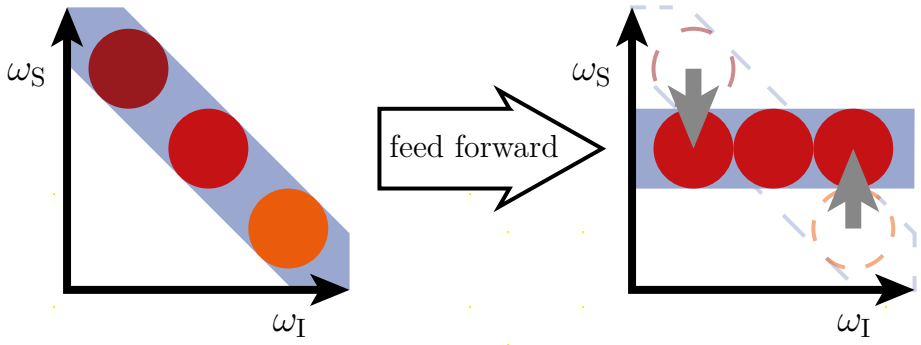

Figure 3.9: To explain feed forward control we simplify the correlated joint output spectrum of the photon source. Photon pairs are created in separate frequency modes which are indicated by different coloured circles. The spectrally resolved herald detection of a photon from one of these modes in the idler arm reveals the frequency of the corresponding signal photon. This information is passed on, fed forward, to set the required frequency shift. Shifting each generated photon by the correct amount, results in a new *effective* joint output spectrum with the frequency information of the signal erased.

By also taking the frequency correlation between signal and idler photons into account, feed forward logic determines the appropriate settings to shift the signal photon. For each herald detection event, the associated signal photon is translated to the output frequency window, while other photons that might have been generated in other frequency bins are rejected by a bandpass filter centred on the frequency of the output mode. Spectral shifting and feed forward control erases the spectral information of the signal photon, which was initially captured by the spectral correlations. The plot, right hand side of Fig. 3.9, of the signal and idler frequency after taking feed forward control into account shows no spectral correlations. Exercising this control over a specific shifting range leads to the expected *effective* joint spectrum as the schematic in Fig. 3.9 indicates.

3.4 The impact of imperfections

Any experimental realisation of a photon source will suffer from experimental limitations and imperfections. Their effect on the source performance can be classified into two groups:

imperfections reducing the purity of the emitted photon and imperfections leading to photon loss from the output channel.

First we will look at imperfections that deteriorate the purity. As we discussed in a previous Section 3.2.2, we saw that the relationship between the spectral herald resolution and the pump bandwidth have a direct influence on the heralded photon purity. Any imperfection in the pump preparation, especially with regard to its spectral bandwidth, will change the photon purity. A decrease in the TOF spectrometer resolution, e.g. due to additional jitter in the herald detection or reference timing, will reduce the purity.

Besides the TOF spectrometer and the heralding detection, imperfections can arise in the RF electronics driving the frequency translation. Amplitude and phase fluctuations will lead to incorrect frequency shifting, increasing the distinguishability of photons emitted on consecutive pump pules. A similar effect is caused by dark-counts, these act as spurious herald events leading to erroneous frequency shift settings. Dark-counts are a concern if their rate is very high compared to the photon pair emission rates or if the photon pair emission probability is high, such that a photon in the signal path is usually present when a dark-count event occurs. More generally, the feed forward electronics could be calibrated incorrectly such that the frequency shifts are wrong. Besides shifting the photon by an unsuitable amount, an erroneous setting can also add chirp to the shifted photon. This again increases the distinguishability of consecutive photons. A very grave problem could arise if the feed forward logic has a larger latency than expected or is not prepared to manage high count rates, both of which lead to incorrect frequency shifts.

All these imperfections can reduce the purity of the heralded photon but can also have

a second effect when combined with the output filter. In that case, shifting photons insufficiently or too far results in loss when the photon is rejected by the output filter. In addition to the loss mechanisms already mentioned above, all components introduce some loss. There are two kinds of inefficiencies that one can distinguish: loss of the herald and loss of the signal photons. The loss of the signal photon is more serious since it leads to no photon emission when one expects a photon to be present, reducing the heralding efficiency. Herald loss results in the failure of a single trial, which can be compensated by the use of more modes. Nevertheless, it decreases the overall performance of the multiplexed source.

Since loss is very relevant for the photon detection statistics, we will now include it in the model. To simplify the calculations we assume constant loss for all modes κ in the signal mode and constant loss for the herald mode. When losing m out of n photons we have to include all permutations of modes to calculate the probability of generating $n-m$ photons. The probability distribution for multiple modes with constant loss is given by

$$P\left(r,n,\kappa,\eta\right)=\sum_{m=n}^{\infty}\binom{m}{n}\eta^{n}\left(1-\eta\right)^{m-n}P\left(r,n,\kappa\right), \tag{3.12}$$

where $\binom{m}{n}$ is the Binomial distribution, η is the efficiency and $1-\eta$ the probability of loosing one photon. With this expression we can directly derive a formula for the herald detection probability P_{H} and for the coincidence detection probability P_{CC}

$$P_{\mathrm{H}}\left(r,\kappa,\eta_{\mathrm{H}}\right)=1-P\left(r,n=0,\kappa,\eta_{\mathrm{H}}\right), \tag{3.13}$$

and

$$P_{\mathrm{CC}}\left(r,\kappa,\eta_{\mathrm{S}},\eta_{\mathrm{H}}\right)=\sum_{n=1}^{\infty}P\left(r,n,\kappa\right)\left(1-\left(1-\eta_{\mathrm{S}}\right)^{n}\right)\left(1-\left(1-\eta_{\mathrm{H}}\right)^{n}\right), \tag{3.14}$$

where η_S, η_H are the signal and herald path efficiencies. The coincidence detection probability is the product of the probability of generating n photons multiplied by the probability of not losing all signal and herald photons. Figure 3.10 compares various different probabilities of detecting n photons from κ modes with 1 % and 50 % loss. Increasing the number of modes increases the probability of generating a single photon in only one mode for constant loss, Fig. 3.10a. This improvement is even more striking if the probability of detecting a single photon from at least one source is depicted, Fig. 3.10b. An ideal multiplexing source harnesses this advantage with photon number resolving detectors and reduces the impact of higher photon numbers at the same time. Figures 3.10c and 3.10d display the heralding and coincidence detection probability for the same scenarios where photon number resolution is not available. Both probabilities increase with additional modes where the impact of loss is stronger on P_{CC} since two modes are affected instead of just the herald mode. In the scenarios of the later two figures, where no photon number resolution is available, it is necessary that the source operates in the low squeezing limit such that higher order photon numbers do not deteriorate the output state. Nevertheless it is apparent that additional modes compensate for loss. The number of modes necessary to compensate a certain amount of loss is displayed in Fig. 3.11 for equal efficiencies η for the signal and herald path. With increased efficiency the number of required modes decreases significantly.

In a further step we now want to see how loss affects the $g_H^{(2)}$ measurement. To derive this equation we first need to know the probability of detecting n photons given a herald photon has been detected. This is given by

$$P\left(r, n, \kappa, \eta_S \middle| \, \mathrm{H}, \eta_H\right) = \frac{\sum_{m=n}^{\infty} \binom{m}{n} P\left(r, m, \kappa\right) \eta_S^n \left(1-\eta_S\right)^{m-n} \left(1-\left(1-\eta_H\right)^m\right)}{P_H\left(r, \kappa, \eta_H\right)}. \tag{3.15}$$

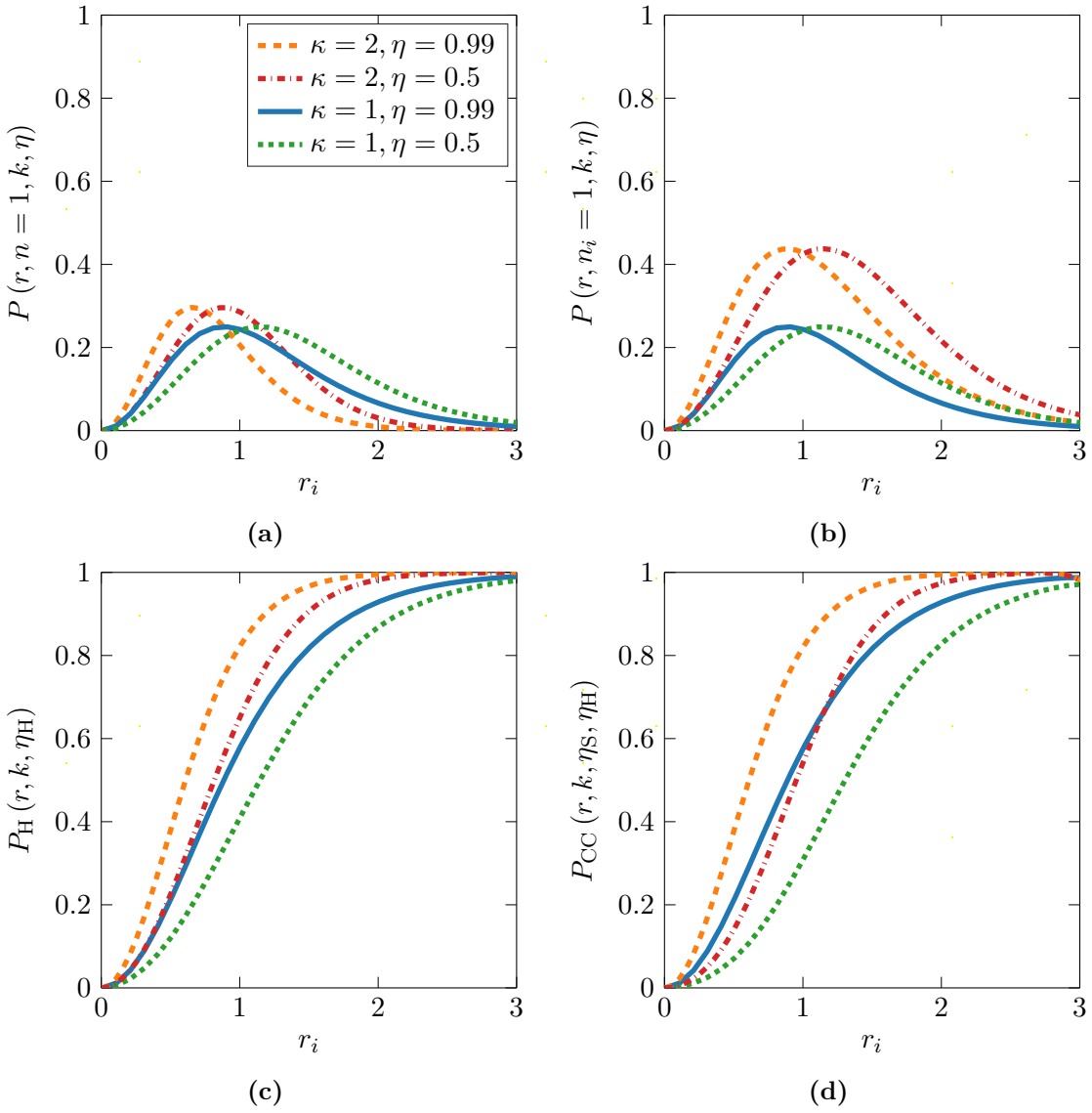

Figure 3.10: (a) the probability of detecting $n = 1$ photon for $\kappa = 1$ or 2 modes with a total detection efficiency of $\eta = 99\,\%$ or $50\,\%$ in the herald and signal path. (b) shows the probability of detecting one photon from at least one mode, i, assuming photon number resolution as in (a). This clearly demonstrates the advantage of multiplexing. (c-d) show the corresponding herald and coincidence detection probabilities, without photon number resolving detectors. All probabilities are displayed with respect to the squeezing per mode $r_i = \frac{1}{\kappa} r$ which is the same for all modes. The solid blue line corresponds to $(\kappa = 1, \eta = 0.99)$, the dashed orange line to $(\kappa = 2, \eta = 0.99)$, the dotted green line to $(\kappa = 1, \eta = 0.5)$ and the dashed dotted red line to $(\kappa = 2, \eta = 0.5)$.

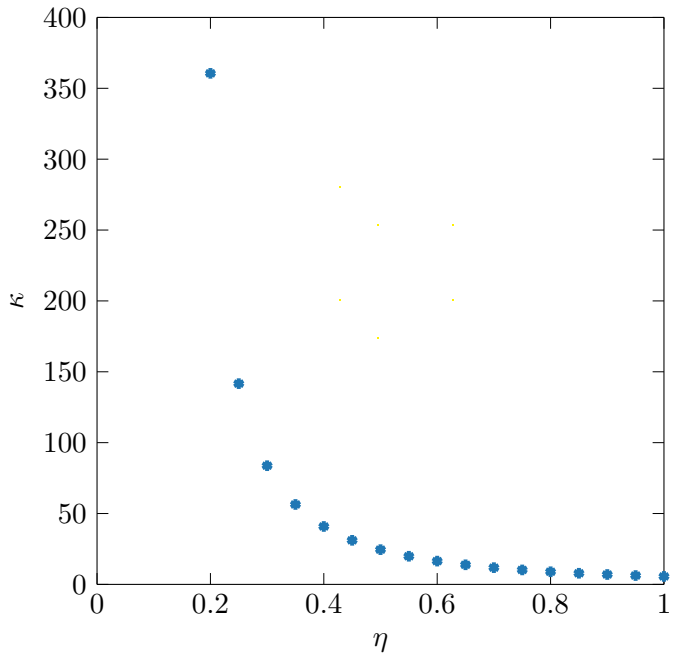

Figure 3.11: For a constant coincidence detection probability of 20 % the number of modes must increase significantly to compensate for lower signal and herald path efficiencies. A constant squeezing of $r = 0.2$ is assumed.

With loss the $g_{\mathrm{H}}^{(2)}$ is then stated as

$$g_{\mathrm{H}}^{(2)}(0) = \frac{\sum_{n=2}^{\infty} n\,(n-1)\,P\left(r, n, \kappa, \eta_{\mathrm{S}} | \,\mathrm{H}, \eta_{\mathrm{H}}\right)}{\left(\sum_{n=1}^{\infty} n\,P\left(r, n, \kappa, \eta_{\mathrm{S}} | \,\mathrm{H}, \eta_{\mathrm{H}}\right)\right)^2}. \tag{3.16}$$

To understand the consequences of loss we compare again the case of 99 % efficiency to the one with 50 % efficiency in Fig. 3.12. In Fig. 3.12a the $g_{\mathrm{H}}^{(2)}$ is larger for the multi mode case. This is understandable if one keeps in mind that $r_i = r\lambda_i$. Higher photon numbers are therefore much more likely to occur in an output to which two modes with equal squeezing contribute than just one mode of the same squeezing strength. To account for this Fig. 3.12b depicts the $g_{\mathrm{H}}^{(2)}$ versus the total squeezing r. When looking at Fig. 3.12c or 3.12d it becomes apparent that loss can easily destroy the advantage gained by multiplexing if inefficiencies are not kept at a similar level as for a non multiplexed source.

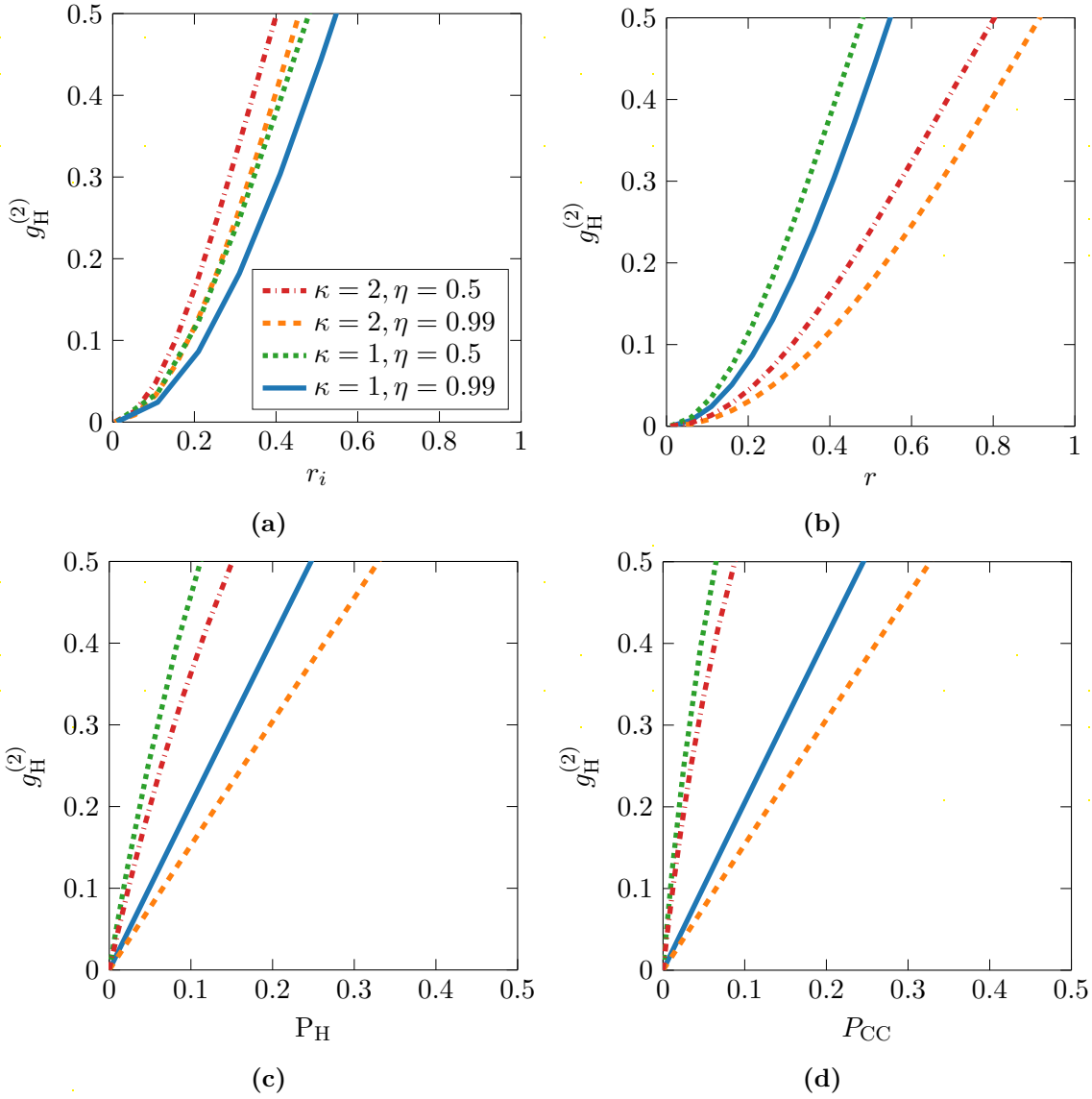

Figure 3.12: (a) displays the $g_{\mathrm{H}}^{(2)}$ versus the squeezing parameter per mode r_i for $\kappa = 1, 2$ modes contributing to the output statistics and 1 % or 50 % loss. (b) depicts the same scenario versus the total squeezing r. (c) and (d) again display the $g_{\mathrm{H}}^{(2)}$ with respect to the herald and coincidence detection probability. The solid blue line corresponds to $(\kappa = 1, \eta = 0.99)$, the dashed orange line to $(\kappa = 2, \eta = 0.99)$, the dotted green line to $(\kappa = 1, \eta = 0.5)$ and the dashed dotted red line to $(\kappa = 2, \eta = 0.5)$.

One can try to compensate for loss by stronger squeezing to increase the photon emission. This can only be done with caution since it will deteriorate the photon statistics, as is visible in the increased $g_{\mathrm{H}}^{(2)}$ due to a larger impact of higher photon number components.

Another significant imperfection of an experimental implementation is the use of single binary detectors instead of photon number resolving detectors. This forces any implementation to work in the weak squeezing regime where higher photon emissions are unlikely, but also single photon emission is rare. Fast photon number resolving detectors could mitigate this problem in the future.

3.5 Summary

In this chapter we focused on the conceptual details of multiplexed sources with an emphasis on frequency multiplexing. We have discussed the essential components needed to realise a frequency multiplexed source. With these principal components in place we turned our attention back to the theoretical description of purity and photon statistics. We studied how the introduction of lossy components into the theoretical framework allows us to describe the expected behaviour of the multiplexed source. In the next two chapters we will look at the experimental set-up and its characterisation which will allow us to add specific values to parameters in the model.

Chapter 4

The frequency multiplexing set-up

In this chapter we will now discuss the implementation of a frequency multiplexed single photon source. We will address the choices and expected performance of the components. A detailed schematic gives an overview of the experiment in Fig. 4.1. We will consider each part of the set-up individually in the following Sections.

4.1 Source chip and pulsed pump field properties

As a first block we will consider the photon generation with the pump preparation and the optical non-linear material as its main components. A z-cut periodically poled KTP crystal forms the non-linear material for the photon source chip. The poling period Λ phase-matches type-0 PDC. The chip has 5 groups of rubidium in-diffused waveguides, as schematically indicated in Fig. 4.2. Each group consists of two sets of three waveguides alternating in width between $2\,\mu$m, $3\,\mu$m, and $4\,\mu$m. Waveguides confine the pump and daughter fields, such that a higher source brightness, in comparison to a bulk, non-waveguided, source can be achieved. The chip length is 3.29 mm yielding the phase-matching function as displayed

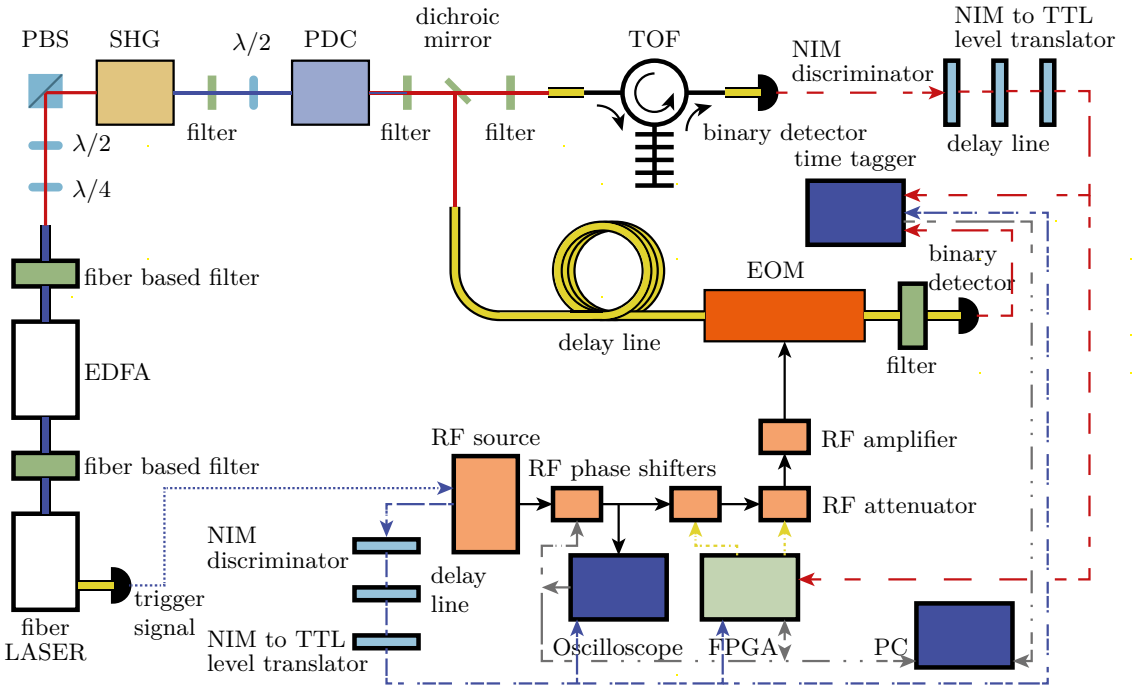

Figure 4.1: Detailed schematic of the frequency multiplexing single photon source set-up: Starting on the bottom left hand side the output of a pulsed laser system passes an amplification and filtering stages. A following SHG stage frequency doubles the beam to form the pump field for the SPDC process. The TOF spectrometer measures the herald mode output of the SPDC process. A FPGA processes the herald detection event and adapts the feed forward settings of the RF signal driving the EOM. A delay line holds up the signal photon to compensate for the latency of the feed forward logic. At the output of the frequency multiplexed single photon source the frequency shifted signal photon passes a bandpass filter, selecting the output mode.

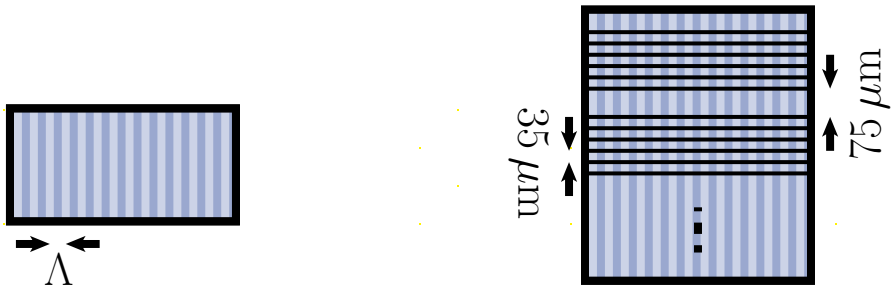

Figure 4.2: The KTP chip layout indicating the periodic poling and its periodicity Λ (a) and the waveguide arrangement and spacing (b).

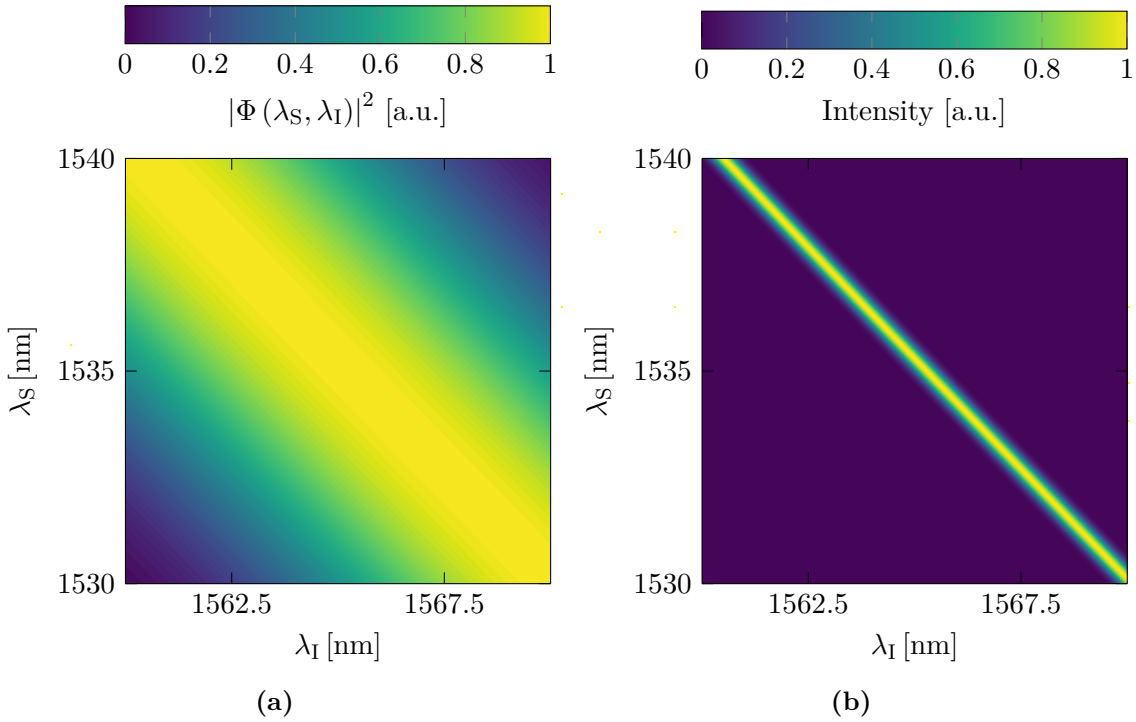

Figure 4.3: The phase-matching function for type-0 PDC in KTP (a) and the resulting correlated JSI (b) for a pump field centred at 775 nm are orientated along the $-45°$ diagonal with respect to the signal and idler wavelength.

in Fig. 4.3a. For a pump field centred at 775 nm the PDC process is degenerate at 1550 nm. Combining the pump envelope and phase-matching functions leads to the JSI depicted in Figure 4.3b. A dichroic mirror separates the signal and idler fields at the degeneracy point, such that the frequency multiplexed source operates ~ 15 nm away from that point. Working in the telecommunication band is beneficial due to a variety of relatively inexpensive and low loss off-the-shelf components which are optimized for the telecommunication industry.

4.1.1 The pump field preparation

The pump field preparation starts with a customized erbium-doped fibre laser emitting Femtosecond (fs) laser-pulses at a repetition rate of 10 MHz. A separate housing for the fibre cavity thermally decouples it from ambient temperature variations and stabilises the

Specification	Value
Repetition rate	10 MHz
Central wavelength	1560 nm
Bandwidth	30 nm
Output power	42 mW
Pulse duration	80 fs

Table 4.1: The pump laser specifications.

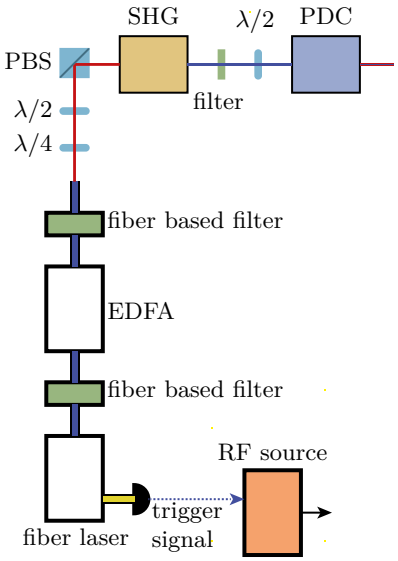

Figure 4.4: The output of the fibre laser is filtered and re-amplified before it is converted to the required pump field wavelength in a SHG stage. The converted field drives the non-linear process in the PDC chip. A photodiode detects a signal from the laser monitor output and generates a reference clock.

repetition rate of the laser to within ±200 Hz. Table 4.1 summarises the specifications of this laser system. A photodiode picks up a signal from the laser monitor output to provide a reference clock for the experiment, as can be seen on the bottom right of the magnified set-up view in Fig. 4.4. Band pass filters reduce the laser output bandwidth to ∼ 60 GHz and an Erbium-Doped Fibre Amplifier (EDFA) re-amplifies the field. Following the amplification a filter removes spectral broadening and the polarisation is optimized to be linear. A Second-Harmonic Generation (SHG) process in periodically poled LN converts the 1550 nm pump laser to 775 nm. The remaining 1550 nm fundamental is rejected by a short-pass filter and

Specification	Value
Repetition rate	10 MHz
Central wavelength	775 nm
Bandwidth FWHM	0.12 nm or 60 GHz
Output power	$\sim$ 2 mW
Pulse duration	7.36 ps

Table 4.2: The pump field properties driving the SPDC process.

the 775 nm pump light drives the type-0 SPDC process in the KTP chip. Additional filters are used after the source to remove the residual pump light and split the signal and herald fields.

The optimal pump Full Width at Half Maximum (FWHM) bandwidth to generate photons with a purity of at least 90 % after heralding, with the TOF spectrometer, and a maximal number of modes in a certain spectral range is $\sim$ 25 GHz or $\sim$ 0.05 nm at the pump wavelength of 775 nm, according to the calculations of Section 3.2.2.
As we will see in the next Chapter 5.1 building a filter that narrows the pump bandwidth to this extent is challenging and adds significant losses to the set-up. Due to this reason the pump bandwidth was later increased to about 60 GHz or 0.12 nm at the pump wavelength. A summary of the pump field properties is given in Table 4.2.

4.2 Photon detection and the frequency resolved heralding measurement

In this thesis single photon sensitive detectors acting as binary detectors register the generated photons. We will therefore shortly review the working principles of the used single photon sensitive detectors.

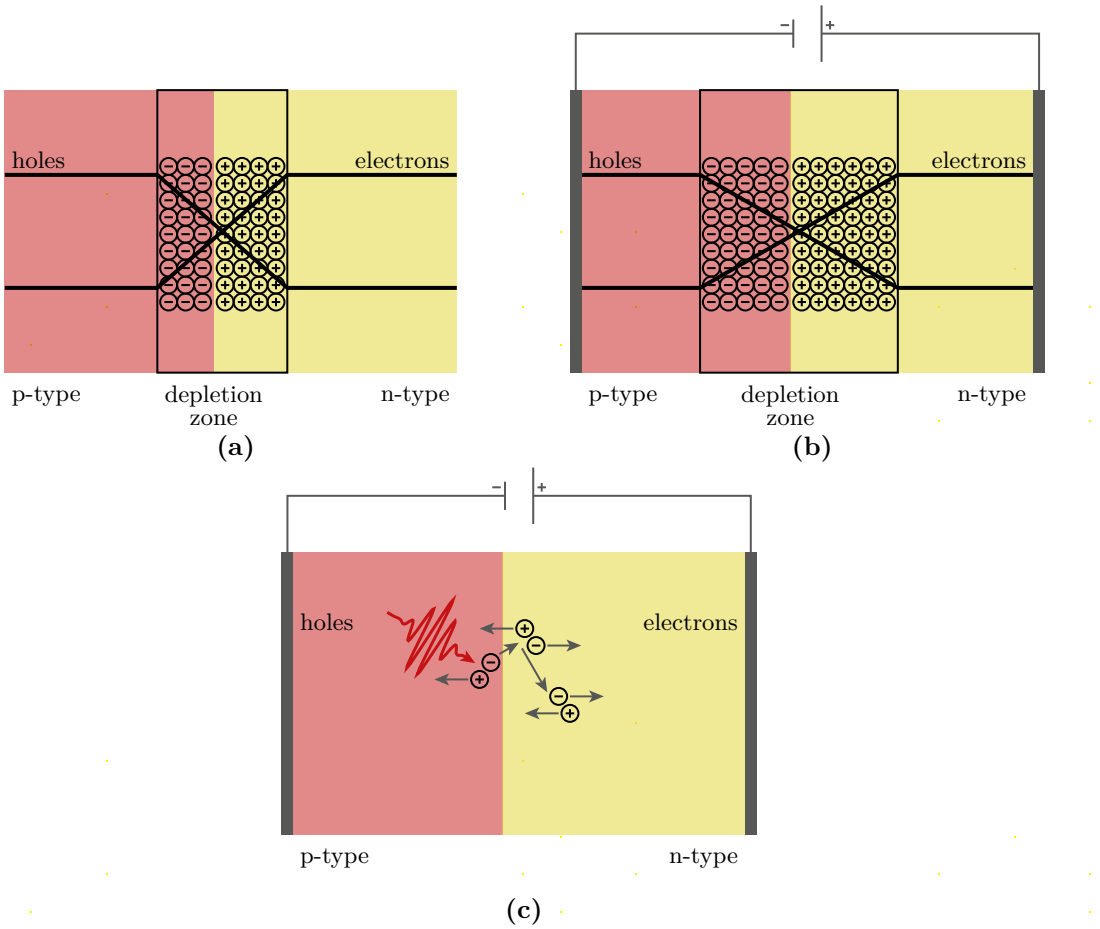

Figure 4.5: The charge carrier distribution in the depletion zone of a pn-junction in the neutral state balances the electrical potentials (a). If a reverse bias is applied to the pn-junction, the depletion zone increases (b). An absorbed photon in the depletion zone creates a electron-hole pair and an electric avalanche effect is initiated. The current build up of the avalanche amplifies the signal to a steady current.

4.2.1 Photon detection

In single photon experiments Avalanche Photo-Diodes are commonly used [56]. A semiconductor structure called a pn-junction forms the central element of an APD as depicted in Fig. 4.5. Two adjacent regions of a doped semiconductor form the pn-junction. The p-type region is doped such that it has an excess of holes, missing electrons, and the n-type region has an excess of negative charge, i.e. electrons. Along the interface of these two regions electrons and holes cross over to balance the potential difference and form the depletion zone, as

in Fig. 4.5a. Electrodes on either side of the junction apply an additional bias potential. In the reverse bias configuration the voltage of this potential is above the avalanche breakdown point [156]. The bias potential draws the electrons in the n-type side and the holes in the p-type side away from the interface increasing the potential difference, leading to a larger depletion zone, as depicted in Fig. 4.5b.

If a photon is absorbed in the pn-junction, an electron-hole pair is created. The free electron accelerates towards the anode and the hole is drawn towards the cathode by the applied bias voltage. While moving, they undergo collisions with other bound electrons in the lattice and create new electron-hole pairs. This causes an avalanche process, amplifying the initial single electron to a constant current of many electron-hole pairs, effectively triggering the binary detector. A quench discharges the bias voltage and stops the avalanche process.

APDs are relatively inexpensive and have basically no additional requirements. At most they are cooled by a Peltier or thermoelectric cooler. For these reasons, APDs are common detectors in quantum optics. For this experiment, the most relevant detectors are Indium Gallium Arsenide (InGaAs) APDs, which are sensitive between $1 - 1.65\,\mu$m and have a peak detection efficiency of about $20\,\%$. The detection efficiency is the efficiency of converting an absorbed photon to a detection event.

A drawback of InGaAs APDs is their relatively high dark-count rate. Dark-counts are spurious noise events. These spurious detection events can arise from background radiation which couple to the detector, or thermal excitations that trigger an avalanche not due to a photon. Another effect present in APDs is after-pulsing. After-pulsing is a false detection event with a characteristic time offset to a previous avalanche. Charge carriers trapped in

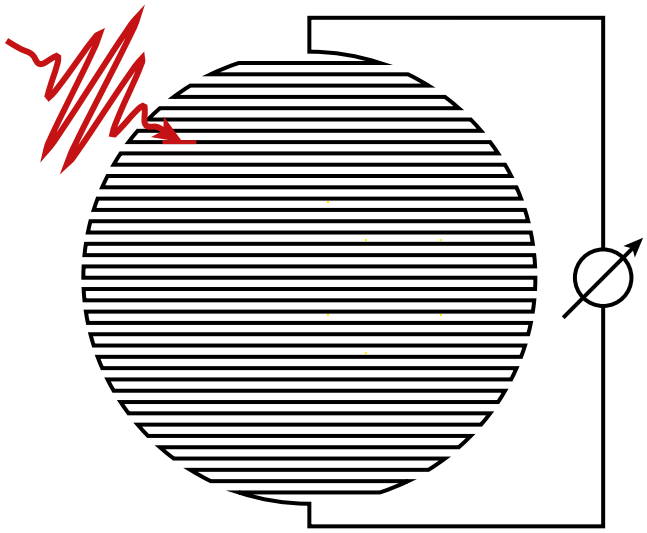

Figure 4.6: A nanowire is a small meandering superconducting wire. If a photon is absorbed the material heats up and losses superconductivity. This sudden increase in resistivity establishes the detection event.

the depletion zone, following the first avalanche, are freed and induce a second avalanche once the reverse bias is re-established after a quench. To reduce the amount of remaining charge carriers and ensure that the avalanche has died out completely a hold off time on the order of $10\,\mu$s is necessary, reducing the maximal count-rate at which photons can be detected to $100 \cdot 10^3$ counts per second.

One alternative to APDs, which is now becoming commercially available, are Superconducting Nanowire Single Photon Detectors[56,157]. A SNSPD is a thin meander of superconducting material such as Tungsten Silicide (WSi), see Fig. 4.6. A current biases the nanowire close to its superconducting to normal threshold current such that it is still superconducting. If the nanowire absorbs a photon a small section of the wire heats up and becomes resistive. This abrupt change in resistivity is measured and amplified. The nanowire cools back down and once more becomes superconducting[158]. At this point another photon can be detected. A benefit of SNSPDs, is their high detection efficiency of

Specification	InGaAs APD	SNSPD
Detection efficiency	$\sim 20\%$	$\sim 80\%$
Dark-counts	$1 - 2{\cdot}10^3\,\text{counts}{\cdot}\text{s}^{-1}$	$\sim 10\,\text{counts}{\cdot}\text{s}^{-1}$
Spectral range	$1 - 1.65\,\mu\text{m}$	$700 - 1700\,\text{nm}$
Timing jitter FWHM	$150 - 250\,\text{ps}$	$70\,\text{ps}$
Dead time	$10\,\mu\text{s}$	$50 - 100\,\text{ns}$
Special requirements	none	cryogenic temperatures

Table 4.3: Comparison of the properties of InGaAs APDs and SNSPDs

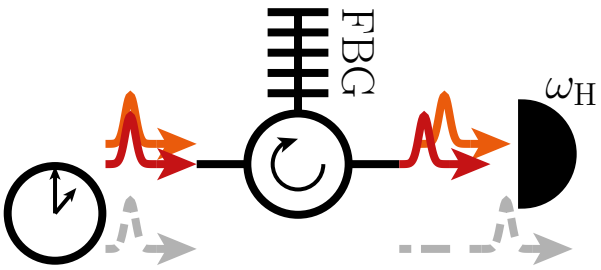

Figure 4.7: A FBG introduces a frequency dependent time delay to an optical pulse. The TOF spectrometer measures the arrival time of a photon with respect to a reference signal and infers the photon frequency.

80% at telecommunication wavelength and their very low dark-count rates of a few photons per second in comparison to InGaAs APDs[159,160]. The main disadvantage is their need to be operated at low temperatures around 1° K. Due to their small detector area SNSPDs can be very fast detectors with high count rates and reset times in the range of $50 - 100\,\text{ns}$. Its dimensions also favour a small temporal jitter of $70\,\text{ps}$[161].

In summary the SNSPD outperforms the InGaAs APD in every respect and is the detector of choice for the frequency multiplexing experiment due to its high efficiency, short dead time, low dark-count rates, and high timing resolution. Table 4.3 summarises the characteristics of the two photon detectors.

4.2.2 The Time of Flight spectrometer

In the previous Chapter 3.2.2, the TOF spectrometer was briefly introduced, here we will

Specification	Value
Loss	$2.33 - 2.89\,\mathrm{dB}$
Dispersion	$-2.3\frac{\mathrm{ns}}{\mathrm{nm}}$
Spectral range	$1525 - 1575\,\mathrm{nm}$

Table 4.4: Summary of the Bragg grating specifications.

discuss its specifications.

The TOF spectrometer comprises of a dispersive element, a binary detector, and a time reference, see Fig. 4.7. In the presented experiment, a chirped Fibre Bragg Grating (FBG) is the dispersive element with a dispersion of $-2.3\frac{\mathrm{ns}}{\mathrm{nm}}$ and a reflection band of $1525-1575\,\mathrm{nm}$. Table 4.4 summarises the properties of the FBG. The role of the dispersive element is to map different frequencies to different times of arrival at the detector. The distribution of time of arrivals is measured using a time-tagger module connected to the output of the detector.

When choosing to use a TOF spectrometer one has to keep in mind that the underlying repetition rate of the experiment has to be balanced with the spectral range and dispersion of the TOF spectrometer. If this is not done adequately, consecutive pulses become overlapped in time, and there is no longer a unique time of arrival for a particular frequency. For the given dispersion and a laser repetition rate of 10 MHz a maximal spectral range of $\sim 43.5\,\mathrm{nm}$ can be measured without overlap.

4.3 Time tagging and feed forward control logic

As we learned before in Chapter 3.3, the feed forward logic processes the heralding detection signal time of arrival and determines the settings of the RF signal to implement the desired frequency shift. The central component for this section of the experiment is the

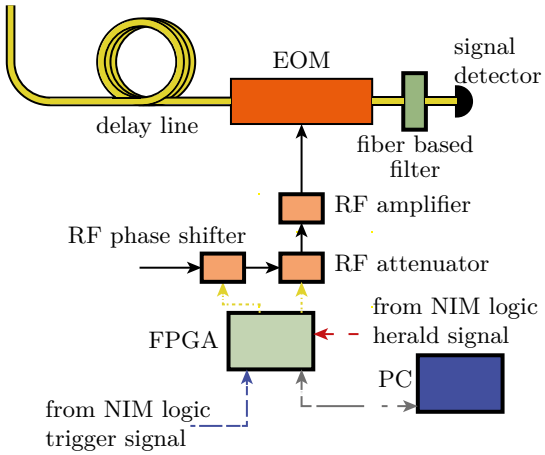

Figure 4.8: The FPGA evaluates the herald detection event timing and sets the amplitude and phase of the RF signal driving the frequency shift.

Field-Programmable Gate Array (FPGA). Programming an FPGA sets physical connections between individual logic component blocks within a specialised Silicon chip. By using a specialized electrical circuit, fast and complex signal processing on a highly integrated platform is possible, exactly what is needed to perform fast feed forward control.

J Tiedau and P Humphreys, who initially worked on the frequency multiplexed source, programmed the FPGA basing their system on the Time to Digital Converter (TDC) core developed by S Bourdeauducq[162,163]. Here, only the important elements of this device are summarized. As depicted in Fig. 4.8, the feed forward process starts with the FPGA receiving a heralding detection signal. In the TDC, the signal propagates in a delay line and in the next internal clock cycle of the FPGA the position to which the signal has progressed is measured. The start-up calibration of the FPGA, an internal routine initiated when the FPGA is turned on, generates a Lookup-Table (LUT) which converts the position in the delay line to time with a higher resolution than the FPGA clock rate. Temperature and voltage changes on the FPGA board can lead to drifts in the propagation speed of signals in the delay line. An online calibration procedure constantly monitors the frequency of ring

oscillators close to the delay line and compensates for these drifts. We use a second input for the reference clock signal to derive a timing difference between the herald detection and the laser trigger. The FPGA TDC core can reach a timing resolution of 33 ps[163]. The latency of the FPGA between a detection event and applying the according feed forward settings is ~ 518 ns, mainly limited by the Data Acquisition (DAQ) board as explained by J Tiedau[163]. The signal photon is delayed in an optical fibre for this processing time before it passes into the EOM.

A Personal Computer (PC) communicates with the FPGA to calibrate and write a second set of LUTs defining the RF phase shifter and attenuator settings with respect to the measured heralding detection timing. The RF phase shifter and attenuator change the RF signal driving the EOM. The EOM implements the corresponding frequency shift and completes the feed forward control circuit. We will discuss in the following chapter how this second set of LUTs is calibrated.

The FPGA requires Low Voltage Transistor-Transistor Logic (LVTTL) signals as input signals, to prevent damage to the board. Neither the reference clock signal nor the detectors provide this signal level. The output pulses from the SNSPDs have an amplitude of ~ 200 mV, whereas the LVTTL signal standard defines an active high between $2.4 - 3.3$ V and a maximum voltage not exceeding 4.5 V. Nuclear Instrumentation Module (NIM) logic modules adapt the pulse levels as depicted in Fig. 4.9. A NIM grid discriminator converts the original signals from the reference clock output of the RF generator and the detector to NIM pulses. NIM grid components have been used extensively in nuclear physics and are based on a pulse standard defining -0.8 V as logical true. Such modules exhibit appropriate timing performances and can easily handle the signal rates of this experiment. An addi-

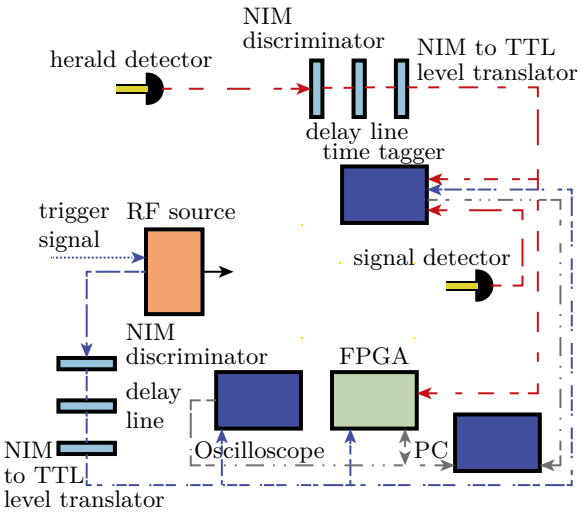

Figure 4.9: NIM modules convert the reference clock and herald detection signals to TTL pulses matching the requirements of the FPGA.

tional delay enables coarse adjustment of the relative timings. The final NIM component converts the NIM pulse to a Transistor-Transistor Logic (TTL) pulse. The output pulse of this module is at the lower edge of the TTL standard and additional loss in the cable to the FPGA reduces the signal amplitude to within the LVTTL standard.

Copies of the same signals are send to a time-tagger which records the measured events.

4.4 The frequency shift of the heralded photon

4.4.1 The electro-optical modulator

In the previous chapter we have already discussed how a frequency shift is obtained using an EOM, see Section 3.2.3. For the choice of an EOM, two properties are essential for the frequency multiplexed source: low optical loss and a large shifting range. These two objectives cannot be fully satisfied at the same time. A large shifting range requires high electric field strength in the modulator where the optical field propagates. This can be accomplished by placing the electrodes close to channel waveguides which confine the optical

field [164]. A drawback of this approach is that the propagation loss increases [165]. The opposite approach is a bulk EOM without waveguides and electrodes more distant to the optical field. A bulk crystal reduces the propagation loss for the optical field greatly. The result of distant electrodes is a lower electric field strength at the optical field such that the shifting range is smaller.

In this experiment the emphasis is on the shifting range. Therefore a fibre coupled EOM with a V_π of 4.5 V and a transmission loss of 2.0 dB implements the frequency shift. The V_π is the Voltage difference required for a π phase shift of the optical field. As we will learn in the next chapter, the 8 GHz RF signal is amplified to a power of 3 W. The linear range of the RF signal modulates the refractive index of the EOM and a frequency shift is imposed on the optical field as discussed in Section 3.2.3. We relate the power P of the RF signal and the amplitude of the phase change on the optical field by

$$A_\phi = \sqrt{2RP}\frac{\pi}{V_\pi}, \tag{4.1}$$

where R is the 50 Ω impedance of the RF signal line. The linear time varying phase is then,

$$\phi(t) = 2\pi f_{\mathrm{RF}} A_\phi t. \tag{4.2}$$

We will therefore expect a frequency shift of up to ±96.7 GHz, following (3.11), equivalent to a wavelength change of ±0.76 nm. The EOM is followed by a fibre integrated bandpass filter, centred at 1535 nm with a FWHM of 50 GHz. This filter selects the transmitted spectral bin for the output of the frequency multiplexed source. The optical loss in the transmission band of this filter is 0.37 dB. In the utilised down-conversion process the bandwidth of the

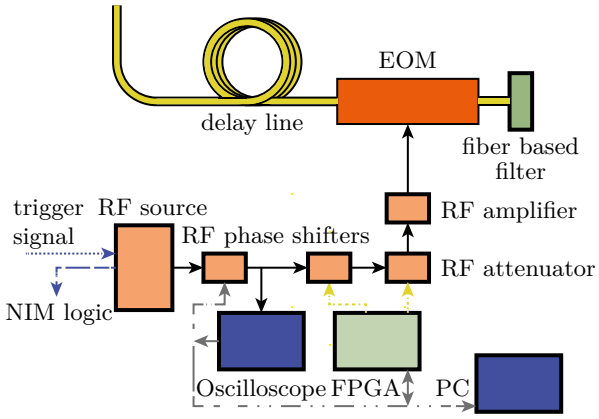

Figure 4.10: The RF synthesizer locks to the external reference signal and generates the 8 GHz signal. A locking loop stabilises the phase of the RF signal and the FPGA controls the feed forward settings.

generated photons is determined by the spectral pump field width. The output filter is not well matched to the pump bandwidth due to the relaxed pump filter requirements. This leads to a reduced transmission through the narrow output filter of the relatively broad heralded photons. This mismatch increases the loss in the signal path.

4.4.2 Radio Frequency field generation

We now turn our attention to synthesising the RF signal, that drives the frequency shift. The elements used to generate and control the RF signal are displayed in Fig. 4.10. A photodiode detects the 10 MHz trigger signal from the laser monitor output and passes it to the reference clock input of a RF synthesizer. The synthesizer locks its internal clock to the external reference and generates a 8 GHz signal.

We can understand the choice for the RF frequency by considering that the slope of the RF signal determines the optical shift, as described in Eq. (4.2). It is therefore desirable to use a high frequency signal with a steep slope. A second consideration is the duration of the optical pulse, which must be within the linear region of the RF signal. The optical pulse will

be distorted if it is longer than this region. Therefore, we have to select a RF signal with as high a frequency as possible to maximise the shifting range, while still accommodating the full duration of the optical pulse in its linear range. Assuming that the linear range is approximately $\frac{1}{4}$ of a period, an 8 GHz signal can shift a pulse of up to 31.25 ps duration without distortion. A transform limited pulse of this length has a spectral intensity FWHM of 14.12 GHz or 0.113 nm at 1550 nm.

Phase locking of the radio frequency signal

A problem in deriving a 8 GHz signal from a 10 MHz reference is that a small phase drift in the 10 MHz signal is a much larger phase drift in a 8 GHz signal. To improve the phase stability of the 8 GHz signal a fast sampling oscilloscope monitors its trace. A computer script corrects for the phase-drift with respect to an initial trace and proportionally changes the setting of a RF phase shifter. This is a slow locking loop that stabilizes phase-drift that occurs on a timescale of several seconds. The amplitude of the RF signal changes depending on the phase shifter setting. A diode is used to monitor the RF power and feeds this back to the RF synthesizer to stabilize the signal amplitude.

Following the phase stabilisation circuit, an additional phase shifter and attenuator, controlled by the FPGA, apply the feed forward settings to the RF signal. Close to the EOM a 3 W RF amplifier intensifies the RF signal to enable large frequency shifts. This amplifier is located as close as possible to the EOM to minimise signal attenuation.

Component name	specified optical loss
EOM	2.0 dB
Signal filter	0.37 dB
FBG	2.33 – 2.89 dB
Detector	∼0.97 dB†
Fibre coupling	1.5 – 3 dB†
Delay line	0.18 dB†

Table 4.5: Summary of the specified optical component loss if available provided by the manufacturer or measured (†)

4.5 Summary

In this chapter we took a detailed look at the experimental set-up, the choices made for the implementation of the frequency multiplexed source and the specifications of the individual components. A summary of the optical component loss is given in Table 4.5. In the next chapter we will characterise and calibrate each component and establish a functional frequency multiplexed source.

Chapter 5

Performance of the frequency multiplexing set-up

With the framework and the general working principle of a frequency multiplexed single photon source and its components in place, it is now time to see how the set-up performs. In the next sections we will present the characterisation of the components of the multiplexed photon source. In a final step we investigate the performance of the full set-up and compare it to the theoretical framework we developed in Chapter 3.4.

5.1 Photon generation

In Chapter 4.1.1 we discussed the pump field preparation. We learned that high stability of the pulse repetition rate is one of the crucial requirements for the laser system. A temperature controlled enclosure houses the cavity of the customized fibre laser to tune the repetition rate to 10 MHz ± 200 Hz. In this enclosure additional aluminium blocks act as

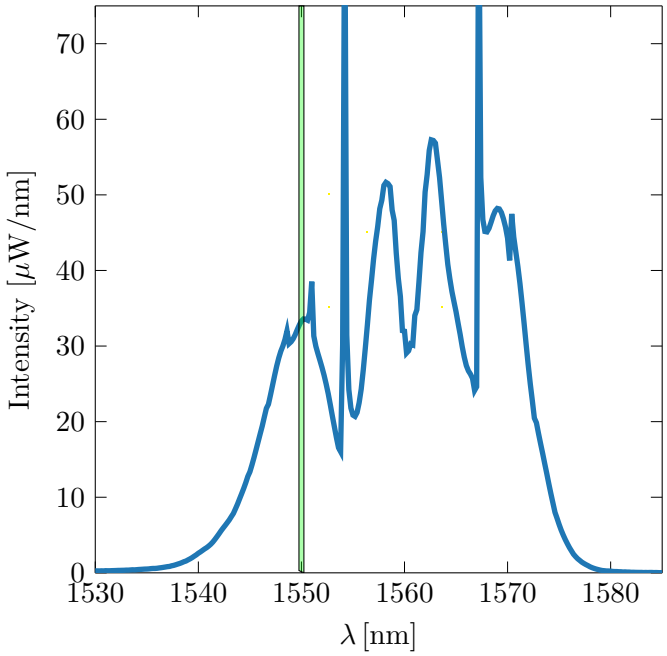

Figure 5.1: The attenuated output spectrum of the customised telecommunication wavelength fibre laser spans a frequency range of $1545 - 1575\,\text{nm}$. A green box indicates the region which is relevant for the final pump field.

heat reservoirs and a Peltier element heats the system to 34°C. This thermally decouples the laser cavity from the temperature fluctuations of the laboratory, such that no additional active stabilisation is required to keep the laser pulse repetition rate within the target range. Table 4.1 of the previous chapter summarises the specifications of the laser system.

Next we will concentrate on the spectral properties of the laser and on shaping the pump field such that it is suitable for the frequency multiplexed source. The aim is to up-convert the telecommunication wavelength laser field with a SHG process to 775 nm, the wavelength at which the pump spectrum should be centred for the PDC process. The power of the pump field needs to be in the range of a few Milliwatt (mW) and have an optimal spectral FWHM bandwidth of 0.05 nm or $\sim 25\,\text{GHz}$ at 775 nm.

The idea is to frequency double the field first and then apply spectral filtering. The laser output, as depicted in Fig. 5.1, is up-converted by SHG in a periodically poled LN crys-

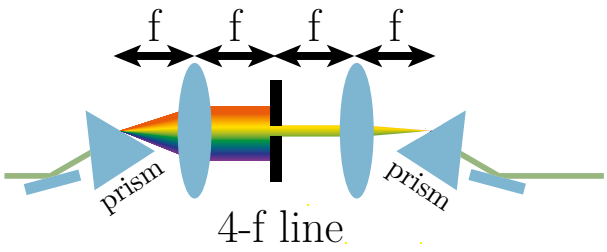

Figure 5.2: Schematic of a 4-f line set-up: The dispersive element maps the frequency components of an optical pulse to different propagation directions. A lens in one focal length distance converts these components in its focal plane to distinct spatial positions. The variable slit selects the transmitted frequency components which are then recombined to a beam with a mirrored arrangement of the lens and dispersive element.

tal. Initially, a 4-f line set-up was used to spectrally filter the up-converted pump field as displayed in Fig. 5.2. It consists of a dispersive element such as a grating or prism that disperses the frequency components of a light field into different propagation directions. A lens, one focal length away from the grating, completes a Fourier transformation and maps, together with the grating, the wave-vector of each frequency component to a position in space at the focal plane. A slit at that position selects the frequency components and a second set of a lens and grating recombine the beam again. This set-up has a length 4 times the focal length of the lenses used and is therefore referred to as a 4-f line.

J Tiedau designed a 4-f line of 4 m length to reach the necessary spectral resolution [163]. The measured minimal filtered pump field bandwidth is $\sim 0.07\,\mathrm{nm}$ [163], limited by the dispersion of the grating and the focal length of the lens. In addition to its large size the 4-f line introduces loss, resulting in a transmission of about 66 % of the pump field. This additional loss reduces the already low pump field power levels to $10 - 20\,\mu\mathrm{W}$. For the operation of the multiplexed photon source these levels were insufficient.

In order to optimize pump power, we instead used an etalon to filter the pump field. Two mirrors with 74 % and 99 % reflectivity separated by 0.25 mm form the etalon. The line

width of this set-up is 0.059 nm with a free spectral range of 1.2 nm. An additional band-pass filter of $\sim$1.3 nm FWHM is sufficient to select a single mode. The transmission of the etalon is $60-70\,\%$, similar to the transmission of the 4-f line in the required spectral range. The pump field power therefore remains too low for the frequency multiplexing source.
If we turn our attention back to the initial laser spectrum, in Fig. 5.1, we can see that the spectral range of interest only forms a very small portion of the full spectrum. In addition this part of the spectrum is not even the one with the highest intensities. To circumvent these limitations and difficulties a different approach was chosen for the final set-up.

Instead of converting the pump field first and then filtering it, the filter is applied first. We also relax the bandwidth requirements from $\sim$ 25 GHz to about 60 GHz, such that compact off the shelf fibre integrated filters can be used. The drawback of increasing the pump bandwidth is that the number of multiplexed modes is reduced. Additionally an amplification stage was inserted, consisting of an EDFA, increasing the power in the spectral bandwidth of interest, as depicted in Fig. 4.4. A coarse spectral filter reduces the optical power propagating in the optical fibre before the inline filter. This prevents self-phase modulation and Raman-induced frequency shifts[166,167] in the optical fibre at high optical power. Figure 5.3 displays the filtered laser spectrum. The spectrum is centred at 1550 nm and has a bandwidth of $\sim$0.34 nm.

An EDFA amplifies the filtered pump spectrum to $50-70$ mW. A second filter removes spectral broadening and background noise arising from amplification and fibre transmission. Figure 5.3 shows the amplified spectrum. A side-peak was observed in the filtered spectra, especially in the amplified one. This side-peak is due to the specific filter design. The

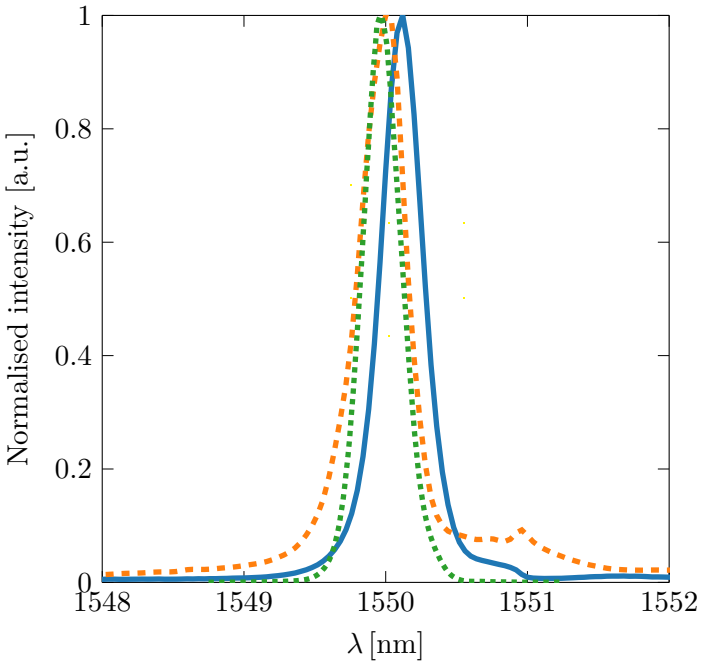

Figure 5.3: Transmission spectra of the pump field after different filter and amplification stages: The pump laser field coupled to the input of the EDFA is first filtered, solid blue line, before the amplification stage. The amplified field passes an identical filter, dashed orange line, to remove spectral broadening, and is then polarisation filtered, dotted green line. A small misalignment between the central filter frequencies leads to the offset between the displayed spectra.

inline filter consists of a packaged Fabry-Perot filter filter, which can be tuned by rotation, between fibre collimation packages. For two orthogonal linear polarisations the central wavelength of the angled filter is slightly offset. Despite the polarisation control of the set-up, amplification adds light in the other mode leading to a rise of the side peak. A set of wave-plates and a Polarising Beam Splitter (PBS) filter the polarisation following the amplification of the pump field.

The SHG stage then frequency doubles the filtered and amplified pump field to a centred wavelength of 775 nm with a bandwidth of 0.12 nm, see Fig. 5.4a. This approach can deliver pump powers of up to 2 mW to the PDC chip for photon generation. A concern that arises is that the pump field is not transform limited but chirped due to the initial pump

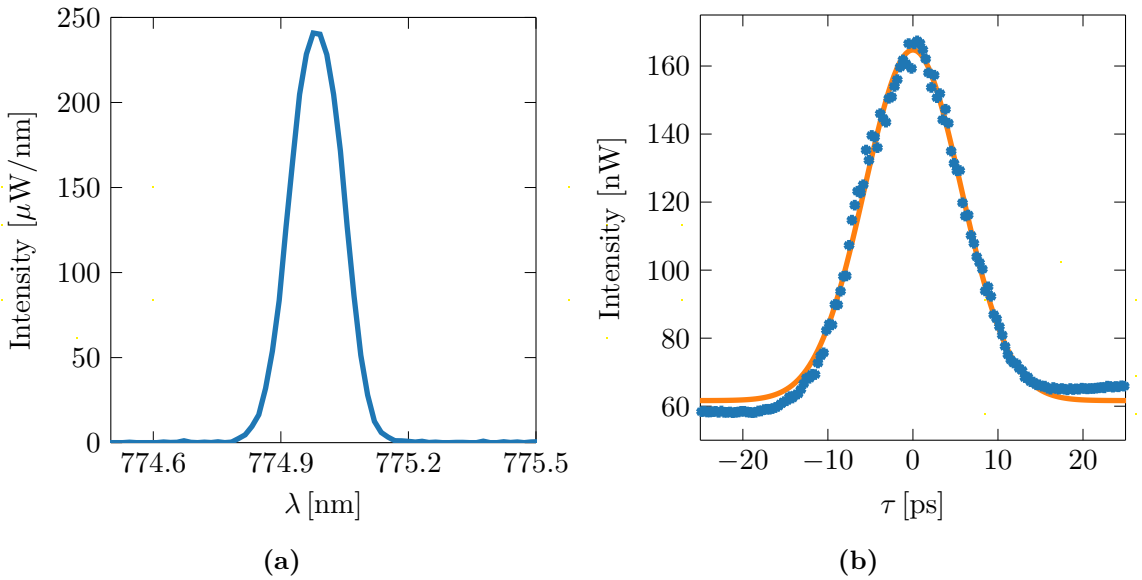

Figure 5.4: (a) SHG converts the filtered and re-amplified fibre laser output to the required pump field wavelength of 775 nm. (b) an autocorrelation measurement, blue data-points, verifies that the pump pulse is near transform limited with 9.45 ps duration. A Gaussian fit, solid orange line, is displayed alongside the measurement.

spectrum and self-phase modulation in the amplification process. This leads to chirped photons emitted by the source. Chirped wave-packets have a longer temporal duration than transform limited ones. For the shifting operation the duration of the photon is critical and has to be within the linear range of the shifting signal. Further, a chirped pump pulse can in principal induce mixedness in the heralded photon state. For the frequency multiplexed source this is not a concern, because the phase profile, depicted as a slice in Fig. 5.5, is identical for the heralded photons, after frequency shifting. The emitted photons remain therefore indistinguishable with identical chirp.

An auto-correlation measurement of the pulse duration was used to verify that the pump is not significantly chirped. Figure 5.4b depicts the resulting auto-correlation function of the pulse-envelope. The pump duration is nearly transform limited with 9.45 ps versus the expected 7.36 ps.

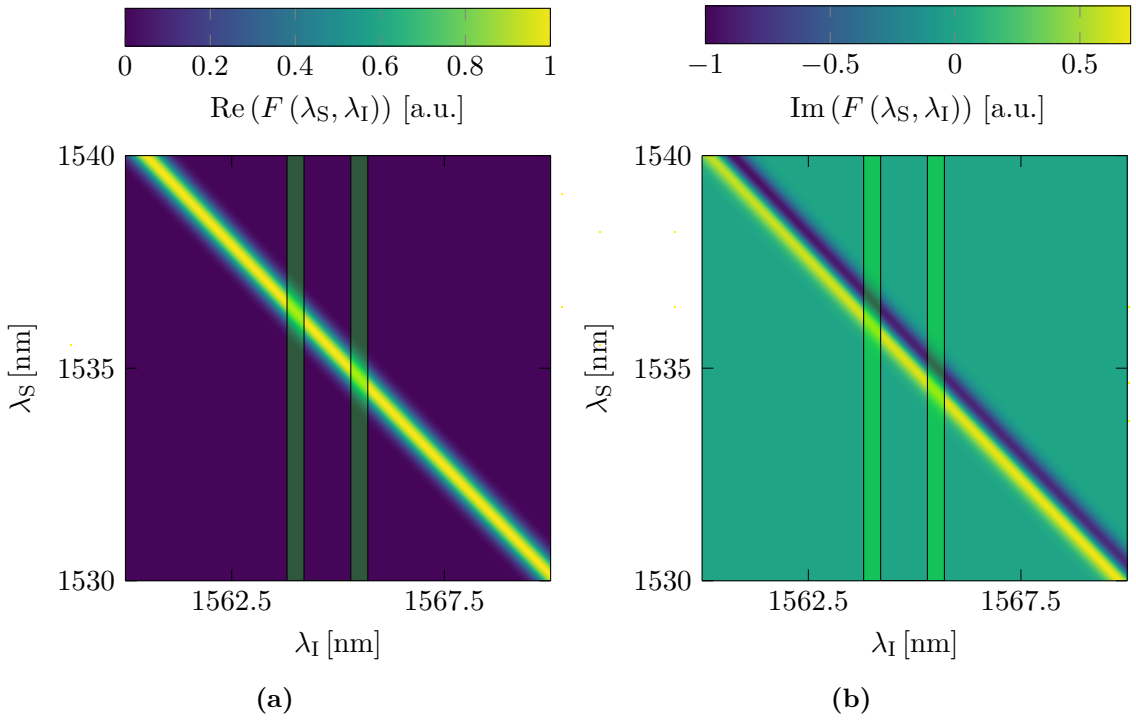

Figure 5.5: The real (a) and imaginary (b) part of the JSA to a type-0 PDC process. The phase visible in the imaginary part is the same for photons heralded at different frequencies, indicated by the slices.

The non-linear optical material enabling the type-0 SPDC process is KTP and the polarisation of the optical fields are orientated along the z-axis of the crystal. The chip length was initially chosen as 3.29 mm to build a cavity for the heralded mode by adding custom reflective coatings to the chip facets. This idea proved to be technically challenging for the chip manufacturer and its implementation has been postponed. Nevertheless the chip was used even with its broad phase-matching function. However the short chip length makes it difficult to distinguish between a mode coupled to a waveguide and light that propagates through the bulk material. By using lenses with short focal length, it becomes easier to distinguish between these two effects, due to a stronger divergence of the beam. For this reason, a lens with shorter focal length than for optimal mode matching was used

to couple the pump light into the waveguide. The coupling efficiencies of the output mode of the waveguide and single mode optical fibres are $\sim 50\,\%$ for the herald field and $\sim 70\,\%$ for the signal field. Temperature variations of the laboratory and relaxation of the optical mounts require daily optimization of the fibre coupling to maximize the coupling efficiency. Different path lengths between the chip to the herald and signal fibre as well as the distinct spectral ranges around 1535 nm and 1565 nm lead to the disparate coupling efficiencies.

We learned earlier that the type-0 SPDC process is phase-matched for a wide frequency range and is degenerate at 1550 nm. An angled edge pass filter was used to separate the signal and idler fields. The filter transmits the signal field below ~ 1549.5 nm and reflects the herald field above ~ 1550.5 nm. In the reflected beam path some scattered light below 1550 nm remains close to the filter edge. Angle tuning of the filter decreases the wavelength position of this filter edge but also diminishes the edge steepness slightly. Light in the region of the filter edge is reflected as well as transmitted and is therefore discarded in the experiment, by additional spectral filters. The ranges of signal and herald fields used in the multiplexed source are centred at 1535 nm and 1565 nm respectively to stay clear of this edge and the scattered light.

The JSI of the SPDC process was recorded by using two TOF spectrometers to accumulate coincidence timing events[152]. The time of arrival converted to wavelength is shown in Fig. 5.6. We clearly observe the spectral correlations that one expected from type-0 SPDC in periodically poled KTP.

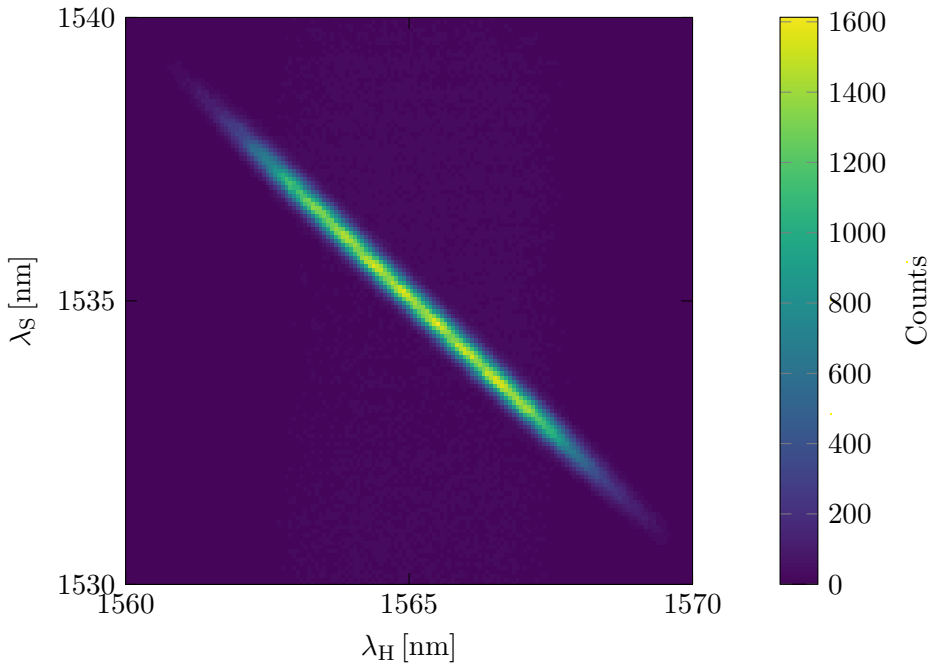

Figure 5.6: The measured JSI of the correlated photon source is limited by the filter applied to the herald mode with a bandwidth of $\sim 6\,\text{nm}$. The frequency correlation has the expected shape anticipated by the numerical simulations.

5.2 The Time of Flight spectrometer

We studied the working principle of the TOF spectrometer in Section 4.2.2 and will now discuss the characterisation of the spectrometer. We use seeded down-conversion to calibrate the TOF spectrometer[168]. The spectrometer is connected to either the signal or the herald mode while the other one is blocked. A strong Continuous-Wave (CW) laser, with a bandwidth of $\sim 400\,\text{kHz}$, propagates with the pump beam through the source chip and is spectrally centred at the herald or signal field wavelength, as depicted in Fig. 5.7. This seed field pre-populates the second mode and causes stimulated emission of the correlated mode by Difference Frequency Generation (DFG). Energy conservation requires that the stimulated emission is centred at $\omega_P - \omega_{seed}$. A calibration curve for various seed field wavelengths relates the arrival time bin in the TOF spectrometer and the wavelength of

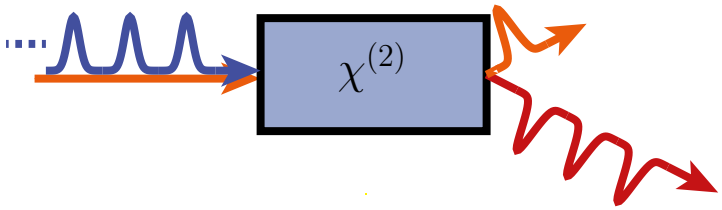

Figure 5.7: Set-up schematic for seeded PDC: A seed laser is coupled through the chip along with the pump field, stimulating the emission of the corresponding opposite field of the PDC process.

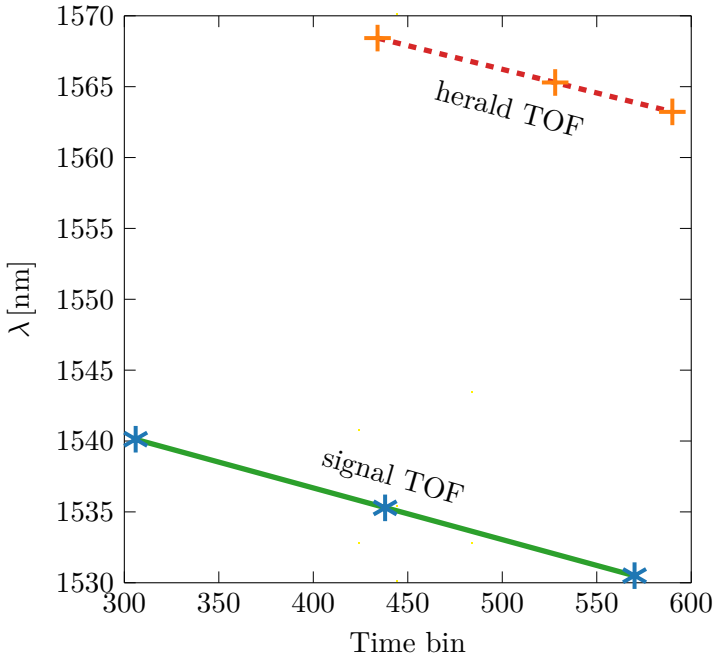

Figure 5.8: The calibration of the TOF spectrometers at three points shows a linear fit to the arrival time bin. Two arrival time bins correspond to 162 ps.

the stimulated field to each other as displayed in Fig. 5.8. A linear fit to the measurement yields the calibration for the two spectrometers summarised in Table 5.1, agreeing with the manufacturer specification. Timing jitter of the time tagger and the detector decrease the resolution of the TOF spectrometer. These are summarised in Table 5.2.

The insertion loss of the Bragg grating in the TOF spectrometer is $\sim 2.89\,\mathrm{dB}$. Losses are mostly due to the circulator separating the incoming light from the light reflected at the grating and the finite reflectivity of the grating itself. The expected spectral resolution of

TOF	a [nm/bin]	b [nm]
herald	−0.0334(5)	1582.9(3)
signal	−0.0365(17)	1551.3(3)

Table 5.1: The calibration curve of the TOF spectrometers is parametrised by $\lambda = a * bin + b$ with the according values listed in the table.

Parameter	Value
SNSPD time jitter	70 ps
Time tagger resolution	162 ps
FPGA TDC resolution	33 ps

Table 5.2: The time resolution of the time tagger and the detectors dictates the resolution of the TOF spectrometer.

the TOF spectrometer measured with the time tagger is on the order of 0.08 nm for two time bins of 162 ps.

5.3 Photon detection

The nanowire detectors behave as expected with a maximal detection efficiency of ∼80 %[169]. This efficiency falls by up to 20 % if the light is in the opposite linear polarisation[160]. High count-rates in excess of $2–3.5{\cdot}10^6$ counts per second lead to an increase in the temporal jitter. This is explained by the fact that the next photon is absorbed before the nanowire has fully cooled down. This leads to a change in the pulse shape of the electronic response of the detector and the threshold determining the event is triggered with a varying timing. To prevent this from impacting measurements, the count-rates are limited to several $100{\cdot}10^3$ counts per second.

A related effect occurs in the TOF spectrometer. The emission of the type-0 SPDC process is very broadband and photons from multi-pair emissions can be in different spectral bins at the same time. The binary detector only registers the first photon in a certain time

window and ignores all others, due to the detector dead time. If the spectral range of the PDC pairs is much larger than the range of interest, photons at longer wavelength blind the detector for photons arriving later. For this reason, additional filters on the herald path remove photons from frequency bins which are far off the desired shifting range. The edges of the coarse filters are at $\sim 1562\,\text{nm}$ and $\sim 1568\,\text{nm}$ reducing the full detection window which ranges from $1525-1575\,\text{nm}$.

5.4 Frequency translation

In this section we will characterise the RF signal generation circuit and the EOM as they are the key components to implement the frequency shift.

5.4.1 Radio Frequency field generation

We learned in Section 4.4.2 that the RF signal is generated by a RF synthesizer locked to the laser pulse train. We discussed that deriving an 8 GHz signal from a 10 MHz pulse train is not necessarily phase stable. For this reason a locking loop is needed to prevent large phase drifts.

A fast sampling oscilloscope, triggered by the laser reference, monitors the RF signal from the synthesiser. The fast sampling oscilloscope samples a periodic signal with respect to the reference trigger. For each sample the relative time offset to the reference changes. Over multiple frames the oscilloscope captures the details of the periodic signal with high temporal resolution. This approach of measuring a trace simplifies the electronic signal processing and reduces the necessary bandwidth of the oscilloscope. A downside is that shot to shot variations in the signal wash out. We confirmed with a high bandwidth oscilloscope

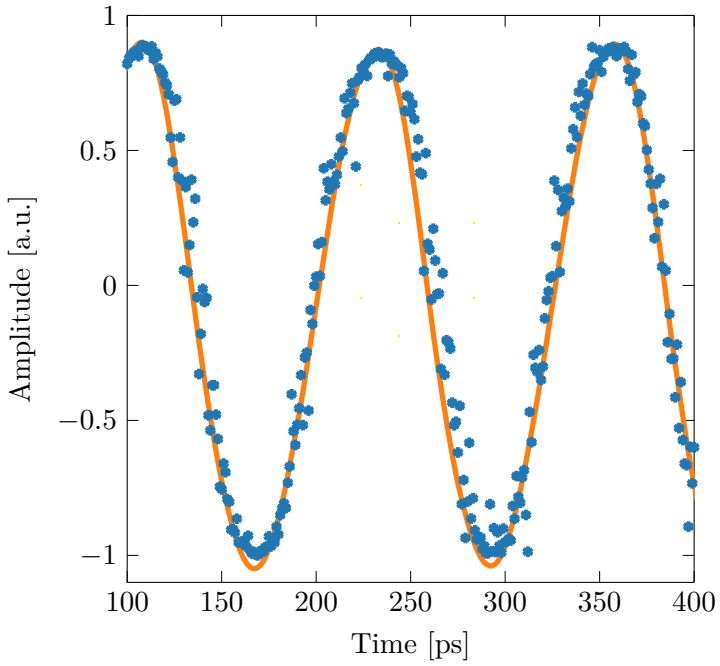

Figure 5.9: The RF signal traces recorded with the fast sampling oscilloscope, blue markers, agree with the trace recorded by a high bandwidth oscilloscope, orange solid line.

that the captured trace is a good representation of the monitored signal, see Fig. 5.9. Approximately once per second a computer processes the acquired trace of the sampling oscilloscope. The program fits a sinusoidal function to the trace and compares it to the initial dataset recorded when the script was started. It evaluates the amplitude and phase difference of these two datasets, as plotted in Fig. 5.10a and 5.10c. If the locking loop is activated a proportional algorithm compensates the phase difference and changes the setting of a RF phase shifter in the RF signal line. It is clear from the figure that the locking loop compensates for phase drift on the order of tens of seconds while fast variations remain. Nevertheless this reduces the phase noise from up to $\pm 10°$ to $\pm 2.5°$. A shift of $20°$ would offset the RF signal significantly with respect to the photon arrival time at the EOM, leading to temporal chirp and spectral broadening of the photon instead of a clean frequency shift. Figure 5.10b displays the voltage applied to the RF shifter. The amplitude of the RF signal,

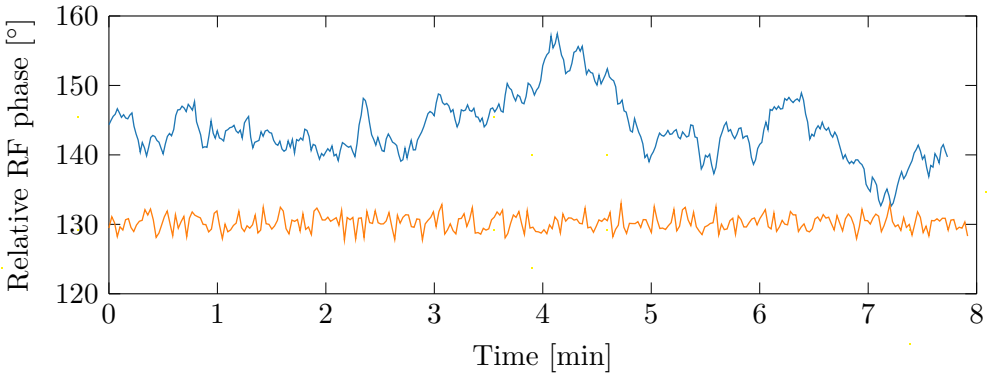

(a)

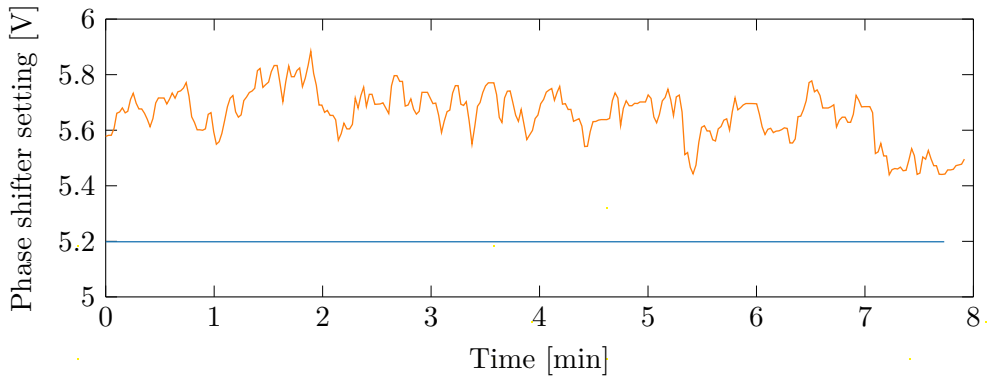

(b)

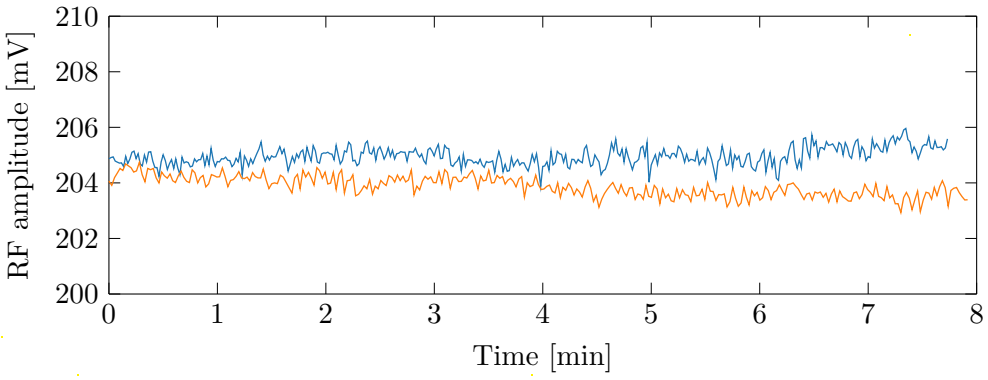

(c)

Figure 5.10: (a) The phase of the unstabilised RF signal drifts over tens of degrees, blue solid lines. A fast sampling oscilloscope periodically acquires a trace of the RF signal and a computer script matches it to a previous measurement. Phase drift is compensated with a variable RF phase shifter, orange lines.(b) The applied voltage to the phase shifter as adapted to compensate phase drift. (c) A diode always monitors the signal amplitude and feeds it back to the RF generator, which stabilises it with an internal circuit. The RF signal amplitude remains therefore nearly constant.

Fig. 5.10c, is monitored by an external Schottky diode detector and fed back to the signal synthesizer, which internally stabilizes the power output.

5.4.2 Electro-Optical Modulator performance

The performance of the EOM was tested with the help of weak coherent pulses generated by DFG. This is the same DFG process that was used when calibrating the TOF spectrometer, enhancing the emission such that it can easily be detected with standard spectrometers. An Optical Spectrum Analyser (OSA) records the emission in the signal field after passing the EOM. This seeded process was used to align the polarisation of the signal field with the axes of the EOM, which only acts on one linear polarisation. In the following step, the RF phase was adjusted to maximize the spectral shift with minimal distortion. Figure 5.11 displays the resulting traces. The central peak corresponds to the unshifted seeded down-conversion process centred at 1535.0 nm with a spectral bandwidth of 0.396 nm. Located to the left and the right are the maximally up and down shifted spectra centred at 1534.35 nm and 1535.58 nm with a bandwidth of 0.388 nm and 0.408 nm respectively. No notable distortion in the shape of the spectra occurs. A small change of the spectral bandwidth leads to the amplitude variation of the spectrum on the right hand side. In Section 4.4.1 we concluded, that for the RF power available, we expect a frequency shift of up to ± 0.76 nm. The measurement shows that the shifting is limited to ± 0.65 nm slightly less than expected. This is due to additional loss on the RF signal or a larger V_π.

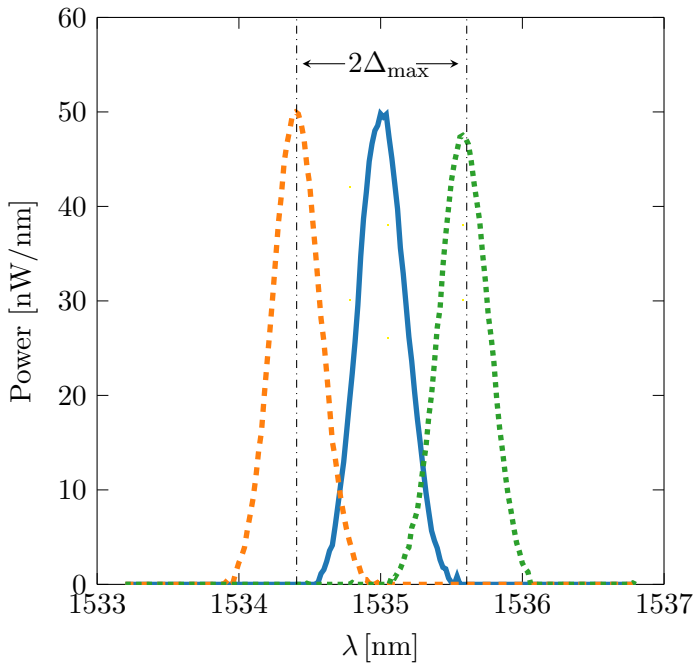

Figure 5.11: The EOM translates the spectra of the seeded PDC process by up to $\Delta_{max} = \pm 0.65\,\text{nm}$. As an example the unshifted and maximally up and down shifted spectra are compared. The spectral distortion remains minimal.

5.5 Feed forward control logic

We use an FPGA to evaluate the herald arrival time an apply the according frequency shift setting to the signal photons. These settings applied in the feed forward step are defined in a second set of LUTs. The LUTs are derived by first finding the phase settings for which the photon propagating through the EOM is synchronised with the linear positive or negative slope of the RF signal, as seen in Fig. 3.8. In a second step, the phase was held constant while the RF signal amplitude is changed such that different shift distances are applied.

For the first step we perform a global phase calibration. Seeded down-conversion aids this measurement again. A spectrometer monitors the spectrum after the EOM while we perform a coarse phase sweep of the RF signal through the full phase shifter range. The coarse scan determines the range of settings for the maximal frequency shifts and a following

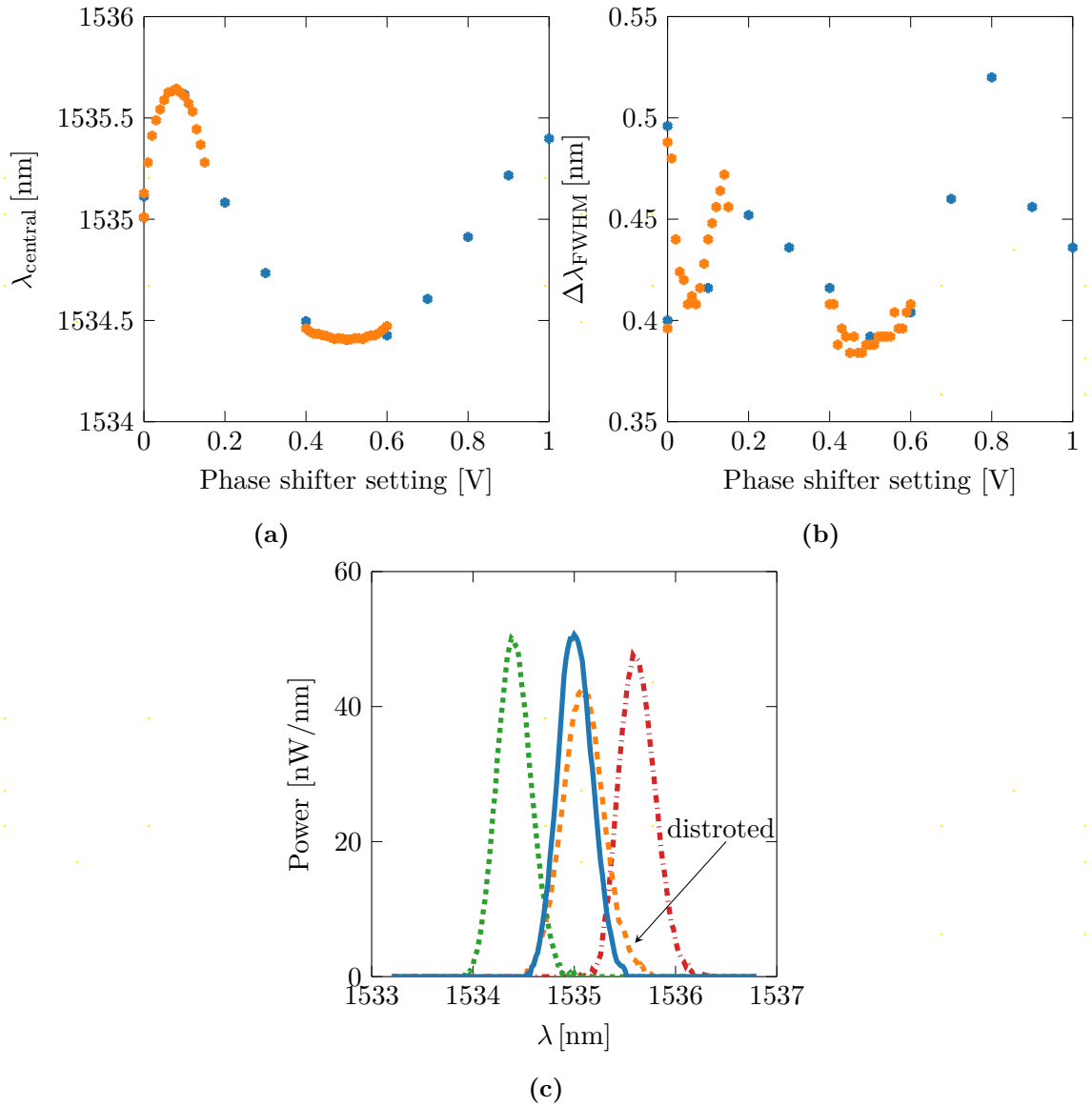

Figure 5.12: The global RF phase calibration scans the phase of the RF signal with respect to the photon arrival time at the EOM. This results in a maximally up and down shifted spectra as well as distorted ones. The central wavelength as well as the spectral bandwidth is recorded, (a) and (b) respectively. A fine scan around the optimal settings, orange data points, identifies the optimal settings. In (c) four exemplary spectra are selected representing no, blue solid, maximal up, red dashed-doted, and down, green dashed, shifts. Alongside a broadened, orange dashed, spectrum is displayed.

fine scan close to these parameters determines the optimal setting. Figure 5.12 displays the settings applied to the phase shifter and the respective central wavelength and spectral bandwidth for these scans. We can see that the central wavelength varies smoothly with

the applied phase shift. The spectral bandwidth increases for phase settings where none or small frequency shifts are applied. These settings of spectral broadening correspond to pulses coinciding with the maximum and minimum of the RF signal. Figure 5.12c displays example traces of the measured spectra in comparison to an unshifted spectrum. From this particular measurement we have found that the optimal global phase settings for spectral translations are $\sim 0.1\,\mathrm{V}$ for upward and $\sim 0.5\,\mathrm{V}$ for downward shifting.

In Fig. 5.12a we note that the phase shifter response is not linear with respect to the applied voltage and the sinusoidal curve is compressed on one side. For this reason we need to investigate the phase shifter and attenuator response independently.

The fast sampling oscilloscope was used to monitor the RF signal while we scan either the voltage applied to the attenuator or the phase shifter. The plots in Fig. 5.13 show the measured phase changes and amplitude variations of the RF signal. During the characterisation of the phase shifter no attenuation is applied and no additional phase shift is used when characterising the attenuator. We can see that the phase shifter, as well as the attenuator, do not only change either the phase or the amplitude of the RF signal, but also impact the other parameter. We also find a slight non-linear response of the phase shifter for settings in the range of $\sim 0 - 0.2\,\mathrm{V}$. The plots clearly show that the LUTs need to take into account the large amplitude change of $> 10\,\%$ for the phase shifter and steep jump in phase for the attenuator.

The distance of the spectral shift is directly proportional to the RF signal amplitude as we have seen in Section 3.2.3. If the amplitude is halved the shift is halved as well. From the global phase calibration we know the maximal up and down shift as well as the phase setting required for those shifts. We combine this information in a model which also takes

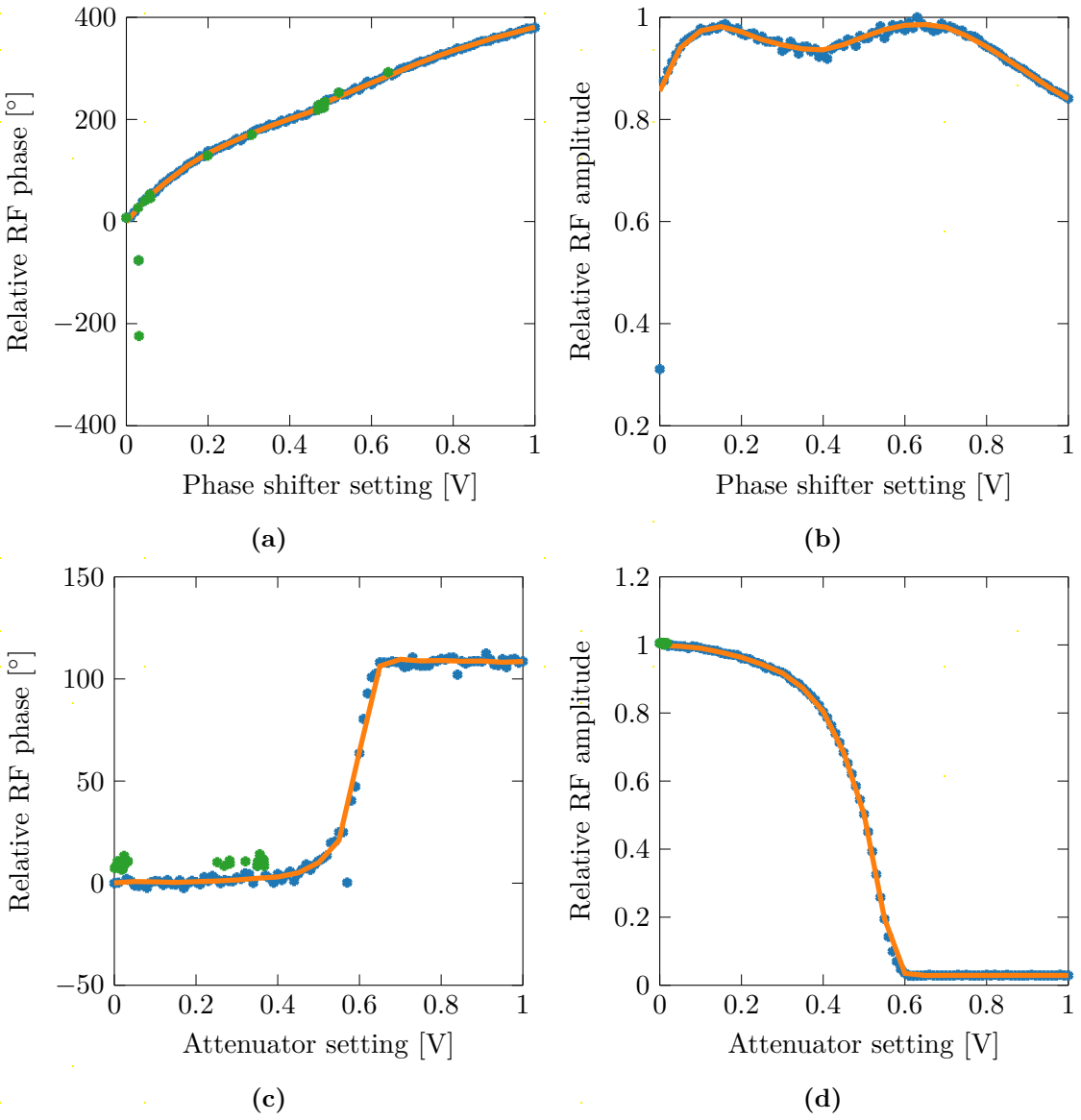

Figure 5.13: The RF phase shifter applies a voltage dependent phase shift and attenuation to the RF signal, (a) and (b). Similarly, the RF attenuator also changes the phase and amplitude of the signal, (c) and (d). Both devices are characterised with the measurements, blue dots, and a function is fitted to the data points, orange line. Measurements excluded from the fit are marked in green.

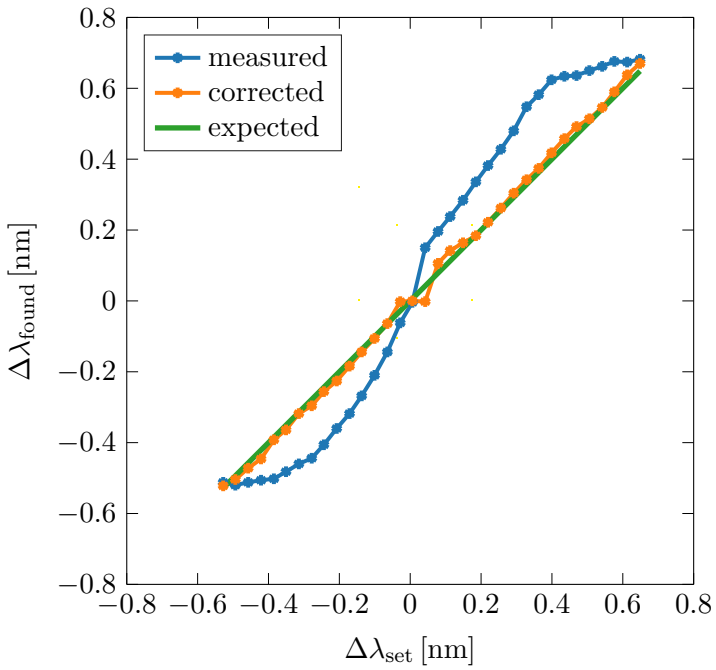

Figure 5.14: The LUT settings to implement frequency shift are tested with seeded PDC. The measured shift, blue line and points, varies significantly from the expected translation, green line. A final adjustment to the LUT corrects for these offsets, orange line and points.

the attenuator and phase shifter calibration into account. The result is a parameter set which changes the frequency translation linearly while no spectral distortion should occur. We again test this parameter set by taking traces of shifted seeded down-conversion spectra. Figure 5.14 displays the expected shift versus the measured shift of the central wavelength of the spectrum. We note an offset to the expected shifting, which we compensate for in a final adjustment of the applied settings.

At the end of this calibration process a computer program generates the LUT settings and uploads it to the FPGA. Figure 5.15 displays the resulting LUTs, where the time resolution of the LUT is 4.88 ps per bin. The complete LUT has 2^{15} bins and holds many repetitions of the displayed settings, spanning a time window of 160 ns or 66−72 nm accordingly. If time delays larger than 160 ns occur settings corresponding to mod (*delay*, 160 ns)

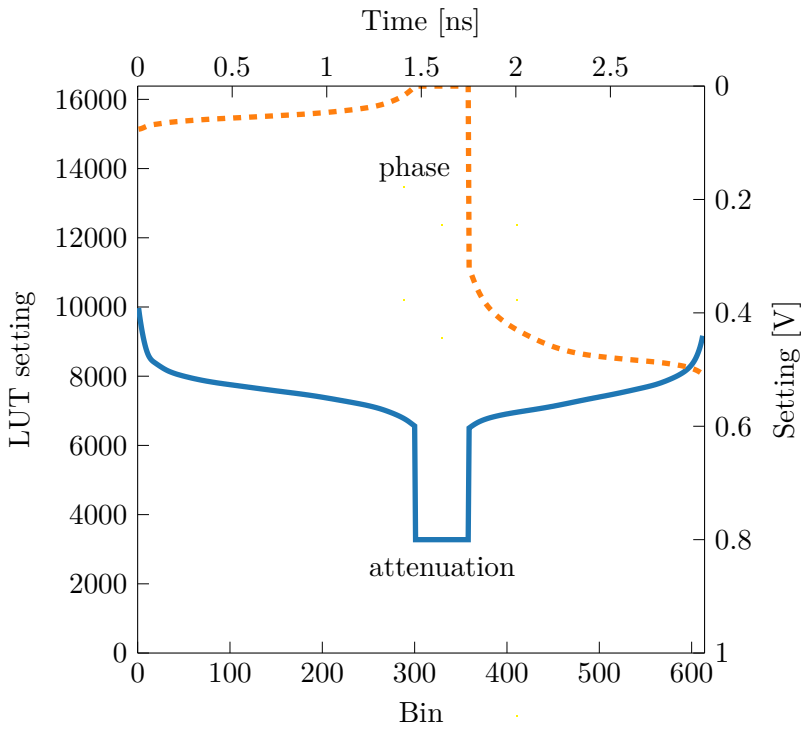

Figure 5.15: The settings of the LUT are within the range of $0 - 2^{14}$, where 16384 represents the minimal applied voltage and 0 the maximal applied voltage to the RF phase shifter and attenuator. For the central bins no frequency shift is applied. This single iteration of settings is repeated several times to fill the whole LUT.

are used.

Next we characterise the performance of the FPGA. Firstly we are interested in determining the latency of the FPGA to a herald event. A delay generator simulates the reference clock as well as the herald events sent to the two input ports of the FPGA and a simplified LUT applies one of two possible settings to the output. An oscilloscope monitors the output voltage and compares it to the timing of a herald signal. This measurement yields an average FPGA latency of 518 ns.

In the next step, we measured the combined set-up timing jitter for all components from the laser system to the FPGA TDC. This timing jitter is the arrival time uncertainty for each

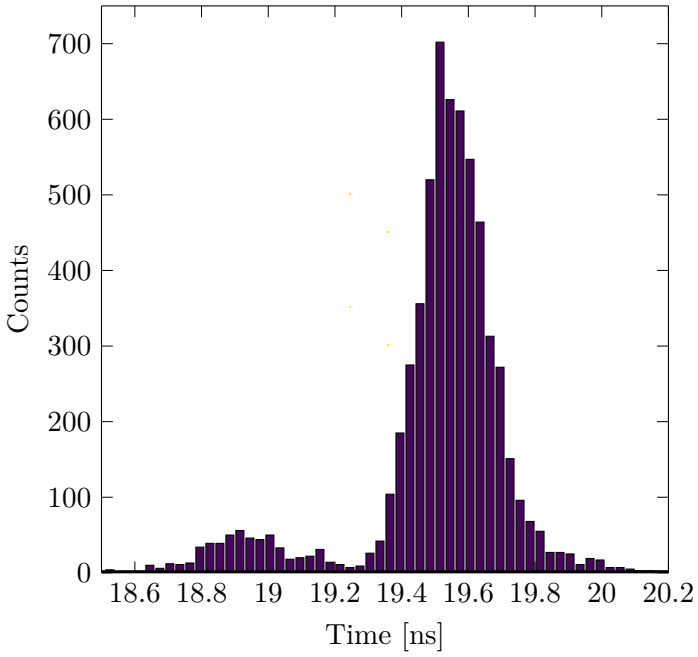

Figure 5.16: A photon arrival time histogram measured by the FPGA TDC for seeded down-conversion without the TOF spectrometer. A small secondary peak at earlier arrival times is present.

Parameter	Value
TDC time resolution	$\sim 33\,\mathrm{ps}$
Combined system time jitter	$234\,\mathrm{ps}$
Feed forward latency	$518\,\mathrm{ns}$
Variation of feed forward latency	-31 to $8\,\mathrm{ns}$
Feed forward signal transient response	$8\,\mathrm{ns}$
Maximal count-rate	$< 2 - 3.5{\cdot}10^{6}\,\mathrm{counts{\cdot}s^{-1}}$

Table 5.3: The summary of the FPGA characteristics takes only the primary peak of the histogram into account.

herald signal when feed forward control is used. We record with the FPGA a time difference histogram of the trigger signal derived from the laser and the converted SNSPD signal, Fig. 5.16. Seeded down-conversion was used to stimulate the emission at one frequency and ensured a fixed timing for all events. The FWHM of the main peak in this measurement is 234 ps. Table 5.3 summarises the performance of the FPGA. The performance of the FPGA is dependent on the quality of the electric signal. The FPGA requires uniform pulses

with a constant duration for the trigger and herald signals. A side peak present in Fig. 5.16 is likely to be caused by jitter in the pulse shape, timing and duration of the electronic signals. The FPGA is sensitive to the rising and falling slopes of the electrical signals which requires standardised pulses with equal duration for the trigger and the herald signals. This constraint is satisfied at the same time as the signal level adaptation of the NIM grid components discussed in Section 4.3. Despite the effort of standardising all electrical signal pulses, slight variations in the pulse shape occur. The FPGA uses a threshold to differentiate a logical low from a logical high signal, which translates pulse shape variations to timing offsets. Repeating changes in the pulse shape are a likely cause for the distinct secondary peak in the event timing of the FPGA.

5.6 Performance of the frequency multiplexed source

In this section we will study the combined performance of the complete frequency multiplexed single photon source. Initially, we will observe in an intuitive way that the feed forward control and frequency translation works as intended. This will be followed by a detailed study of the photon number statistics and characterisation of the heralded photon state purity.

5.6.1 Spectral control

The full assembly of the frequency multiplexed source includes a spectral filter on the output signal arm. With this filter in place we examine again the joint spectral emission of the frequency correlated source. Instead of only one measurement we consider now two joint spectral distributions. The first is the one between the herald and the drop port of the signal

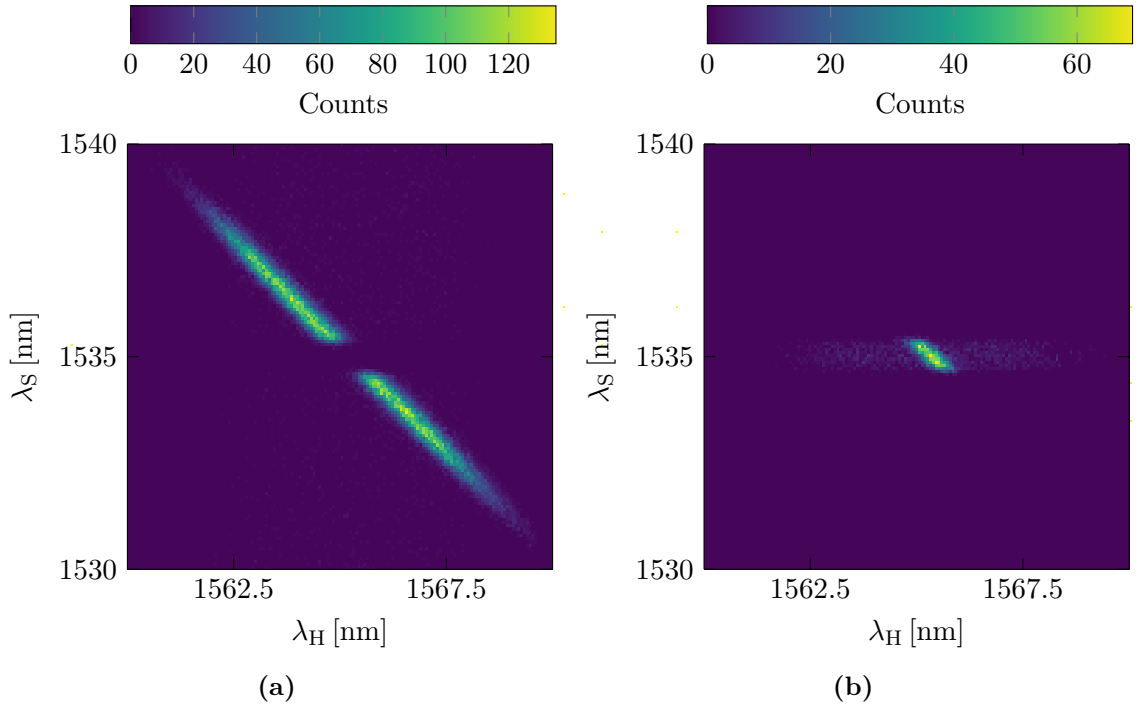

Figure 5.17: The output filter in the signal path separates the output spectral bin from the rejected bins. A measure of the resulting frequency resolved coincidence detections is displayed in (a) for the drop port of the filter and (b) for the pass band.

filter, Fig. 5.17a, as well as the second distribution between the herald and the passband of the filter, Fig. 5.17b. As one expects the signal filter selects a small section of the JSI. This configuration is used for measurements in which the behaviour of a single mode source without multiplexing is approximated.

The FPGA implements the conditional frequency translations for each detected herald photon after calibration of the feed forward electronics and writing the LUTs. Figure 5.18 displays the resulting effective joint spectra. The spectral shift of photons to the passband of the filter effectively shears a section of the JSI to a horizontal line. In this step feed forward control erases spectral information from the initial correlations between the signal and herald fields. The output filter rejects photons which are not within the pass range.

Nevertheless the FPGA implements the frequency translation on all heralded photons.

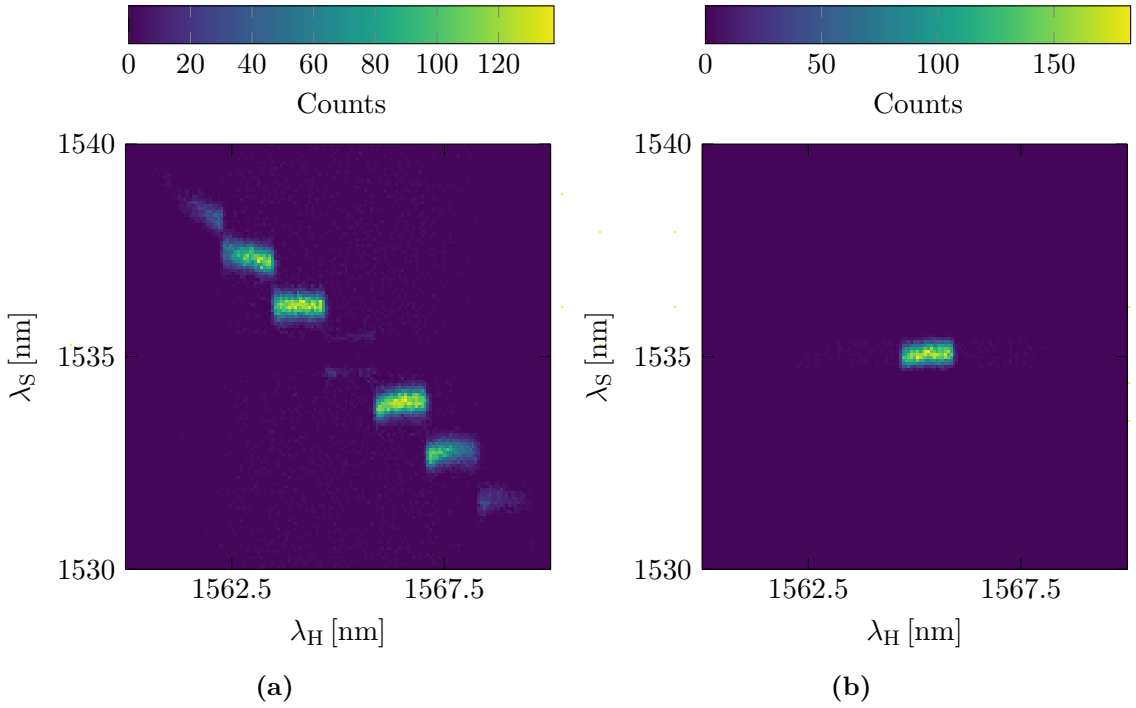

Figure 5.18: With feed forward control, the heralded photons are translated to a common frequency bin, visible as a horizontal feature in the effective JSI. The limited shifting range and multiple repetitions of the identical settings in the LUT lead to several rejected iterations of shifted frequency bins (a) and one that passes the output filter (b).

Multiple repetitions of the shifting entries in the LUT ensure that adjacent modes are equally shifted into a horizontal structure. We observe that not all of these horizontal sections are fully decorrelated and some show remaining distortions. These arise from phase offsets with respect to the RF signal and can be removed by further calibration. With these spectral measurements we have observed that the frequency multiplexing process is working and has been implemented for a frequency correlated single photon source with continuous frequency resolved herald measurements and according signal photon frequency translations. It is now important to determine if the set-up fulfils the requirements imposed on a single photon source and if it performs as well or better than a non-multiplexed one.

5.6.2 Coincidence counting and Klyshko efficiencies

The results presented in the previous section affirm that frequency multiplexing is carried out as intended and that the frequency information is erased by feed forward control. Now we will investigate how this changes the photon statistics and if it agrees with our expectations. Crucially we will also investigate the purity of the emitted photon state. In a following step we discuss how the frequency multiplexed source performs in comparison to a non-multiplexed one.

We expect that the photon flux of the source increases if the emission of multiple modes is combined by feed forward control. This is the fundamental difference from a single mode source where stronger squeezing only increases the brightness and raises at the same time the pollution by higher photon pairs. The following measurements compare the emission of the presented source in two scenarios. In one case no feed forward control is applied, describing an approximation of a single mode source with slightly higher losses, due to tight spectral filtering. The spectral bandwidth of the herald photons is in this case limited to the same bandwidth as the output filter, depicted in Fig. 5.19a. The second scenario represents the multiplexed source with applied feed forward control. Here the spectral herald window spans the full shifting range, as in Fig. 5.19b.

First we observe the change in the herald detection probability as a measure of the source photon flux. Figure 5.20 displays the herald detection probability versus the pump power for the cases displayed in Fig. 5.19. In this measurement the TOF spectrometer acts as a spectral filter by imposing an arrival time window. In the measurements where the source is set-up to mimic that of a nearly single mode source, the feed forward control is disabled and the TOF spectrometer filters the herald mode to a bandwidth of 50 GHz,

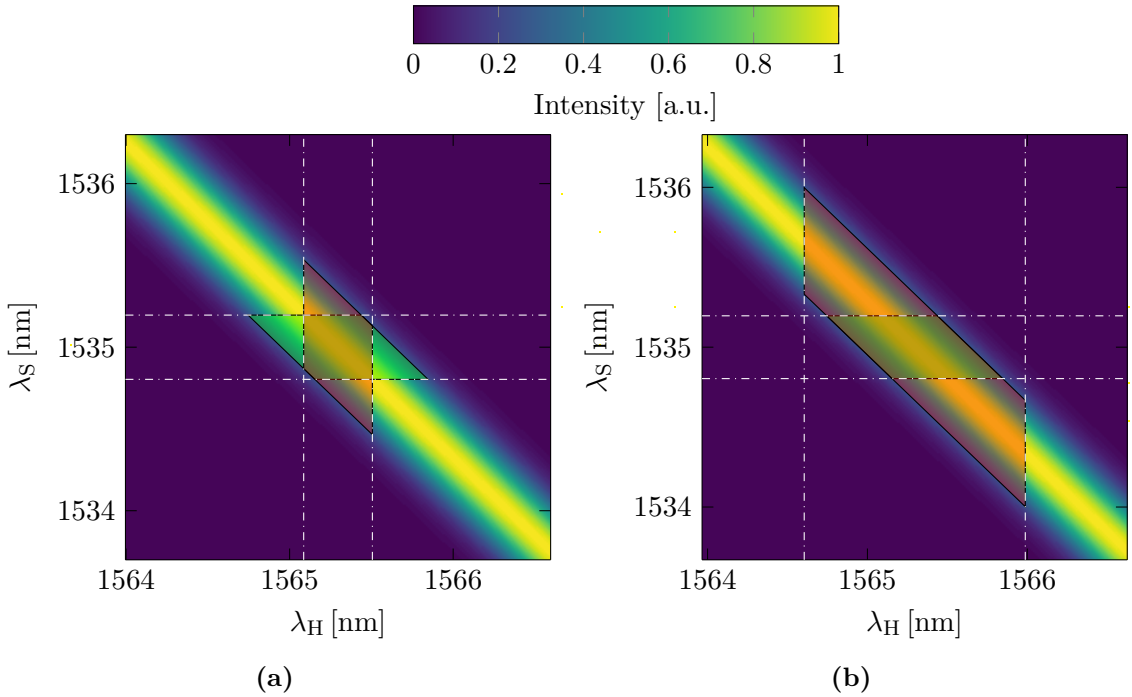

Figure 5.19: Dependent on the measurement, different filter ranges for the post-selected herald detection events are set. For the case, where the emission of a single source is approximated and no feed forward control is used, a narrow herald window corresponding to the same bandwidth as the source output filter is selected (a). The herald detection window is increased to the shifting range if feed forward control is active and frequency bins are multiplexed (b).

similar to the signal filter width. For the second scenario, the herald bandwidth is increased to the full shifting range of 165.4 GHz. Enlarging the herald filter bandwidth increases the herald detection probability. P_H is independent of events in the signal path and is therefore not effected by feed forward control. In all cases we can observe the usual trend that the detection probability increases with higher pump power.

The emission of all non-linear single photon sources is conditional on the herald detection event. A single photon emitted by a SPDC source can only be used if a herald photon was detected and the emitted signal photon is not lost. It is therefore important for us to measure the coincidence detection probability between herald and signal photons. Figure 5.21 displays this measurement versus the pump power for the two filter settings. Again

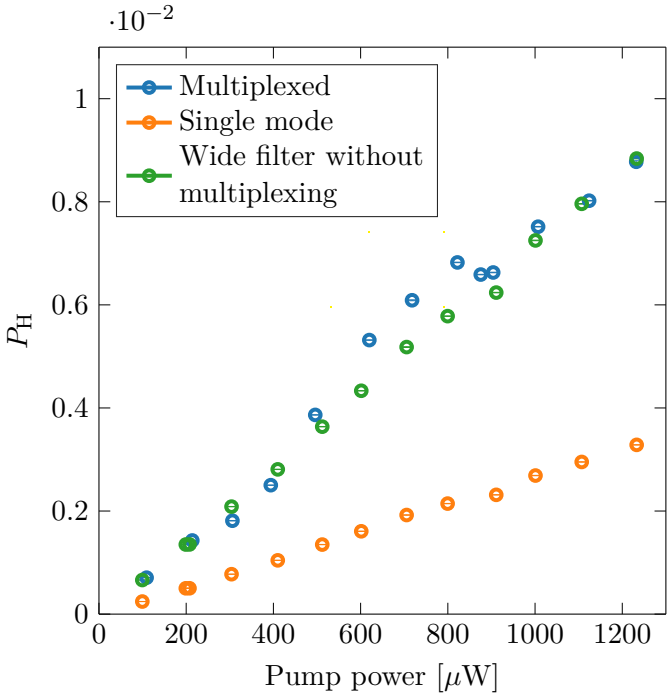

Figure 5.20: The herald detection probability P_H per pump pulse increases with respect to the pump power when comparing a quasi single mode source, lower orange dataset, to the multiplexed source, top blue dataset. The herald detection probability is only dependent on the post selected herald window. Increasing the herald window without multiplexing has therefore the same effect as the green data points indicate.

we can clearly see that the coincidence detection probability is increased by a factor of two for the multiplexed photon source with respect to the quasi single mode scenario. This is due to the fact that the emission of a larger spectral range is accessed and conditionally combined into the source output. The coincidence detection probability also increases for a larger herald filter range without multiplexing because of additional coincidence counts. In Fig. 5.23, we note that the area corresponding to coincidence counts increases significantly if the filter window is enlarged. Feed forward control improves beyond this increase, while erasing the frequency correlation. As expected, the coincidence detection probability increases for the scenarios linearly with larger pump powers. Alongside the measured data-points a theoretical model, see Section 3.4, predicts the expected behaviour

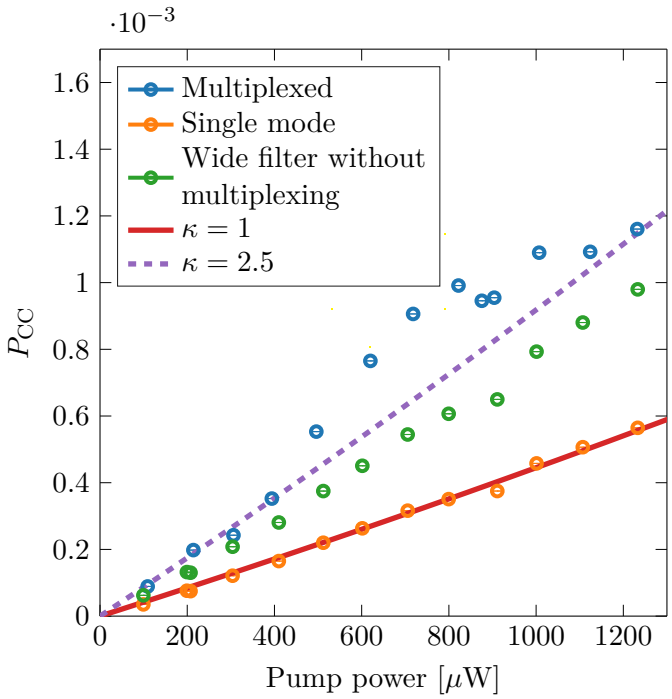

Figure 5.21: The measured coincidence probability increases with respect to the pump power for a quasi single mode source, orange, as well as in the case where frequency bins are multiplexed, blue data points. Enlarging the spectral herald detection window without using feed forward control increases the coincidence detection. P_{CC} is higher for multiplexed frequency bins and constant pump power. Alongside the measurement simulations according to $\kappa = 1$, solid red line, and $\kappa = 2.5$, dashed red purple line, separable modes are displayed.

for a single mode $K = 1$ and multiple separable modes $K = 2.5$ of equal squeezing strength. In this case the effective mode number K and the number of modes used for the simulation κ are equivalent. The deviations of the data points for the multiplexed case from the expected linear slope can be attributed to drifts in the experiment such as changing coupling efficiencies, variations in the feed forward performance due to phase drift and pump power fluctuations.

We can also use the coincidence detection probability to gain further insight into the

performance of the source. In general we denote the coincidence detection probability as,

$$P_{\mathrm{CC}} = \eta_{\mathrm{H}}\,\eta_{\mathrm{S}}\,(1 - P\,(n = 0))\,, \tag{5.1}$$

the product of the signal and herald Klyshko-efficiencies multiplied by the probability of generating photons[170]. The ratios between the coincidence detection probability and the herald or signal detection probability yields the Klyshko-efficiencies of the signal and herald path respectively,

$$\eta_{\mathrm{S}} = \frac{P_{CC}}{\eta_{\mathrm{H}}\,(1 - P\,(n = 0))} = \frac{P_{\mathrm{CC}}}{P_{\mathrm{H}}}, \tag{5.2}$$

$$\eta_{\mathrm{H}} = \frac{P_{\mathrm{CC}}}{P_{\mathrm{S}}}. \tag{5.3}$$

At low pump powers the Klyshko-efficiency approaches the signal and idler path efficiency, because higher photon emissions stop contributing, neglecting the effect of dark counts[104]. The investigation of the path efficiencies is hampered for the frequency multiplexed source by the spectral correlations and different signal and herald filters. We therefore analyse three scenarios to find bounds to the efficiencies. Figure 5.22 displays the values of the herald and signal path Klyshko-efficiencies for increasing pump powers and the different experimental settings. When interpreting these datasets we have to be careful and take the spectral properties of the particular implementation into account. As we see in Fig. 5.23 the spectral ranges of the JSI which corresponds to the coincidence detection events as well as the areas of the herald and signal events do not necessarily fully overlap. For the case of no multiplexing, detection events outside of the overlapping coincidence range will always contribute to the single count events. This leads to an overestimation of the detection

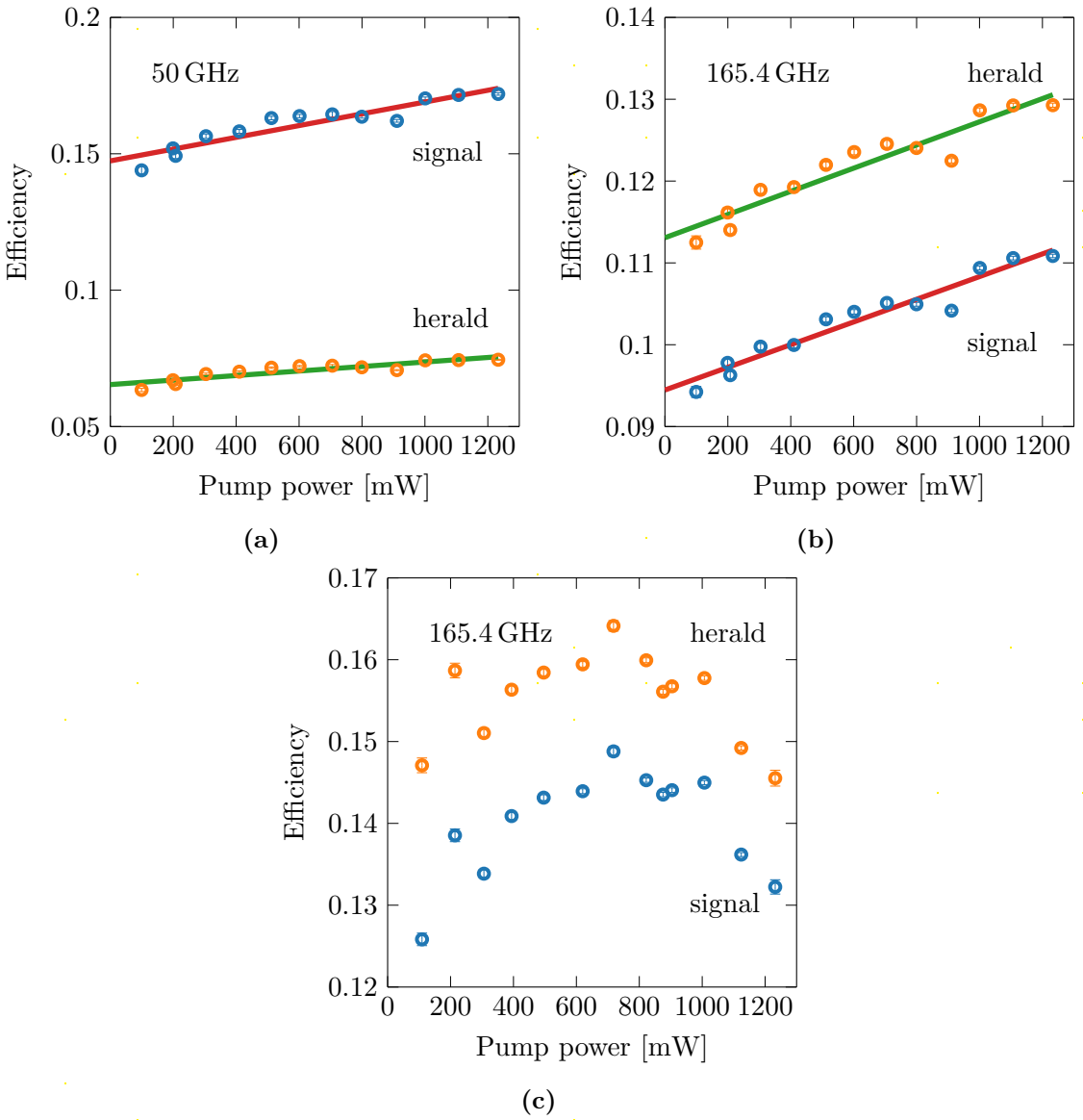

Figure 5.22: The blue data-points reflect the Klyshko-efficiency for the signal path and the orange for the herald path as inferred from the photon count statistics. The dataset displayed in (a) and (b) are measured without feed forward, where (c) uses feed forward control. The post-selected spectral filter width for the herald detection events is 50 GHz in (a) and 165.4 GHz in (b) and (c). Lines indicate linear fits to the data to extract the path efficiency.

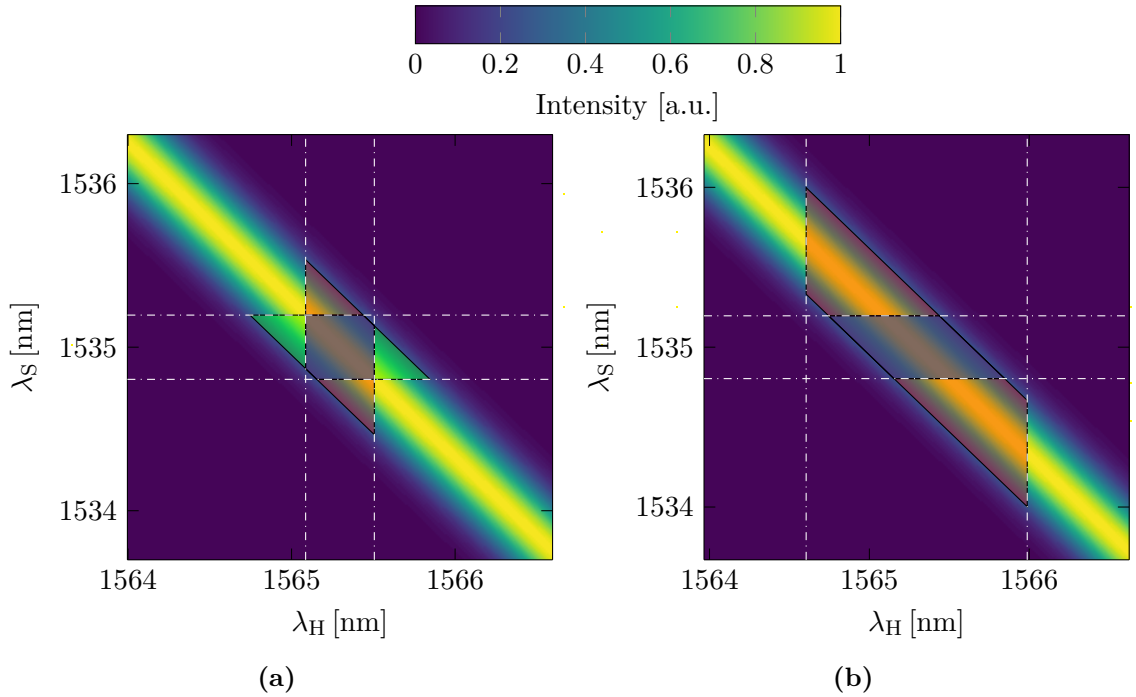

Figure 5.23: For the case of an approximate single mode source, spectral regions of the JSI are included which do not contribute to the coincidence counts (a). Coincidences can only stem from the rectangular region in the centre where both filter-ranges overlap. In (b) the selected spectral range for the herald photons is increased to the shifting range. This in turn increases the coincidence detection range, which now overlaps well with the signal filter range. With such a filter configuration the herald path efficiencies can be inferred. The same configuration is used when feed forward control is active and frequency multiplexing is employed. Heralded photon emission is shifted to within the filter range and the single as well as coincidence detection windows overlap.

probability in one path, in turn underestimating the efficiency of the other. This approach estimates the path efficiencies incorrectly for the filter setting chosen in Fig. 5.23a as used for the measurement in Fig. 5.22a, where no feed forward control is exerted. Nevertheless this is the setting which best approximates a single mode photon source.

Next, we adapt the herald filter such that the overlap between the coincidence detection area and the single signal event region is increased. Figure 5.23b displays this scenario. With this adapted larger herald filter the herald path efficiency is estimated while the measure of the signal path efficiency remains incorrect, see Fig. 5.22b. Linear fits to the datasets without feed forward control were used to estimate the signal and herald path efficiency.

Measurement	η_S	η_H
Combined component loss	$\sim$15.1 %	$\sim$13.8 %
Average efficiency of count statistics with feed forward	14.01(1) %	15.54(1) %
Fit to count statistics quasi single mode source	14.7(2) %†	6.5(1) %†
Fit to count statistics without feed forward, large filter	9.4(1) %†	11.3(1) %
Simulation with $K = 1$	11 %	11 %
Simulation with $K = 2.5$	10 %	10 %

Table 5.4: The summary of estimations to the signal and herald path efficiency inferred from the individual component losses, count statistics and simulations. The simulations reflect an idealised model assuming $\kappa = K$ separable modes with balanced loss and equal squeezing strength. († indicates faulty estimations due to unsuitable filter settings.)

The signal filter is a fixed inline filter and does not allow the bandwidth to be changed. It is therefore not possible to adapt the measurement with all components in place as done before to estimate the signal path efficiency in a similar manner.

The same filter configuration, with a herald filter spanning the full shifting range, provides the settings to measure the path efficiencies with feed forward control. Now all heralded photons should be shifted to the signal filter pass band. Table 5.4 compares the measured signal and herald path efficiencies to the ones inferred by the individual component loss. The values agree well. In particular, the count statistics and the simulations match up for the herald path when the large filter bandwidth is used. We have already discussed why inferring the loss in the signal path from these count statistics is difficult. Nevertheless we see good agreement between the average efficiency of the signal path with feed forward control and the combined component loss. It is also important to remember that the simulations assume κ separable modes with constant loss and equal squeezing strength, reflecting an idealised scenario for the multiplexed source, as depicted in Fig. 5.24.

In order to carry out spectral multiplexing additional elements compared to a common

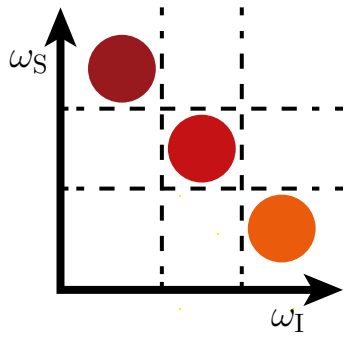

Figure 5.24: Simulations of the photon number statistics assume an idealised scenario of independent separable frequency modes.

Component	Optical loss
Delay line	0.18 dB
EOM	2.2 dB
Signal filter insertion loss	0.46 dB
Signal filter bandwidth mismatch	2.899 dB
Signal fibre coupling	1.5 dB
Total signal loss	7.24 dB
Bragg grating of herald TOF spectrometer	4.6 dB
Herald fibre coupling	3 dB
Total herald loss	7.6 dB
Detection efficiency [169]	$\sim$0.97 dB = 80 %

Table 5.5: Summary of the measured component loss: The output filter of the signal pass is narrower than the photon bandwidth. This artificially decreases the transmission efficiency by an extra 51.3 %. The transmission of the TOF spectrometer is a lower limit, since a broad band light source was used for the measurement, extending beyond the reflection range of the Bragg grating.

heralded single photon source are required. If we now compare these two types of source design, we have to assess if the advantage gained in the photon emission probability by multiplexing compensates for the losses introduced by the extra components needed. The additional components required by the multiplexing scheme are the TOF spectrometer, the EOM, the delay line as well as the output filter. Table 5.5 summarises the losses associated with each component and we discuss now their impact on the source performance.

Once a herald detection event indicates the presence of a photon in the signal path both

source designs rely on the presence of this single photon and any loss can not be compensated for nor registered, corresponding to a reduced heralding efficiencies.

Loss has a similar impact for heralding photons in the single mode source. The herald detector will not provide any insight to the emission of a photon pair if the herald photon is lost. In contrast, in a multiplexed photon source multiple modes can emit herald photons. In this scenario, if one of these herald photons is lost there are still other photons that can be detected and the according signal photon is routed to the common output. We therefore see that a multiplexing scheme can compensate for loss in the herald mode by an increase in the mode number but suffers from the same drawbacks as a single mode source for loss in the signal path. Nevertheless performance of a multiplexed single photon source above the 25 % single source emission probability per pump pulse limit is possible if the losses of the signal path are restricted.

The reduction in the transmission efficiency of the signal path in the presented frequency multiplexed source, due to the EOM, delay line and output filter, is 26.7 %, reducing the total transmission to 15.1 %. This bounds the theoretical limit of heralded photon emission to 15.1 %.

In turn extra modes can counteract the overhead loss of the herald path. We now evaluate what mode number corresponds to the break-even point compensating for the overhead loss of the herald path. For simplicity we assume that in the weak squeezing limit, where higher order photon terms can be neglected, the probability of detecting a herald event is given only by the single photon component such that,

$$P_{\mathrm{H}} = \eta_{\mathrm{H}}\, P\,(n = 1)\,, \tag{5.4}$$

where η_{H} is the herald path efficiency for the non-multiplexed source. The coincidence detection probability is then

$$P_{\mathrm{CC}} = \eta_{\mathrm{S}}\, P_{\mathrm{H}}, \tag{5.5}$$

with η_{S} the signal path efficiency. When adding additional modes κ of equal squeezing strength, the probability of heralding a photon increases by a factor equal to the number of modes, where we neglect the chance of having more than one photon available in all modes, such that

$$P'_{\mathrm{H}} = \kappa\, P_{\mathrm{H}}. \tag{5.6}$$

The alteration of the signal, η'_{S}, and herald, η'_{H}, path efficiencies changes the coincidence detection probability now to

$$P'_{\mathrm{CC}} = \eta_{\mathrm{H}}\eta_{\mathrm{S}}\eta'_{\mathrm{H}}\eta'_{\mathrm{S}}\,\kappa\, P_{\mathrm{H}} = \eta'_{\mathrm{H}}\eta'_{\mathrm{S}}\,\kappa\, P_{\mathrm{CC}}. \tag{5.7}$$

We see that the break-even point is reached, when

$$\frac{P'_{\mathrm{CC}}}{P_{\mathrm{CC}}} \geq 1 \tag{5.8}$$

and

$$\kappa \geq \frac{1}{\eta'_{\mathrm{H}}\eta'_{\mathrm{S}}}. \tag{5.9}$$

For the studied frequency multiplexed source the break-even point is at $\kappa \geq 10.8$ with the losses specified in Table 5.5. A more stringent calculation, also taking herald photons from multiple modes into account, concludes in a break-even mode number of $\kappa = 10.6$ for a

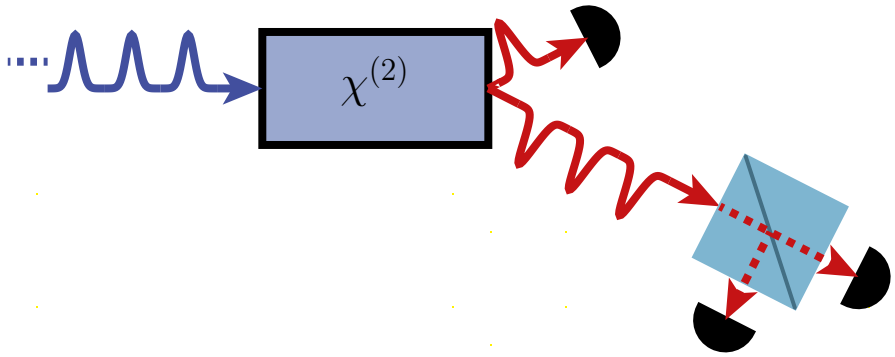

Figure 5.25: The experimental layout of the $g_{\mathrm{H}}^{(2)}$ measurement.

squeezing of $r = 0.2$ per mode. The presented frequency multiplexed source performs with a mode number of 2.5.

5.6.3 Photon number statistics: Heralded second order correlation function

In the previous section we established that the frequency multiplexing source has an increased emission probability for heralded single photons. So far we have not investigated if this increase is due to the feed forward process and the selection of different spectral bins or if additional photons pollute the source output. We will now discuss the measurement of the $g_{\mathrm{H}}^{(2)}$, assessing the contribution of higher order photon terms.

The correlation measurement consists of adding a beam splitter in the signal path and then measuring the three-fold coincidences between the herald and two signal detectors, see Fig. 5.25. The $g_{\mathrm{H}}^{(2)}$ in the weak squeezing limit for coincidence counts C in different channels, as indicated by the indices, is then given by [171,172]

$$g_{\mathrm{H}}^{(2)} = \frac{C_{\mathrm{H,S1,S2}}\, C_{\mathrm{H}}}{C_{\mathrm{H,S1}} C_{\mathrm{H,S2}}}. \tag{5.10}$$

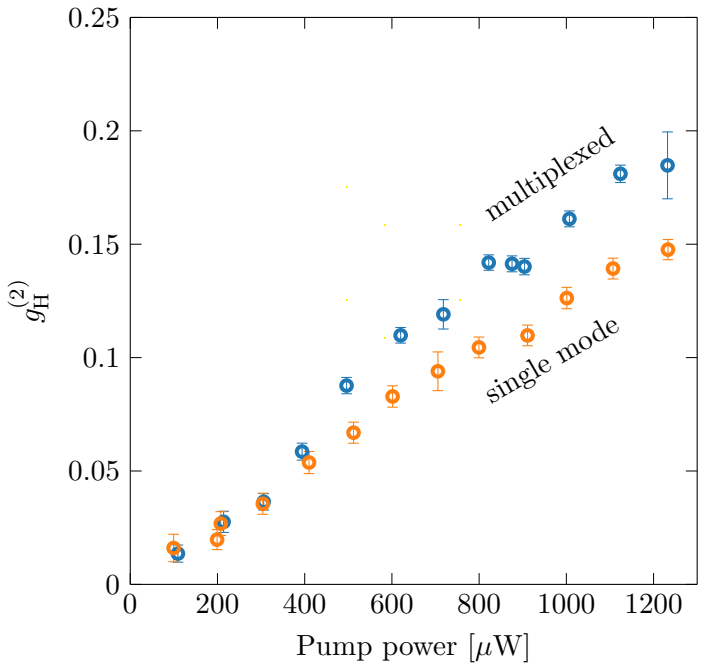

Figure 5.26: The measured $g_{\mathrm{H}}^{(2)}$ for activated feed forward control, blue, or a quasi single mode source, orange, remains constant and increases linearly with the pump power.

We expect that the $g_{\mathrm{H}}^{(2)}$ is constant for a given power, independent of activated multiplexing or not. This is the case because of the uniformity of the correlated spectrum where feed forward control effectively translates the entire JSA. This translation modulates the spectrum but does not change the statistical properties of the mode which passes the signal filter. The measurement, displayed in Fig. 5.26, where the $g_{\mathrm{H}}^{(2)}$ is plotted versus the pump power, confirms this expectation. The $g_{\mathrm{H}}^{(2)}$ is similar for activated feed forward control and the quasi single mode source but rises with increasing pump power, i.e. squeezing, due to additional higher photon number pollution. The slight separation can be explained by pump power variations as well as efficiency changes over the acquisition time.

An alternative representation of the data that takes into account the change of the coincidence detection probability, is depicted in Fig. 5.27. Now the advantage of using a multiplexing scheme becomes clear. For the frequency multiplexed single photon source the

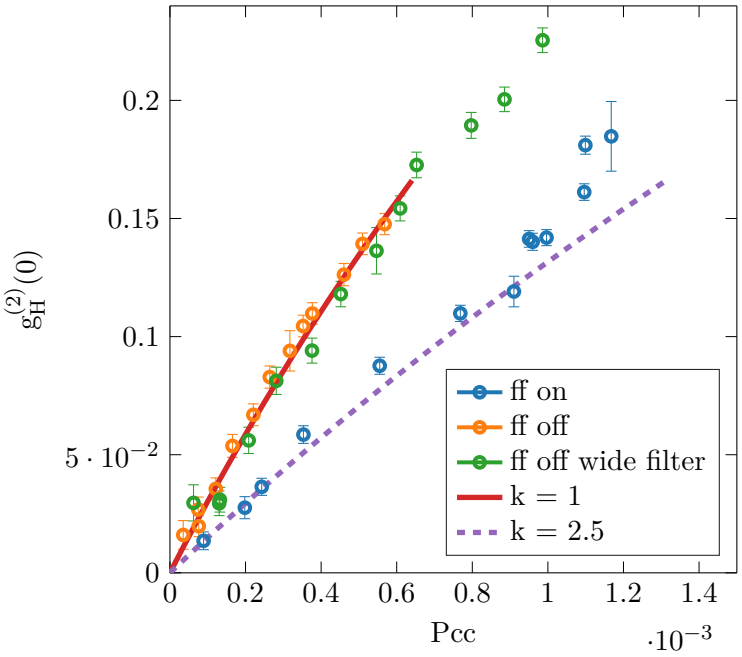

Figure 5.27: The measured $g_{\mathrm{H}}^{(2)}$ with respect to P_{CC} is displayed for activated feed forward control, blue, and a quasi single mode source, orange data points. Enlarging the herald detection window does not improve the $g_{\mathrm{H}}^{(2)}$, green data points. Along side the acquired dataset simulated curves for $K = 1$, solid red line, and $K = 2.5$, dashed purple line, independent squeezers with similar loss parameters are displayed.

contribution of higher photon number terms is reduced for a fixed coincidence detection probability in comparison to a single mode source, and the non-multiplexed source with a wide herald filter. Increasing the herald filter width does not improve the $g_{\mathrm{H}}^{(2)}$, since a larger coincidence detection probability is counteracted by a larger $g_{\mathrm{H}}^{(2)}$. The datasets displayed in Fig. 5.27 are compared with the theoretical model of κ equally squeezed modes as introduced in Chapter 3.4. This means that the effective mode number K is also the number of modes κ of the simulation. Table 5.4 states the losses taken into account for these simulations. We observe very good agreement between the single mode case and the dataset for which no feed forward control is used. The dataset with feed forward control engaged agrees well with an effective mode number of $K = 2.5$ independent modes. The effective mode-number inferred from this simulation is not an integer as one might expect

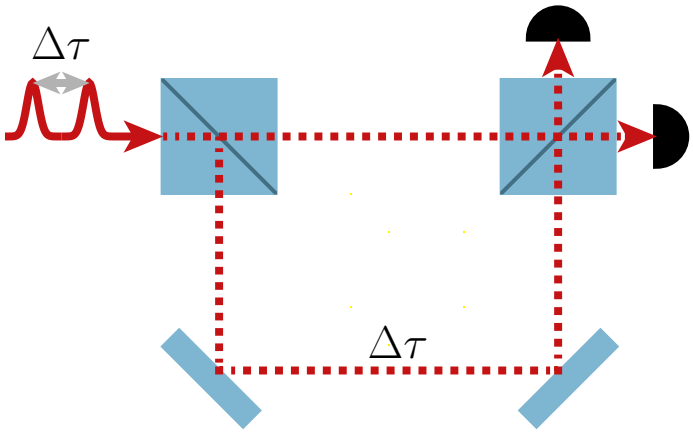

Figure 5.28: The set-up to measure HOM interference resembles a Mach-Zehnder interferometer with a tunable time delay.

when considering independent multiplexed modes. The frequency multiplexed source in the experiment is rather implemented with a continuous frequency band of several modes which cannot be separated easily in the spectral domain.

5.6.4 Hong, Ou and Mandel interference

We have learned that the photon number statistics measured for the frequency multiplexed source show improved source performance compared to a single mode source with the same loss parameters. The contribution of higher photon number terms also remains comparatively low for an increased single photon emission rate. The next characterisation measurement of the frequency multiplexed source is the purity of the emitted single photons and the indistinguishability of consecutive emission.

The photons emitted from the source are coupled into a Mach-Zehnder interferometer, Fig. 5.28, which probabilistically interferes photons from consecutive emissions separated by three pump pulse cycles. Two detectors at the output of the interferometer register arriving

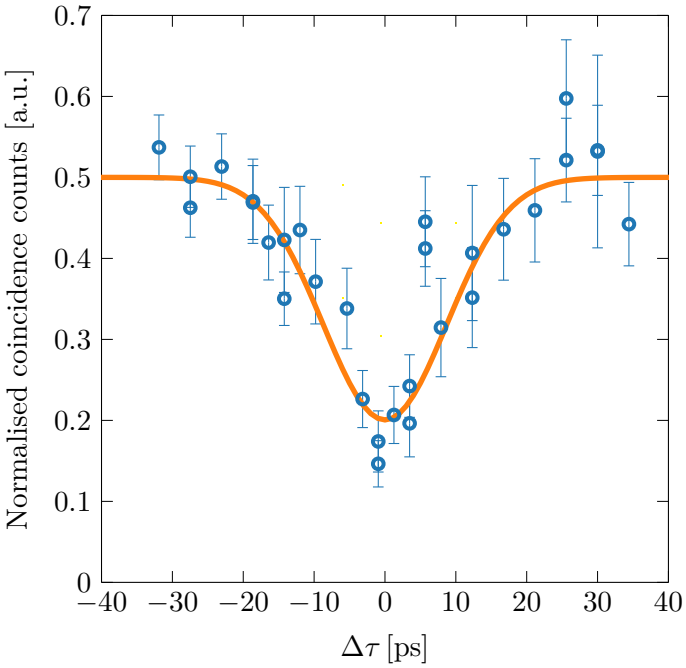

Figure 5.29: The measured HOM interference for varied time delays $\Delta\tau$ between consecutive emissions of the frequency multiplexed single photon source. The inferred visibility from the fitted inverse Gaussian function is 0.613(44) and the width corresponds to 21.3(21) ps.

photons, and count statistics for the coincidence events are recorded. In Section 2.3, we learned that the two components of the photon detection probability amplitudes interfere destructively in a HOM experiment. We introduce distinguishability between the photons by scanning the temporal delay in one of the interferometer arms and record this HOM interference pattern. Figure 5.29 displays the recorded normalised coincidence counts with respect to the delay time. The plot also contains an inverted Gaussian fit to the acquired data for guidance. The visibility is given by,

$$V = \frac{C_{\max} - C_{\min}}{C_{\max}}. \tag{5.11}$$

For the measured HOM interference it is 0.613(44) demonstrating non-classicality. The temporal width of the interference dip is 21.3(21) ps.

Earlier, in Section 2.3, we discussed the HOM interference dip shape and how the expected purity of the output state is computed. The convolution of the temporal envelopes of the two interfering fields determines the width of the HOM dip. The emitted photons are broader than the 50 GHz output filter. Simulations of a rectangular spectral photon shape, corresponding to the pass band of the filter, indicate an expected HOM dip FWHM of 16.95 ps. This is close to the measured width of 21.3(21) ps. Additional broadening can arise from dispersion in components in the signal arm and pump chirp.

Detailed simulations conducted by T Parker take different sources of temporal jitter and the effect of chromatic dispersion into account. We already discussed in Section 5.5 that the temporal response of the FPGA has a width of 234 ps but also shows a secondary peak, see Fig. 5.16. Taking this temporal response of the FPGA into account, we can bound the heralded state purity to 0.922, as discussed in Section 3.2.2.

In Section 5.4.1 we investigated the phase stability of the RF signal. The resulting offset of the RF signal with respect to the arrival time of a photon at the EOM leads to a negligible purity reduction, to 0.997, due to imperfect shifting.

Chromatic dispersion of the delay line leads to a temporal broadening of the heralded photons. This broadening as well as initial pump chirp have a insignificant effect on the HOM visibility. Nevertheless relevant for the measured purity is the fact that heralded photons at different frequencies undergo a distinct amount of temporal delay due to the dispersion in the delay line. Even though this does not lead to incorrect frequency translation, it results in a varying timing offset between consecutive photons in the measured HOM dip. This timing uncertainty reduces the measured visibility to 0.9521.

Higher photon number emissions also reduce the purity of the measurement because a fixed amount of coincidence counts remain present even at zero time delay. The $g_{\mathrm{H}}^{(2)}$ at the pump power used for the HOM dip measurement is about 0.14. The multi photon contribution to the visibility reduction corresponds to 0.97. Combining each of these imperfections results in an expected visibility of ~ 0.85. The simulation therefore gives good indications for significant imperfections causing the visibility reduction but is still above the measured 0.613(44). Larger temporal jitter or other imperfections of the experiment such as insufficient polarisation control can explain a further decrease in the measured visibility. The simulation also predicts that the expected temporal width of the HOM dip is 19.4 ps agreeing well with the measurement of 21.3(21) ps.

5.7 Performance comparison to other photon sources

By completing the characterisation of the frequency multiplexed source we are now in a position to compare it to other single photon sources and implementations of multiplexing. Table 5.6 summarises published results of several photon sources which we will now consider. The comparison includes spatial, temporal and frequency multiplexed implementations of heralded single photon sources as well as QDs as deterministic single photon emitters.

For the multiplexed sources the mode number is in general below 10 with the exception of the temporal multiplexed sources published by F Kaneda et al.[83,147]. Compared to the work presented in this thesis, a similar realisation of a frequency multiplexed source is presented by M G Puigibert et al.[148]. They state a mode number of 3. We can understand this mode number by remembering that their source uses three frequency bins for herald photon detection. In contrast, the frequency multiplexed source presented here accesses a

Reference	Multiplexing approach	Mode number	$P_{\text{delivery}} = \frac{\text{CC}}{\text{R}}$	$g_{\text{H}}^{(2)}$	Raw visibility	Repetition rate (R) [MHz]	Coincidence counts (CC) $[\text{counts}\cdot\text{s}^{-1}]$
X Ma et al.[173]	spatial	4	$9.3\cdot10^{-5}\star\ddagger$	0.5	0.887(38)	80	$7.4\cdot10^{3}$
M Collins et al.[140]	spatial	2	$6.3\cdot10^{-8}\star$	$\leq 0.3\star$	-	$80\star\ddagger$	5
T Meany et al.[174]	spatial	3	$9.2\cdot10^{-7}\star$	$\leq 0.2\star$	-	76	$\sim$70
R Francis-Jones et al.[142]	spatial	2	$2.6\cdot10^{-5}\star$	0.18	-	10	260
G J Mendoza et al.[141]	spatial & temporal	8	$3.8\cdot10^{-6}\star$	$0.368\star$	-	80	$\sim$300
C Xiong et al.[144]	temporal	4	$6\cdot10^{-5}\star\ddagger$	$0.2\star$	0.69(34)	10	$\sim$590
R Hoggarath et al.[146]	temporal	4	$2.9\cdot10^{-4}\star$	$0.13\star$	-	1.25	360
F Kaneda et al.[83]	temporal	30	0.386†	0.479(28)	-	0.05	$19.3\cdot10^{3}\star\dagger$
F Kaneda et al.[147]	temporal	40	0.667†	0.27	0.77(3)	0.5	$333.5\cdot10^{3}$
M Puigibert[148]	frequency	3	$4.4\cdot10^{-6}\star$	0.06(1)	-	80	350
C Joshi et al.[149]	frequency	3	-	0.070(2)	-	CW	$23\cdot10^{3}$
N Somaschi et al.[70]	QD		$10^{-3}\star$	0.024(7)	0.74(7)	82	$125\cdot10^{3}$
J Loredo et al.[72]	QD		0.14†	0.0288(2)	0.603(6)	80	$3.6\cdot10^{6}$
H Wang et al.[41]	QD		$0.0855\star$	0.027(1)	0.939(3)	76	$6.5\cdot10^{6}$
this work	frequency	2.5	$1.16\cdot10^{-3}$	0.1857	0.613(44)	10	$11.6\cdot10^{3}$

Table 5.6: Comparison of the performance of different approaches to multiplexed photon sources and deterministic emitting QDs: P_{delivery} is the detection probability of a (heralded) photon in the output mode. ($\star$ inferred value, † backed out detector efficiency, ‡ experimental parameters are not clearly specified)

continuous range of herald photons. Using the same mode number definition is difficult to justify for a continuous herald frequency band since it would lead to a unreasonable large number of modes. An alternative solution could be that the photon bandwidth of the signal defines the spectral width of a mode, similar to the example of separable discrete modes see Fig. 5.24. Each mode is within the shifting range. In the limit of a infinitely large shifting range or a photon bandwidth approaching zero, the number of multiplexed modes can then be expressed as the ration of the shifting range to the photon bandwidth. For the presented source this definition yields a mode number of 3.18. This mode number seems to be reasonable but nevertheless ignores the fact that these modes are not spectrally distinct in the herald mode. The same is true for the approach of M G Puigibert et al[148]. who use the herald filter to define modes but these modes overlap spectrally in the signal field. Earlier we have introduced a model of the photon count statistics for κ modes, Section 3.4. This model resolves the difficulty by assuming κ separable modes with equal squeezing strength. For the presented source the model infers an effective mode number of $K = 2.5$ when matching it with the recorded photon count statistics.

The photon delivery probability, measured as the (heralded) photon detection probability at the output, is the first of the three significant performance measures of the sources. Many implementations remain far below the single percent probability as does this experiment. Only the previously mentioned temporal implementation with tens of modes reaches a high photon delivery probability even beyond the theoretical single mode limit of 25 %. This is achieved due to low photon loss and is aided by high squeezing. Some of the QD approaches reach a photon emission probability after an excitation of several percent. Noteworthy for this work is that some QDs perform similar in this measure with a photon detection

probability of $\sim 10^{-3}$. The photon delivery probability of the frequency multiplexed source described in this thesis is higher than that of the other pulsed frequency multiplexing source despite the lower repetition rate. This is attributed to the facts, that the squeezing is higher and the optical loss performance of the presented set-up is better.

Several of the reference publications do not measure a $g_{\mathrm{H}}^{(2)}$ and state a Coincidence to Accidentals Ratio (CAR) instead. The CAR value verifies that the detection events in the signal and idler path are correlated, as they should be, if TMSV states are emitted. If possible, simulations infer the squeezing strength and likely $g_{\mathrm{H}}^{(2)}$ values for the stated experimental parameters.

The photon delivery probability is strongly dependent on the squeezing strength. We consider therefore only the performance for maximal squeezing for all measures. The listed $g_{\mathrm{H}}^{(2)}$ performance reflects the squeezing strength. Quantum dots unsurprisingly outperform all other two mode squeezers in this measure as they are in principle single photon emitters. Besides these, many multiplexed implementations operate at a $g_{\mathrm{H}}^{(2)}$ of 0.2 or beyond for the stated photon emission rates.

Only a few experiments measure the purity of the emitted photon states. Most still require improvements for high photon indistinguishability. The interference visibilities of the QD implementations strongly relies on the interference of emitted photons within a few experiment cycles. Decoherence processes of the QDs often deteriorate these visibilities for emitted photons from intervals separated by more than $\sim 50\,\mathrm{ns}$.

The repetition rate of the experiments bounds the coincidence rates that are achieved for the different implementations. This is of importance if one strives to optimize measurement time e.g. in multi-photon interference experiments.

The last column states the measured coincidence count rates for the heralded single photon sources and the count rates of the QD experiments, which varying over a large range.

In summary we see that this experiment performs on par with most other multiplexed source implementations and characterises the emitted photon state further than some multiplexed sources by a HOM interference measurement.

5.8 Conclusion

In this chapter we studied the performance of the elements of the source and combined them to form the frequency multiplexed source. We assembled, characterised, and tested the source to demonstrate that the photon number statistics improve for a multiplexed source and that the emitted photon state is purified.

5.8.1 Possible improvements

With the description of the multiplexed source and its elements it is now possible for us to judge what possible improvements can be considered.

For multiplexed single photon sources it is essential to multiplex many modes to increase the photon emission probability. There are several improvements, which can increase the multiplexed frequency range.

First a larger range for frequency translation immediately increases the number of multiplexed modes. One approach is a higher RF power, up to the EOM damage threshold. Another solution is to adapt the RF frequency to more closely match the photon duration, maximising the slope of the modulation signal of the EOM, again increasing the shifting range. Combining both of these approaches is also possible. In addition a redesign of the

RF signal generation can simplify the set-up through the inclusion of a phase lock loop. The RF generator could for example provide the reference clock signal to which the laser system locks or lock to a higher frequency component of the laser trigger pulse train for more phase stability.

Independent of the RF system the pump field preparation can be simplified. A specialised laser system could be employed, which matches the pump bandwidth, making the filtering and SHG stage obsolete. Locking the laser system to the RF signal synthesiser might also improve the timing stability of the set-up. The pump field should also be spectrally narrowed and matched to the TOF spectrometer resolution for an optimized mode number and photon purity. Matching the pump bandwidth and the output filter will also decrease the transmission loss of the filter due to spectrally broad photon wave packets.

Optical loss is one of the major obstacles for photon sources and there are some elements with significant loss in the frequency multiplexed photon source set-up, see Table 5.4. Striking is the already mentioned transmission loss of the poorly matched output filter. Adjusting the filter bandwidth to the photon width will improve the transmission of the signal path considerably. A drawback is a possible increase in photon emission from adjacent frequency bins. The EOM contributes to the optical loss in the signal pass but the potential for large improvements for waveguided modulators seem limited.

The coupling efficiencies for both fields hold some potential for improvement. Optimizing the coupling lenses, matching the beam path length and adding eventual mode shaping can improve the coupling efficiencies especially in the herald path. Worthwhile considering is also a longer KTP chip, simplifying pump coupling and improving the output mode

shape. A longer chip will also increase the source brightness and alleviate the pump power requirements.

The loss of the FBG in the TOF spectrometer contributes substantially to the herald path inefficiency and the performance is lower than the manufacturers specifications. Investigating options to reduce the loss, especially of the circulator, can optimize its performance. Typical circulators have an insertion loss of $\sim$0.8 dB per pass.

The third field of improvements focuses on the purity of the emitted photons. To increase the measured purity of the multiplexed photon source dispersion management of the delay line is necessary. A higher spectral resolution of the herald measurement also increases the purity of the heralded state. This can be achieved by less timing jitter of the electrical signals and by an increased dispersion of the TOF spectrometer.

A separate approach is a source chip redesign which forms a cavity on the herald field[175], defining discrete frequency bins, as Fig. 5.30 depicts. The discrete bins ease the requirements on the spectral herald measurement resolution and the feed forward control settings. At the same time the purity is improved since each mode is separable.

Projected source performance

As an outlook we quantify how the discussed improvements can be implemented and compare such a set-up to an ideal single photon source. We identify possible advances in the optical loss specified for readily available components. This enhances the performance of the set-up significantly, as stated in Table 5.7. We expect considerable potential in opti-

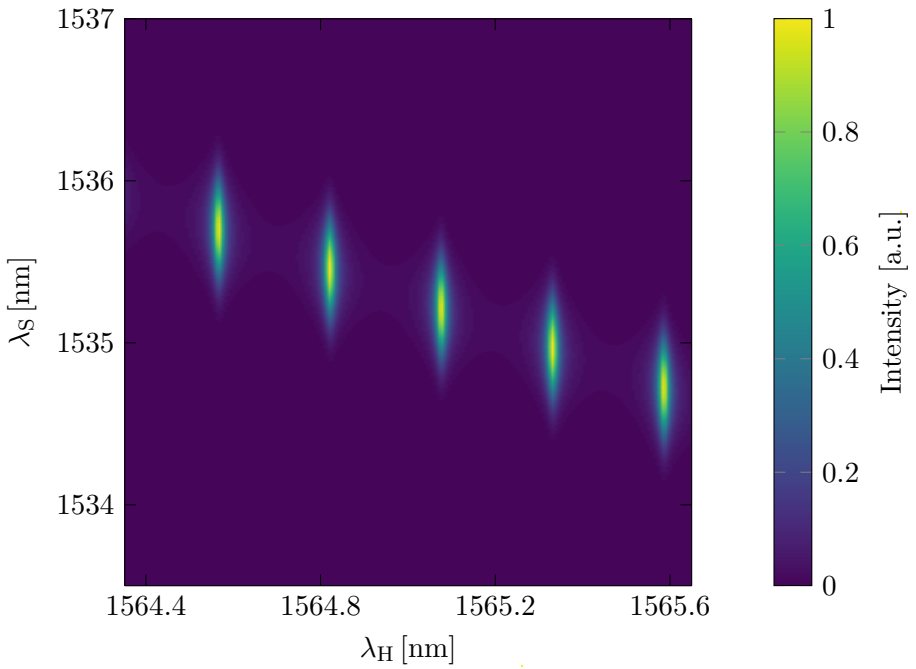

Figure 5.30: The proposed purity optimized frequency multiplexed source incorporates a cavity for the herald field, as apparent in the JSI. This discretises the frequency bins simplifying spectral resolved herald measurements and feed forward control.

Component	Current optical loss	Improved optical loss
Delay line	0.18 dB	0.06 dB
EOM	2.2 dB	1.5 dB
Signal filter insertion loss	0.46 dB	0.37 dB
Signal filter bandwidth mismatch	2.899 dB	0 dB
Signal fibre coupling	1.5 dB	0.45 dB
Total signal loss	7.24 dB	2.38 dB
Bragg grating of TOF spectrometer	4.6 dB	2.6 dB
Herald fibre coupling	3 dB	0.45 dB
Total herald loss	7.6 dB	3.05 dB
Detection efficiency	0.97 dB	0.22 dB

Table 5.7: Summary of the loss properties of the frequency multiplexed source and realistic improvements. The improvements are based on current device specifications stated by manufactures, while the presented source is specified by the device performance measured. In addition to these we assume an improvement of the coupling and detection efficiencies.

mizing the coupling efficiencies of the signal and herald fields to single mode optical fibres. Since these calculations include detection efficiencies we also assume an improvement of new detectors up to 95 % efficiency, where SNSPDs with 93 % detection efficiency have been reported [159].

The second quantity that requires optimisation is the number of multiplexed modes. Increasing the RF power up to the damage threshold of the modulator[1] promises a mode number increase by a factor of 5.7. Reducing the pump bandwidth to half of the current width will again double the mode number and mitigate the losses due to the mismatch of the output filter in the signal path. These changes would result in mode numbers of $\kappa \geq 28$. A trade-off in reducing the photon bandwidth is that the temporal duration of the photon wave packet is increased, extending over nearly the complete linear range of the 8 GHz RF signal. Care has to be taken that temporal jitter of the RF signal does not reduce the photon purity. A second consequence of the reduced pump field bandwidth can also be the pollution of the output mode with photons emitted in adjacent frequency bin, which are now more likely to pass the output filter. The impact of this should be limited due to weak squeezing and the low occupation probability of photons in these bins.

In summary we calculate that with these changes the frequency multiplexed source delivers a heralded photon in 25.03 % of the trials at a $g_{\mathrm{H}}^{(2)}$ of 0.125. 25 % is the fundamental limit for an ideal single mode heralded single photon source with photon number resolution. Further improvements beyond the ones specified here will then outperform a single mode source. The single photon rates of the multiplexed source with the stated changes will be comparable to the highest available photon rates from QDs [41,72].

[1] Lower limits on the damage threshold of the EOM were provided in correspondence with the manufacturer.

Chapter 6

Waveguided Silica telecommunication wavelength Four-Wave Mixing sources

In this chapter we will discuss a different approach to photon pair generation. The focus is now Four-Wave Mixing (FWM) in Silica. This generates a TMSV state just as SPDC in the previous chapters. The theoretical framework to describe this process was introduced alongside the description of SPDC in Chapter 2. Here we discuss birefringent phase-matched FWM in Direct UV-Writing (DUW) Silica chips manufactured by M Posner et al.[176] at the University of Southampton.

Photon generation in Silica is appealing due to low interface loss to other optical components based on the same material such as single mode optical fibres[177]. In addition transmission loss is exceptionally low for telecommunication wavelengths[178]. The intrinsic mode matching to many optical elements holds the potential of low loss source operation and high heralding efficiencies, in an integrated platform.

An advantage of the DUW Silica chip platform is the possibility of integration with

other optical elements such as beam splitters, phase shifters, and Bragg grating filters[33,80,101,102,117,125,138,176,179]. Integration aids the scalability of experiments to more complex photonic circuits. Spring et al.[80] demonstrated a uniform array of heralded single photon sources in direct UV-written Silica chips. Here we intend to extend the capability of this platform to the telecommunication range.

A drawback of the FWM processes is the weak optical non-linearity of Silica, $\chi^{(3)} \approx 10^{-19}\,\mathrm{m}^2/\mathrm{W}$[178], limiting pump to photon conversion efficiency. In addition to this, noise processes such as Raman scattering[117,178] introduce noise photons and hamper the performance of these sources[80]. Raman scattering in Silica occurs in several frequency bands with the peak emission at 13.2 THz and extending out to 42 THz below the pump frequency[178]. We therefore investigate if noise processes persist to exist for photon generation at 1550 nm and affect the photon sources. This experiment is based on results by Spring et al.[80,117] and extends the work of transferring the emission of the idler photons to the telecommunication wavelength band[180].

6.1 Birefringence tuning of the phase-matching condition

A previous study[180] of direct UV-written waveguides in Silica showed that the central idler wavelength can be moved to the telecommunication band around 1310 nm by increasing the pump wavelength. Simulations, following the theory introduced in Chapter 2, indicate that the emission can be further tuned to idler photon wavelengths of 1550 nm and beyond. An array of simultaneously pumped heralded single photon sources benefits from a commercially available compact laser system, that drives the non-linear processes. The central

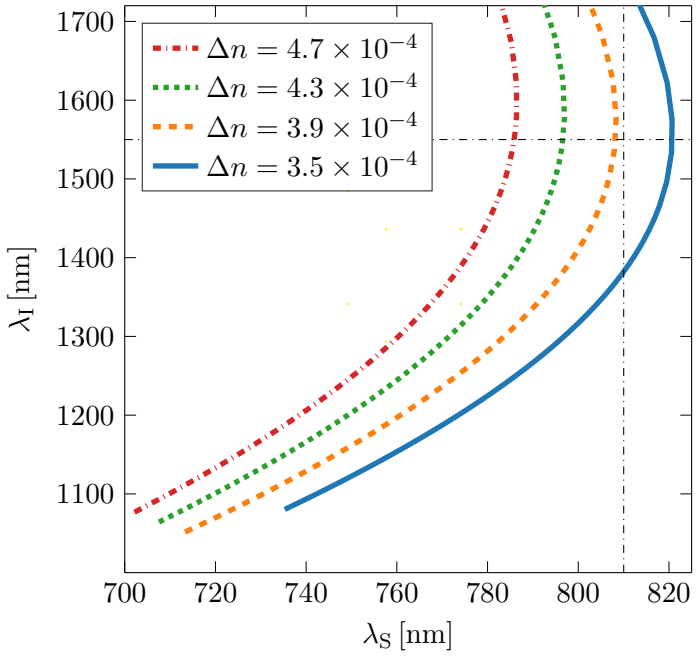

Figure 6.1: The solutions to the phase-matching condition $\Delta k = 0$ for FWM in Silica for various birefringences Δn indicate possible sets of pump, signal and idler wavelengths. The signal and idler wavelength corresponding to the targeted settings are indicated with dashed dotted black lines. A birefringence near $3.9 \cdot 10^{-4}$ is therefore optimal for the intended source operation.

pump field wavelength for idler photon emission in the telecommunication band is above $1\,\mu$m. For this wavelength range Ytterbium doped fibre lasers with emission wavelength up to 1064 nm are a plausible candidate. We now search for the birefringence required to guarantee phase-matching such that the idler photon wavelength is at 1550 nm and the pump field wavelength is within the range of Ytterbium lasers, 1030 nm to 1070 nm.

Energy conservation requires that for a pump field at 1064 nm and an idler field at 1550 nm, the signal field is centred at 810.02 nm. Figure 6.1 displays solutions to the phase-matching condition $\Delta k = 0$ for birefringences Δn between $3.5 \cdot 10^{-4}$ and $4.7 \cdot 10^{-4}$, see Section 2.1.2. The displayed phase-matching condition has a turning point such that the maximal signal wavelength is capped. An increase in birefringence translates the curve towards shorter signal wavelength. The phase-matching condition is fulfilled

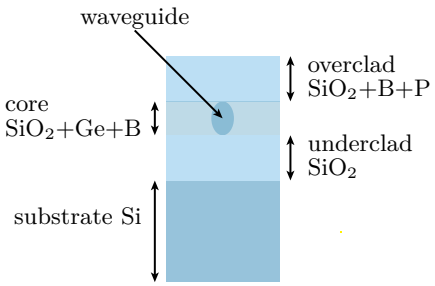

Figure 6.2: The layer structure and composition for the FWM chips manufactured at the University of Southampton. Layers of Silica (SiO_2) are placed on top of the Silicon (Si) waver by FHD. Dopants introduced in these layers change the photosensitivity, melting point and thermal expansion coefficient.

for the required wavelength ranges near a birefringence of $3.9 \cdot 10^{-4}$. This birefringence is higher than previously reported birefringences in direct UV-written Silica waveguides [181].

6.2 Direct UV-Writing of Silica-on-Silicon chips

The group of P G R Smith at the Optoelectronics Research Centre of the University of Southampton fabricated the waveguided chips. M Posner describes the fabrication process [176] in detail. Here we review the essential steps of the manufacturing process.

The manufacturing process begins by depositing layers of doped glass onto a Silicon substrate. Figure 6.2 depicts the layer structure. These commercially available substrate wafers of Silicon have a $\sim 16\,\mu$m thick thermal oxide layer. This thermal oxide layer is the under-cladding to the wave-guiding layer.

A Flame Hydrolysis Deposition (FHD) process deposits a soot layer of small glass particles on the wafer surface. In a second processing step the soot consolidates to a uniform layer while heated. First FHD forms the core layer followed by a second iteration depositing the over-cladding. In the second iteration the applied heat is below the melting

Dopant	Thermal expansion coefficient	Photo sensitivity	T_0	n
B	increase	increase	reduce	reduce
Ge	increase	increase	reduce	increase
P	increase	reduce	reduce	increase

Table 6.1: The effect of Boron (B), Germanium (Ge) and Phosporus (P) on the thermal expansion coefficient, photo sensitivity, Melting point (T_0) and Index of refraction (n) of the FWM chip layers.

point of the previously deposited core layer to prevent already consolidated layers from melting.

The introduction of dopants in the FHD process changes the properties of each layer dependent on their concentration, Fig. 6.2 and Table 6.1. The aim is to increase the birefringence with higher layer stress due to different thermal expansion coefficients. Boron, Germanium, and Phosphorus increase the thermal expansion coefficient and reduce the melting point of the glass. Germanium and Phosphorus increase the refractive index of the layer, while Boron reduces it. Boron and Germanium increase the photosensitivity of a layer while Phosphorus reduces it. This property is important for the waveguide writing process.

The concentration of dopants in the over-cladding ensures that the refractive index of the under-cladding is matched. The melting point of the top layer is also lower than the one of the core layer. Boron and Germanium make the core layer photosensitive. This composition also increases the refractive index, preparing the layer to guide optical modes. Figure 6.2 indicates the dopants of each layer. It is important to note that stress due to the different thermal expansion coefficients of the layers introduces birefringence. The dopant concentrations in turn control the thermal expansion of each layer. Several chips are diced from the wafer before the next step of waveguide writing.

DUW forms waveguides in the core layer of the chips. Hydrogen was diffused into the chips in a high-pressure chamber and increases the photosensitivity for the writing process. Once removed from the chamber, Hydrogen dissipates and the photosensitivity decreases over time again. A focused UV laser writes waveguides into the photosensitive core layer of the chips. UV light causes a localised increase of the refractive index. The change of the refractive index is likely due to induced defects and stress in the illuminated area [176]. The core layer thickness and the spot size of the writing beam define the shape of the waveguide. These parameters can be varied to match the mode size to different optical fibres. The end-facets of the chips were polished to reduce optical loss. Transmission losses on the order of $0.15\,\mathrm{dB}\cdot\mathrm{cm}^{-1}$ have been observed in these waveguides [169,176].

Besides waveguides, grating structures and beam splitters can also be formed by the DUW process. Variations of the refractive index along the waveguide form a Bragg grating. An interference pattern in the focused writing beam introduces the necessary modulation of the refractive index. Figure 6.3a depicts the two writing beams which focus on a common spot. An EOM controls the phase of one of the two beams and manipulates the interference pattern. If the phase remains unchanged a normal waveguide forms, since intensity variations are averaged out when the chip moves in the writing process. Otherwise if the phase changes as the chip moves, the fringe pattern persists and a grating structure is formed. Two crossing waveguides form a beam splitter and heating elements placed above the guides act as phase shifters. Figure 6.3b displays a typical FWM source chip layout. The waveguide spacing is matches to fibre V-groove assembly spacings and Bragg gratings in the waveguides permit waveguide testing and chip characterisation.

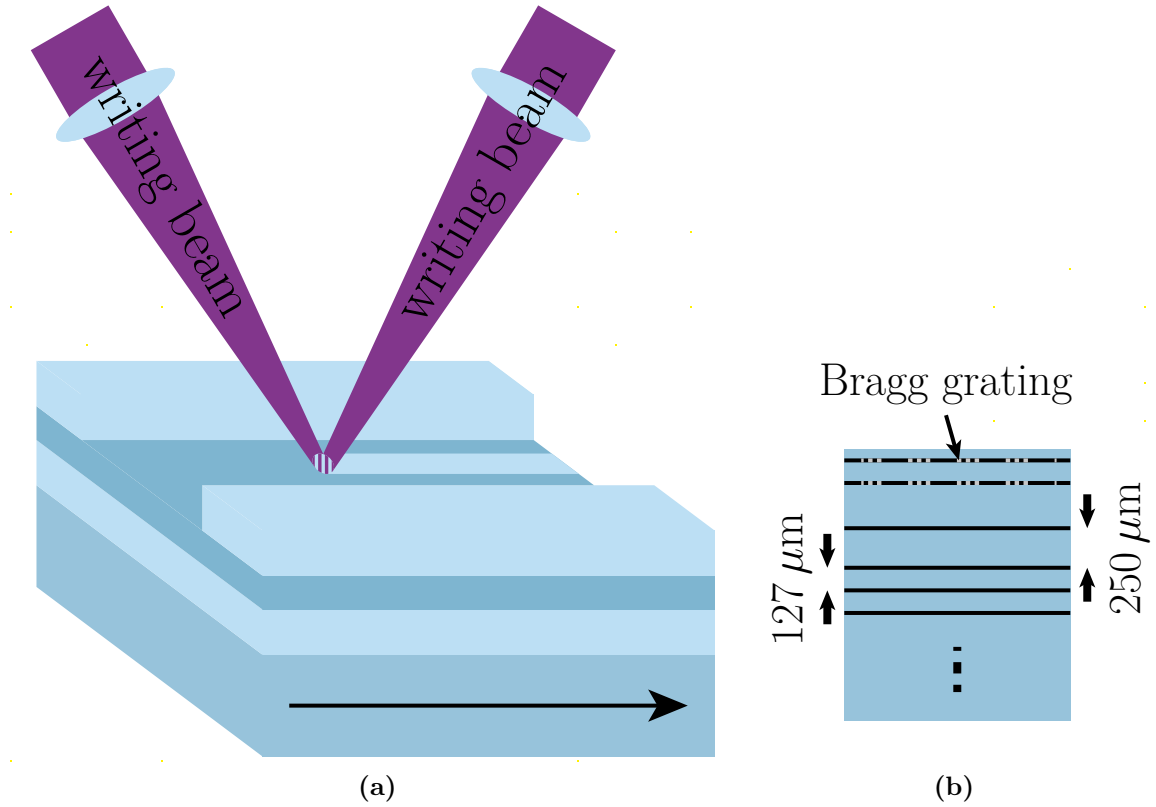

Figure 6.3: Two UV writing beams illuminate a confined region in the photosensitive layer and change the refractive index to establish waveguides in the chip (a). Controlling the phase between the two beams, while the chip is moved for writing, enables the formation of gratings. The typical layout of the waveguide arrangement of the source chips consist of groups of waveguides spaced by 250 μm (b). The waveguides in one set are separated by 127 μm a typical distance for V-groove fibre arrays. Waveguides with Bragg gratings on either side facilitate the chip characterisation.

6.2.1 Expected behaviour of the high birefringence Four-Wave Mixing chips

After fabrication M Posner characterised the waveguides of the high birefringence FWM chips[181]. The Bragg gratings in the waveguides reflect light at distinct frequencies. Figure 6.4 shows such a reflected spectrum of a broadband light source. Birefringence tunes the scattered wavelength of the gratings such that orthogonally polarised light returns different spectra. The birefringence of previous chips[80,180] NB88 is $\leq 3.5 \cdot 10^{-4}$. The increased stress between the layers lead to a measured birefringences of $4.5 - 4.9 \cdot 10^{-4}$ in the new chips,

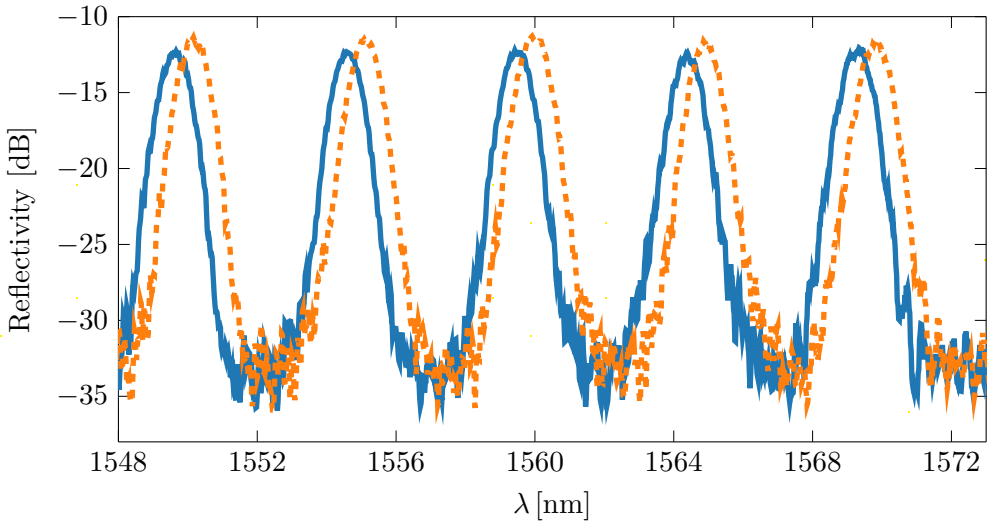

Figure 6.4: The measured reflection spectra of the FWM chip waveguide with Bragg gratings are offset for the two orthogonal polarisations along the optical axis of the waveguides due to birefringence. These datasets were provided by M Posner [181].

NB231-2-3 and NB231/2-13.

Low loss coupling to single mode optical fibre is crucial for high heralding efficiencies. A challenge of the large spectral separation of the signal and idler modes is ensuring single mode guiding of the waveguides at all required wavelengths to guarantee good coupling efficiencies. To study this we check if FWM with higher order guided modes occurs in the source chips. Different guided modes have disparate spectral dispersion and therefore support phase-matched processes at distinct wavelengths. Such secondary processes can also impact the photon source performance if they are not spectrally distinct. Simulations by M Posner predict coupling efficiencies of 78 % for the idler field and 91 % for a field at 790 nm to a polarisation maintaining fibre optimized for 980 nm.

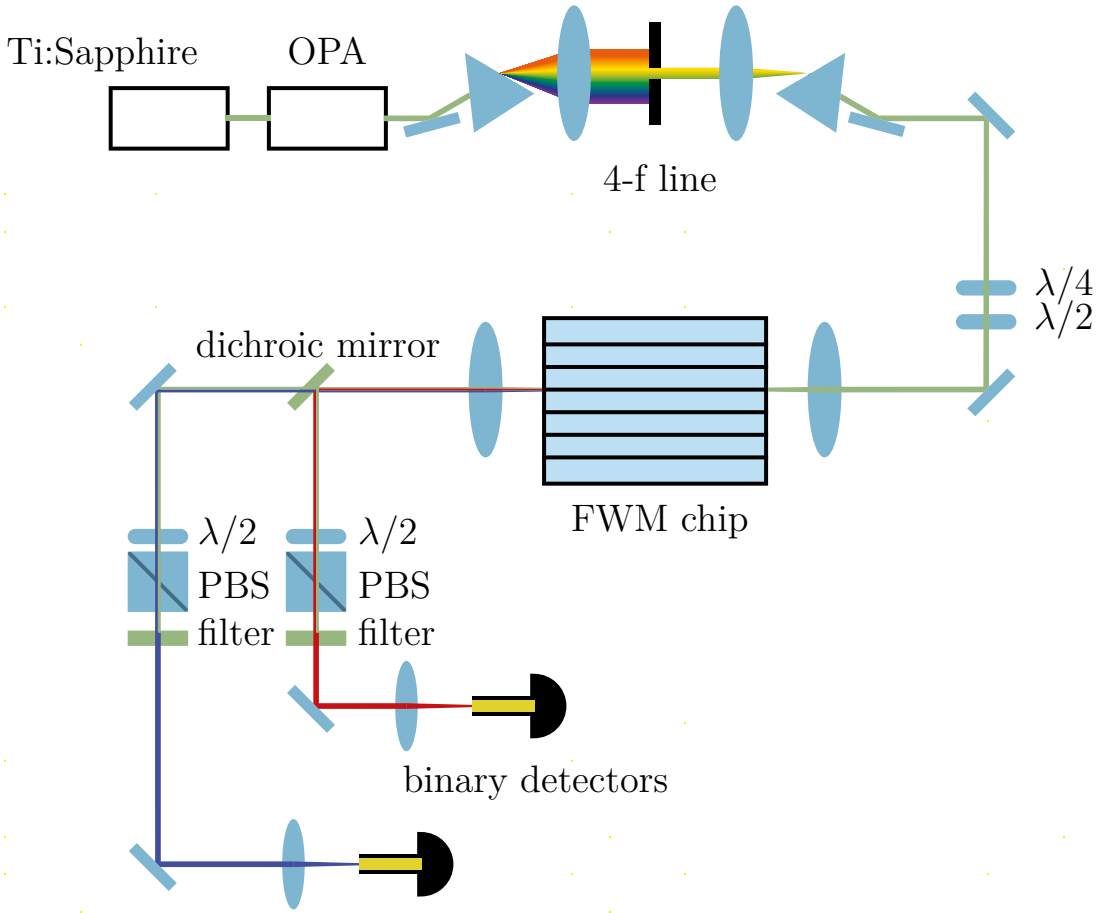

Figure 6.5: Layout of the FWM source experiment: A Ti:Sapphire laser and an OPA generate the pump field and a 4-f line was used to spectrally filter it. The dichroic mirror separates the generated signal and idler photons and single mode optical fibres collect the emission. Additional spectral filters and polarisers attenuate the pump field.

6.3 Four-Wave Mixing source set-up

Figure 6.5 displays the layout of the experiment set-up. A pulsed Titanium Sapphire (Ti:Sapphire) laser system supplies the pump field driving the FWM process. An Optical Parametric Amplifier (OPA) converts the pump laser field to the wavelength range of $1000 - 1070\,\text{nm}$ and a 4-f line shapes the pump field to a bandwidth of around $20\,\text{nm}$. Following the spectral pump preparation wave-plates adjust the pump field polarisation prior to the Silica chip.

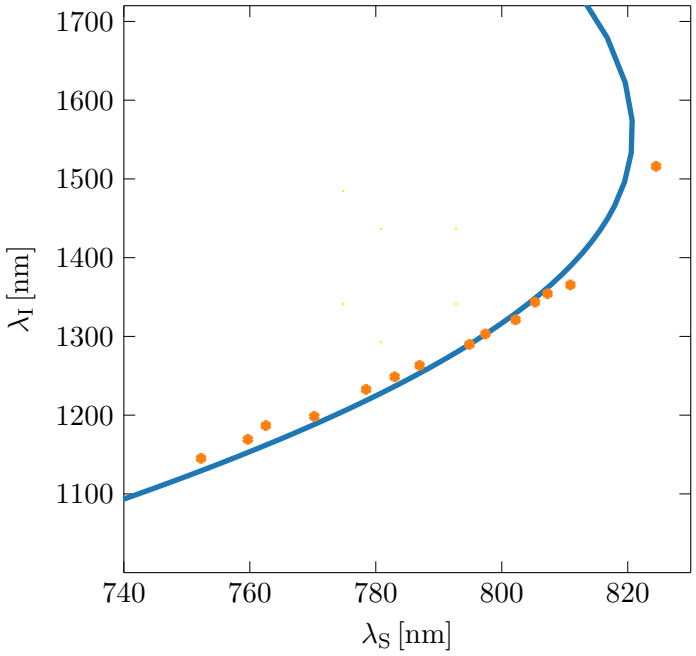

Figure 6.6: The measured phase-matched signal and idler wavelengths, orange data points, for different pump frequencies match the expected wavelength indicated by simulations, solid blue line, for chip NB-88.

A dichroic mirror splits the signal and idler fields and spectral filters attenuate the pump field. The generated photon pairs are in an orthogonal polarisation to the pump field. This allows additional polarisation filtering to fully remove pump light. The remaining signal and idler fields propagate in single mode optical fibre to the detection apparatuses for characterisation.

6.4 Four-Wave Mixing source performance

Based on previous results [180] we first extend the idler field emission range towards 1550 nm. Increasing the pump wavelength raises the signal and idler wavelength. Figure 6.6 displays the central signal and idler field wavelengths with respect to the pump field wavelength for the NB88 FWM chip. The measured values agree well with a corresponding simulation

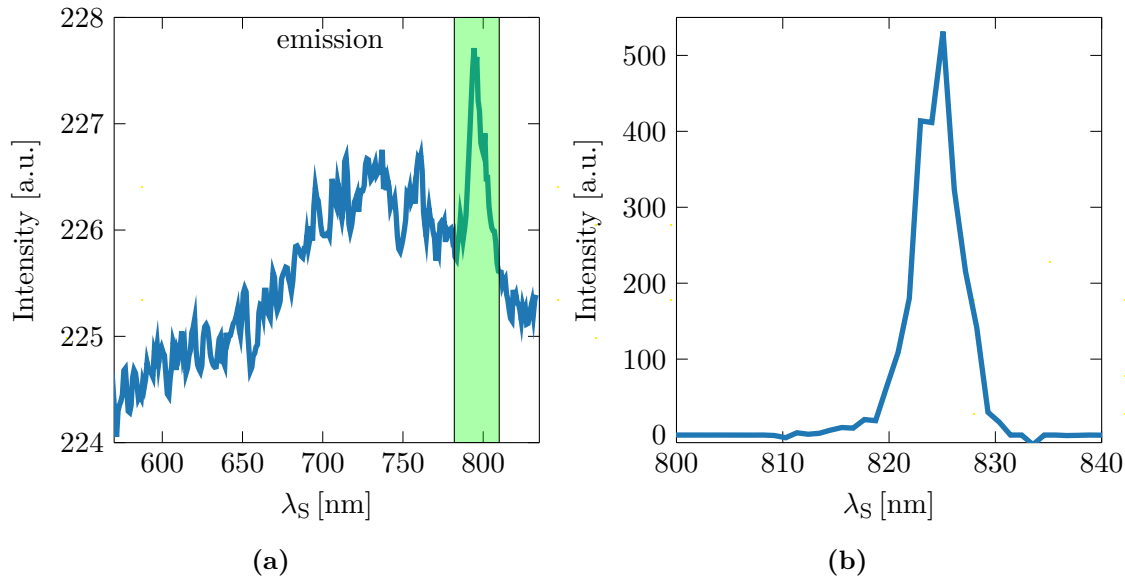

Figure 6.7: Background noise arising in the signal spectra for pump wavelength of 989.4 nm (a) is not observed for longer pump wavelength of 1069.5 nm in the heralded marginal signal spectrum (b).

which assumes a birefringence of $3.5 \cdot 10^{-4}$. The plot shows the extension of the emission range of the FWM photon source from $\sim$1310 nm to $\sim$1500 nm.

If we compare the signal spectra for a short and longer pump field wavelength, we observe a noise reduction as in Fig. 6.7. The second spectrum for longer pump wavelength, Fig. 6.7b, represents a dataset conditional on the coincidence detection of a signal and idler photon contrary to Fig. 6.7a only the signal emission is recorded. This conditional detection reduces noise contributions. Nevertheless the appearance of some noise in the marginal spectrum would be expected due to accidental coincidence events. Previous studies [80,117] of these chips observed similar noise and attributed it to the excitations of non-binding Oxygen-hole centres [182]. This Silica defect is formed by a Silicon Oxygen bond with one free electron at the Oxygen atom. Longer pump wavelength do not excite these defects, reducing the noise to detection background levels. The large separation of the signal and idler fields to the pump field also reduces the impact of noise from Raman scattering.

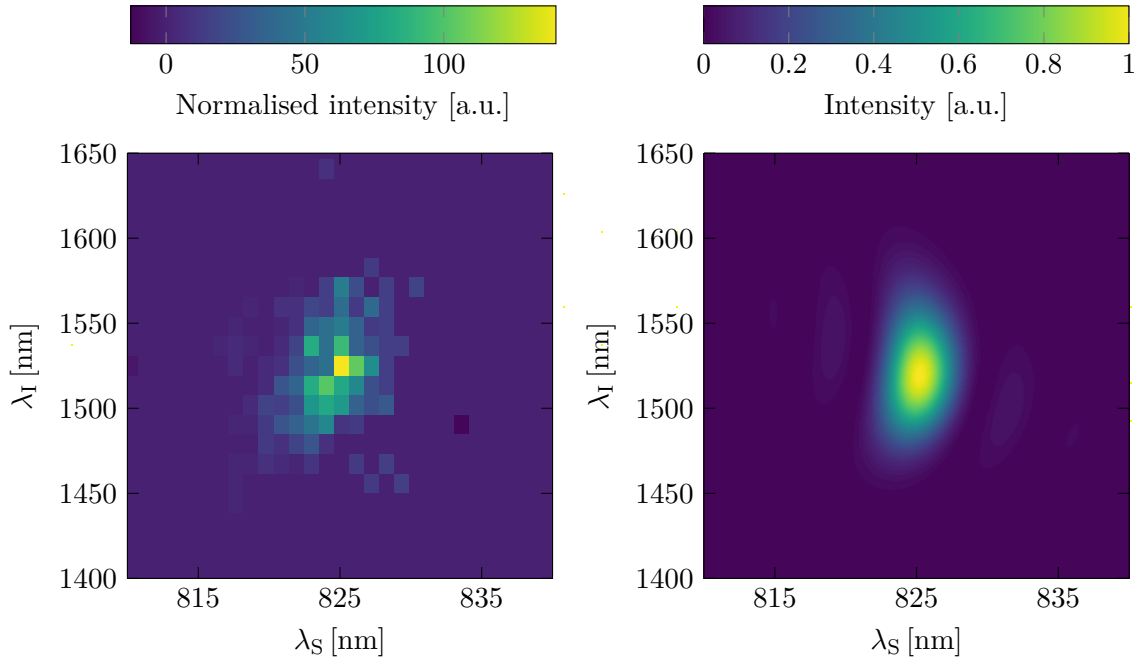

(a) NB88 **(b)** simulation

Figure 6.8: Two TOF spectrometers record the JSI of chip NB88 (a). As comparison an according simulation is displayed in (b).

Figure 6.8a displays the joint spectral characteristics of this photon source chip. Instead of the previously used TOF spectrometers with Bragg gratings, a dispersion compensating fibre[152] and a dispersive cavity structure[183] form the TOF spectrometers. The signal frequency range around 800 nm required a different dispersive device, because dispersion shifted fibres are not commonly available for this spectral range.

We investigate the photon statistics of the FWM source with APDs and Transition-Edge Sensors (TESs)[184]. TESs are superconducting detectors similar to the SNSPDs described previously in Section 4.2.1. A layer of superconducting Tungsten forms the active area. A bias current drives the detector at the edge of the transition to normal resistivity. Once a photon is absorbed by the detector it heats up. In contrast to a nanowire, absorbing

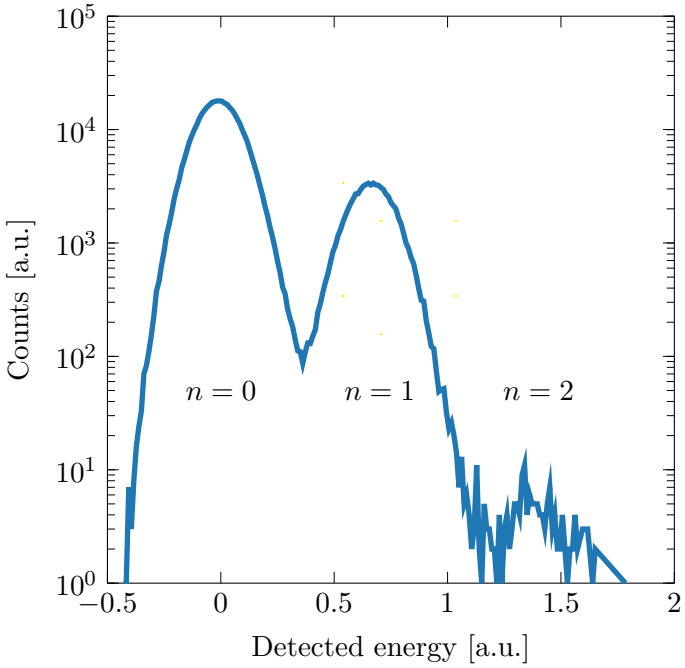

Figure 6.9: The observed photon number statistics of FWM in chip NB-88 as measured by a photon number resolving TES detector. The peaks in the histogram correspond to zero, one and two absorbed photons.

a single photon does not heat up the full detector due to the larger dimension. For this reason multiple photons can be absorbed and the detector response changes with respect to the absorbed energy, thus giving insight to the measured photon number[185–187]. The TES detector requires lower temperatures, cryogenic signal amplification, and has a slower recovery time in comparison to SNSPDs.

Figure 6.9 shows heralded photon number statistics of the idler field recorded with a TES. The first peak in the histogram corresponds to no detection events or the vacuum component. The next two peaks indicate the contributions of a single and two absorbed photons. We can use this measurement to determine the photon count characteristics of the direct UV-written Silica chip FWM source, as listed in Table 6.2. A separate measurement with APDs measures an optimal $g^{(2)}$ of 1.81 and therefore a mode number of 1.24, see

Parameter	Value
Squeezing r	0.0107
$g^{(2)}$	1.805
Effective mode number K	1.242
$g_{\mathrm{H}}^{(2)}$	0.0017
Klyshko efficiency	0.1614

Table 6.2: FWM photon count statistics: Summary of the characterisation of chip NB88. The pump beam was centred at ∼995 nm for this measurement.

Eq. 2.43, for this FWM chip at a pump bandwidth of 22.5 nm and central wavelength of ∼ 1070 nm.

In the next step we investigate the spectral properties of the new optimized DUW Silica chips with increased birefringence, NB231-2-3 and NB231/2-13. We expect that the photon number statistics remain comparable for all chips since only the birefringence changed. A seeded JSI measurement unveils the spectral characteristics of the non-linear process. This time a spectrometer sensitive to a few photons measures seeded spectra in the signal mode. A tunable seed laser in the idler mode stimulates the non-linear process and is tuned to a different wavelength for each acquired spectrometer trace. This measurement method enables a higher resolution in the measured joint spectra [168], compared to the previous measurements of chip NB88.

Figure 6.10 shows the measured and simulated JSIs for the two source chips. Table 6.3 summarises the measurement and simulation parameters. We see for NB231-2-3 in Figure 6.10a and NB231/2-13 in Figure 6.10c that the idler wavelength is close to the intended wavelength of 1550 nm and that the orientations of the joint spectra are nearly vertical. The low signal to noise ratio of the spectrometer and amplitude offsets between the individual measured slices of the spectra prevent the estimation of a lower bound to the mode number.

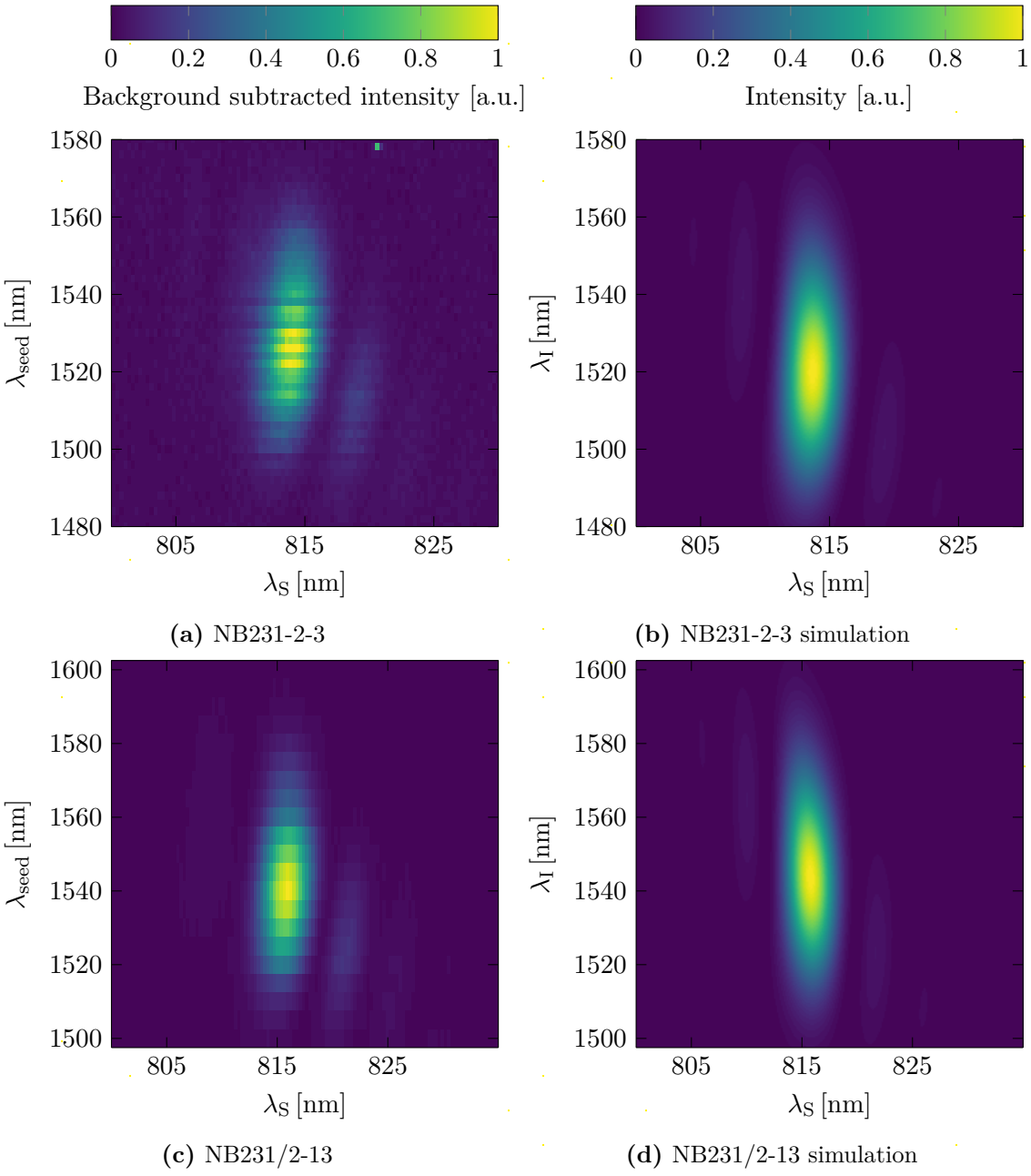

(a) NB231-2-3

(b) NB231-2-3 simulation

(c) NB231/2-13

(d) NB231/2-13 simulation

Figure 6.10: The spectral characterisation of the chip compares measured seeded JSIs (left) with according simulations (right). The measured parameters are summarised in Table 6.3.

	NB88		NB231-2-3		NB231/2-13	
Parameter	Measured	Simulated	Measured	Simulated	Measured	Simulated
λ_P [nm]	$\sim$1069.5	1069.5	$\sim$1067	1060	$\sim$1067	1067.5
$\Delta\lambda_P$ [nm]	$\sim$22.7	22.7	$\sim$16.4	16	$\sim$15	15
λ_S [nm]	825(1)	825.1	814.2(3)	813.6	815.9(3)	815.7
λ_I [nm]	1525(12)	1518.8	1526(2)	1519.9	1540(5)	1543.5
Δn		$3.35\cdot10^{-4}$	$4.5(2)\cdot10^{-4}$	$3.7\cdot10^{-4}$	$4.9(2)\cdot10^{-4}$	$3.65\cdot10^{-4}$
K		1.09		1.10		1.09
Purity		0.916		0.906		0.918

Table 6.3: Summary of the FWM experiment and simulation parameters: The simulations assume a chip length of 4 cm.

The measurements resolve the first side lobe of the phase-matching function, confirming high sensitivity of the measurement set-up. It is also clear that we do not observe any other modes in these spectral regions or fluorescence. This is an encouraging result for a heralded pure single photon source. An additional spectral filter on the signal mode can remove the side lobe and increase the purity of the heralded state.

The simulations of the two FWM chips match reasonably well with the experiment. Simulations indicate a birefringence of $3.7\cdot10^{-4}$ for the NB231-2-3 chip and $3.65\cdot10^{-4}$ for NB231/2-13. These values are much lower than the measured results of the chip characterisation. One also notes that the orientation of the JSIs is slightly different from the measurements. The reason for these offsets is due to non-matching Sellmeier equations describing the refractive index of Silica. We tested three sets of Sellmeier equations [125,126,151,188] where [126] represented the data best. The new dopant composition of the chips changes the refractive index of the material and is likely to be the reason for the mismatch. In J Spring et al. [80,117] changes of the birefringence are observed when pumping the source chips over long periods. This effect is not investigated here and measurement times remained too short for this effect to be noticeable.

	Coupling efficiency
NB88 chip	
Idler (1550 nm)	71 – 75.9 %
Signal (780 nm)	66.09 %
NB231/2-13	
Idler (1550 nm)	63.29 %
Signal	-
Simulations by M Posner [176]	
Idler (1550 nm)	78 %
Signal (790 nm)	91 %

Table 6.4: The measured and expected chip to fibre coupling efficiencies for the idler field agree well, while they differ for the signal field.

In the final step, we study the profile of the guided modes in the FWM chips to estimate and understand what limits the coupling efficiencies to single mode optical fibre. A CW laser at the signal or idler field wavelength propagates through the FWM chip and to a single mode fibre, as in the source set-up Fig. 6.5. For chip NB88 we measure the optical power of these fields before and after the optical fibre and determine the coupling efficiency. A fibre V-groove is connected directly to chip NB231/2-13. The overall transmission of the chip and the V-groove as well as the chip transmission establishes the coupling efficiency. Table 6.4 summarises the measured and expected coupling efficiencies. These results agree well for the idler mode between the simulations and chip NB88. The directly connected fibre V-groove results in a worse transmission. This is because mode adaptations by e.g. telescopes in the free space set-up are not possible. The investigation of the coupling efficiency focuses on the heralded idler mode because it is most relevant for high heralding efficiencies. The optimisation for the idler mode in turn is the reason for worse efficiencies for the signal mode.

We gain further insight to the coupling efficiencies by investigating the chip mode profiles. Figure 6.11 displays mode images for the different chips at the signal and idler field wavelength ranges. An image of a fibre mode at 780 nm serves as a reference. The measured mode sizes are not the guided mode size. An additional lens imaged the beams onto the camera and a trade-off in the mode size had to be made to resolve details of the mode shape. It is obvious that the guided modes do not match the fibre mode perfectly. For all chips especially notable in NB88 the modes exhibit ellipticity, where the fibre mode is nearly perfectly round. This ellipticity is greatly reduced in the new chipsets but remains present. Further studies of the beam propagation reveal that the guides are not single mode. For future developments waveguide dimensions have to be optimised for the large spectral difference between the signal and idler field. Preferably the heralded idler mode coupling is optimized to allow for necessary high heralding efficiencies.

6.5 Outlook

In this chapter we have discussed an approach to telecommunication wavelength FWM single photon sources in direct UV-written waveguides in Silica-on-Silicon chips. DUW in Silica-on-Silicon chips demonstrated large design flexibility and control. Nevertheless improvements especially with respect to the coupling efficiency are still required.

Future developments on this platform should incorporate integration of other optical elements. We anticipate that arrays of multiple sources may be pumped by a single laser by combining it with splitter chips as depicted in Fig. 6.12a. Bragg gratings and wavelength dependent couplers, following the photon generation section, suppress the pump field and separate the signal and idler fields, Fig. 6.12b. Hence the presented technology of DUW

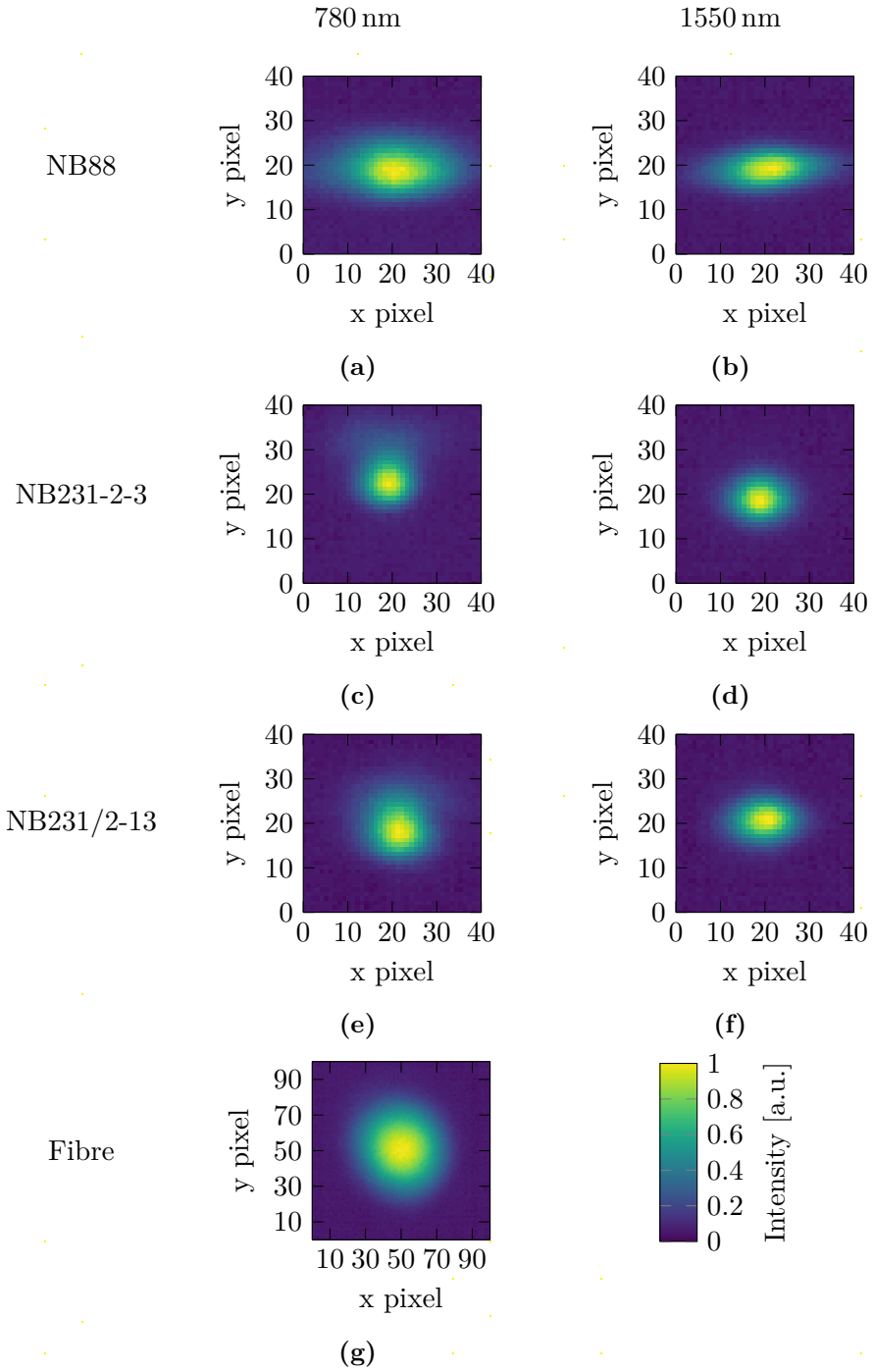

Figure 6.11: Images of the FWM chip modes at 780 nm and 1550 nm show ellipticity. These mode shapes limit coupling efficiencies due to the mismatch when directly interfaced with single mode optical fibres which have circular modes (g). The pixel size is equivalent to 5.5 μm for measurements at 780 nm and 18.98 μm for measurements at 1550 nm.

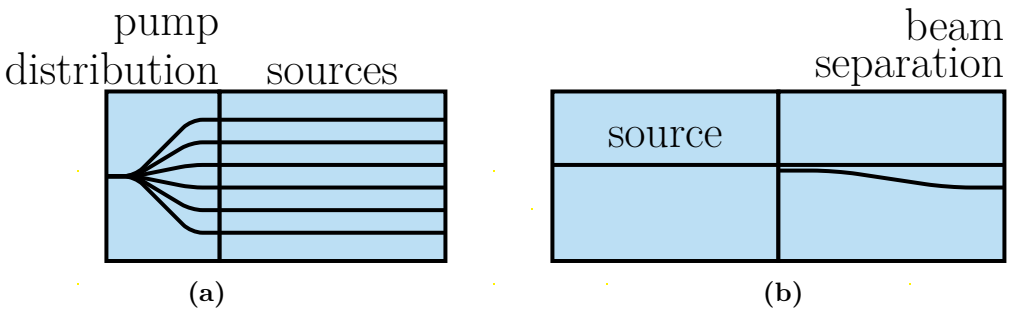

Figure 6.12: (a) the source chip can be combined with a pump distribution chip to drive several FWM sources on chip at the same time. (b) couplers and Bragg grating structures separate the signal and idler fields while suppression the pump field.

chips enables arrays of indistinguishable FWM photon sources on a monolithic platform and should greatly simplify experiments.

An alternative approach to integrated photon generation by FWM in Silica can be based on high birefringent optical fibres [92] or photonic crystal fibres [189,190]. These fibres can exhibit similar birefringences or dispersion properties with better spatial mode shape characteristics, establishing another route to high heralding efficiencies.

Chapter 7

Conclusion

PHOTONS are an essential component for the study of quantum systems and the development of new technologies in the field of quantum information processing. States of light will almost certainly remain the key information carrier to link distant qubits, within a device or between devices, and to share information on a network, such as a quantum internet [191], even if all-optical approaches to quantum computation do not succeed. This makes single photon sources an essential technology. An ideal single photon sources is capable of supplying a single photon on demand. The single photon is in a pure state and is always provided such that it is indistinguishable from any previous one.

Technologies operating with single photons face the challenge of optical loss. It is therefore of the utmost importance to explore routes which reduce transmission and interface loss. One approach is the operation at telecommunication wavelengths such as around 1550 nm where loss in optical fibre is at its minimum. Platforms, such as DUW in Silica chips, with an identical refractive index and an optical mode shape matched to fibres also help to minimise interface loss.

Heralded single photon sources are the main approach for single photon generation in experiments due to their high versatility and technological maturity. Even in the optimal operation scenario with no optical loss and photon number resolving detectors, the generation probability of photon pairs is bound to 25 %. This limits the scale of experiments that rely on the interference of several single photons.

For these reasons we have investigated two approaches to photon generation. First we discussed a continuous frequency multiplexed single photon source. Multiplexing increases the probability of delivering a single photon per trial eventually surpassing the 25 % limit. In the second approach we focused our attention on extending the photon generation in direct UV-written waveguides to 1550 nm to reduce optical transmission loss.

7.1 The frequency multiplexed source

The presented continuous frequency multiplexed single photon source is based on type-0 SPDC in periodically poled KTP. The frequency of the heralding photons of the correlated output spectrum is detected by a TOF spectrometer and a FPGA processes the photon arrival time and sets the amplitude and phase of a RF signal driving an EOM. The EOM then frequency translates the heralded signal photon to the common output mode at 1535 nm over a range of ±0.65 nm. The study of the output photon statistics indicates that the frequency multiplexed source combines the emission of effectively $K = 2.5$ modes of equal squeezing. This increases the photon emission probability by a factor of two while sustaining a constant $g_{\mathrm{H}}^{(2)}$ between 0.013 and 0.186. We measured a HOM interference visibility of 0.613(44) between consecutive photon emissions and discussed possible causes of the reduction of the state purity. In a final step the performance of the presented source was compared to other

multiplexed photon sources and QD based photon sources, where we found that it performs comparably to its contemporaries.

7.2 Telecommunication wavelength Four-Wave Mixing source

The second approach to heralded single photon generation we studied was based on FWM in DUW Silica-on-Silicon chips. We demonstrated that the translation of the idler field to the 1550 nm band is possible with pump fields supplied by commercially available Ytterbium laser systems. For this, the birefringence of the chip was increased to $3.65-3.7\cdot10^{-4}$. We studied the spectral properties of various DUW chips. In these studies no noise processes deteriorating the photon state were observed. We also analysed the photon count statistics for one of the DUW chips. To achieve the goal of a low-loss heralded single photon source coupling losses need to be minimised. For this purpose we investigated the spatial mode structure of the waveguides. Ideally the chip mode matches the mode of a single mode optical fibre. Coupling losses on a similar level as fibre to fibre coupling seem plausible, since the chip and the fibre have a very similar refractive index.

7.3 Outlook

To get closer to the requirements of the ideal single photon source several measures can be taken to improve the presented experiments.

For the frequency multiplexed source it is important to further increase the mode number and reduce the optical loss, especially on the signal mode, to surpass the photon emission

probability of spontaneous emitting single photon sources. The mode number can be increased by enlarging the frequency translation range with a stronger RF field driving the EOM. Additionally the purity of the emitted state can be increased by a new source design incorporating a cavity structure, as seen in Fig. 5.30.

FWM sources in Silica hold the promise of high coupling efficiencies to single mode optical fibres. Harnessing this advantage will lower optical loss and improve the source performance. For this further optimisations of the mode shape in the chip have to be investigated. Additionally further integration with other optical components on chip will increase the design complexity of experimental set-ups while minimizing necessary alignment and stabilisation requirements.

Improving the performance of heralded single photon sources and further integration opens up the possibility of new experiments probing the laws of quantum mechanics and implementing new protocols, and applications in quantum information processing with large numbers of single photons.

Bibliography

[1] Feynman, R. P. Simulating physics with computers. *Int J Theor Phys* **21**, 467–488 (1982).

[2] Deutsch, D. Quantum Theory, the Church-Turing Principle and the Universal Quantum Computer. *Proceedings of the Royal Society A: Mathematical, Physical and Engineering Sciences* **400**, 97–117 (1985).

[3] Shor, P. W. Algorithms for quantum computation: Discrete logarithms and factoring. In *Foundations of Computer Science, 1994 Proceedings., 35th Annual Symposium on*, 124–134 (IEEE, 1994).

[4] Grover, L. K. A fast quantum mechanical algorithm for database search. In *Proceedings of the twenty-eighth annual ACM symposium on Theory of computing*, 212–219 (ACM, 1996).

[5] DiVincenzo, D. P. The Physical Implementation of Quantum Computation. *Fortschritte der Physik* **48**, 771–783 (2000).

[6] Buluta, I., Ashhab, S. & Nori, F. Natural and artificial atoms for quantum computation. *Rep. Prog. Phys.* **74**, 104401 (2011).

[7] Simon, C. *et al.* Quantum memories - A review based on the European integrated project Qubit Applications (QAP). *Eur. Phys. J. D* **58**, 1–22 (2010).

[8] Pan, J.-W., Chen, Z.-B., Lu, C.-Y., Weinfurter, H., Zeilinger, A. & ukowski, M. Multiphoton entanglement and interferometry. *Rev. Mod. Phys.* **84**, 777–838 (2012).

[9] Saffman, M. Quantum computing with atomic qubits and Rydberg interactions: progress and challenges. *J. Phys. B: At. Mol. Opt. Phys.* **49**, 202001 (2016).

[10] Gao, W. B., Imamoglu, A., Bernien, H. & Hanson, R. Coherent manipulation, measurement and entanglement of individual solid-state spins using optical fields. *Nature Photonics* **9**, 363 (2015).

[11] Kok, P., Munro, W. J., Nemoto, K., Ralph, T. C., Dowling, J. P. & Milburn, G. J. Linear optical quantum computing with photonic qubits. *Rev. Mod. Phys.* **79**, 135–174 (2007).

[12] Suter, D. & Mahesh, T. S. Spins as qubits: Quantum information processing by nuclear magnetic resonance. *The Journal of Chemical Physics* **128**, 052206 (2008).

[13] Andersen, U. L., Neergaard-Nielsen, J. S., Loock, P. v. & Furusawa, A. Hybrid discrete- and continuous-variable quantum information. *Nature Physics* **11**, 713 (2015).

[14] Wilk, T., Gaëtan, A., Evellin, C., Wolters, J., Miroshnychenko, Y., Grangier, P. & Browaeys, A. Entanglement of Two Individual Neutral Atoms Using Rydberg Blockade. *Phys. Rev. Lett.* **104**, 010502 (2010).

[15] Isenhower, L. *et al.* Demonstration of a Neutral Atom Controlled-NOT Quantum Gate. *Phys. Rev. Lett.* **104**, 010503 (2010).

[16] Bernien, H. *et al.* Probing many-body dynamics on a 51-atom quantum simulator. *Nature* **551**, 579 (2017).

[17] Hosseini, M., Sparkes, B. M., Campbell, G., Lam, P. K. & Buchler, B. C. High efficiency coherent optical memory with warm rubidium vapour. *Nature Communications* **2**, 174 (2011).

[18] Radnaev, A. G., Dudin, Y. O., Zhao, R., Jen, H. H., Jenkins, S. D., Kuzmich, A. & Kennedy, T. a. B. A quantum memory with telecom-wavelength conversion. *Nature Physics* **6**, 894 (2010).

[19] Yang, S.-J., Wang, X.-J., Bao, X.-H. & Pan, J.-W. An efficient quantum lightmatter interface with sub-second lifetime. *Nature Photonics* **10**, 381 (2016).

[20] Kaczmarek, K. T. *et al.* High-speed noise-free optical quantum memory. *Phys. Rev. A* **97**, 042316 (2018).

[21] Chiaverini, J. *et al.* Realization of quantum error correction. *Nature* **432**, 602 (2004).

[22] Monz, T. *et al.* Realization of a scalable Shor algorithm. *Science* **351**, 1068–1070 (2016).

[23] Gärttner, M., Bohnet, J. G., Safavi-Naini, A., Wall, M. L., Bollinger, J. J. & Rey, A. M. Measuring out-of-time-order correlations and multiple quantum spectra in a trapped-ion quantum magnet. *Nature Physics* **13**, 781 (2017).

[24] Cory, D. G. *et al.* Experimental Quantum Error Correction. *Phys. Rev. Lett.* **81**, 2152–2155 (1998).

[25] Vandersypen, L. M. K. & Chuang, I. L. NMR techniques for quantum control and computation. *Rev. Mod. Phys.* **76**, 1037–1069 (2005).

[26] Negrevergne, C. *et al.* Benchmarking Quantum Control Methods on a 12-Qubit System. *Phys. Rev. Lett.* **96**, 170501 (2006).

[27] Peng, X., Liao, Z., Xu, N., Qin, G., Zhou, X., Suter, D. & Du, J. Quantum Adiabatic Algorithm for Factorization and Its Experimental Implementation. *Phys. Rev. Lett.* **101**, 220405 (2008).

[28] Pfaff, W. *et al.* Unconditional quantum teleportation between distant solid-state quantum bits. *Science* **345**, 532–535 (2014).

[29] Yang, S. *et al.* High-fidelity transfer and storage of photon states in a single nuclear spin. *Nature Photonics* **10**, 507 (2016).

[30] Kalb, N. *et al.* Entanglement distillation between solid-state quantum network nodes. *Science* **356**, 928–932 (2017).

[31] Gasparoni, S., Pan, J.-W., Walther, P., Rudolph, T. & Zeilinger, A. Realization of a Photonic Controlled-NOT Gate Sufficient for Quantum Computation. *Physical Review Letters* **93** (2004).

[32] OBrien, J. L., Pryde, G. J., White, A. G. & Ralph, T. C. High-fidelity Z-measurement error encoding of optical qubits. *Phys. Rev. A* **71**, 060303 (2005).

[33] Spring, J. B. *et al.* Boson Sampling on a Photonic Chip. *Science* **339**, 798–801 (2013).

[34] Lu, H. *et al.* Experimental realization of a concatenated GreenbergerHorneZeilinger state for macroscopic quantum superpositions. *Nature Photonics* **8**, 364–368 (2014).

[35] Wang, X.-L. *et al.* Quantum teleportation of multiple degrees of freedom of a single photon. *Nature* **518**, 516–519 (2015).

[36] Wang, X.-L. *et al.* Experimental Ten-Photon Entanglement. *Phys. Rev. Lett.* **117**, 210502 (2016).

[37] Takeda, S., Mizuta, T., Fuwa, M., van Loock, P. & Furusawa, A. Deterministic quantum teleportation of photonic quantum bits by a hybrid technique. *Nature* **500**, 315–318 (2013).

[38] Santagati, R. *et al.* Witnessing eigenstates for quantum simulation of Hamiltonian spectra. *Science Advances* **4**, eaap9646 (2018).

[39] Jin, H. *et al.* On-Chip Generation and Manipulation of Entangled Photons Based on Reconfigurable Lithium-Niobate Waveguide Circuits. *Physical Review Letters* **113** (2014).

[40] Greve, K. D. *et al.* Quantum-dot spinphoton entanglement via frequency downconversion to telecom wavelength. *Nature* **491**, 421 (2012).

[41] Wang, H. *et al.* High-efficiency multiphoton boson sampling. *Nature Photonics* **11**, 361 (2017).

[42] Stockill, R. *et al.* Phase-Tuned Entangled State Generation between Distant Spin Qubits. *Phys. Rev. Lett.* **119**, 010503 (2017).

[43] Koehl, W. F., Buckley, B. B., Heremans, F. J., Calusine, G. & Awschalom, D. D. Room temperature coherent control of defect spin qubits in silicon carbide. *Nature* **479**, 84 (2011).

[44] Heinze, G., Hubrich, C. & Halfmann, T. Stopped Light and Image Storage by Electromagnetically Induced Transparency up to the Regime of One Minute. *Phys. Rev. Lett.* **111**, 033601 (2013).

[45] Saglamyurek, E. *et al.* Quantum storage of entangled telecom-wavelength photons in an erbium-doped optical fibre. *Nature Photonics* **9**, 83 (2015).

[46] Zhong, M. *et al.* Optically addressable nuclear spins in a solid with a six-hour coherence time. *Nature* **517**, 177 (2015).

[47] Corrielli, G., Seri, A., Mazzera, M., Osellame, R. & de Riedmatten, H. Integrated Optical Memory Based on Laser-Written Waveguides. *Phys. Rev. Applied* **5**, 054013 (2016).

[48] Song, C. *et al.* 10-Qubit Entanglement and Parallel Logic Operations with a Superconducting Circuit. *Phys. Rev. Lett.* **119**, 180511 (2017).

[49] Knill, E., Laflamme, R. & Milburn, G. J. A scheme for efficient quantum computation with linear optics. *nature* **409**, 46–52 (2001).

[50] Gordon, J. P., Zeiger, H. J. & Townes, C. H. The Maser—New Type of Microwave Amplifier, Frequency Standard, and Spectrometer. *Phys. Rev.* **99**, 1264–1274 (1955).

[51] Maiman, T. H. Stimulated Optical Radiation in Ruby. *Nature* **187**, 493 (1960).

[52] Franken, P. A., Hill, A. E., Peters, C. e. & Weinreich, G. Generation of optical harmonics. *Physical Review Letters* **7**, 118 (1961).

[53] Giordmaine, J. A. Mixing of light beams in crystals. *Physical Review Letters* **8**, 19 (1962).

[54] Maker, P. D., Terhune, R. W., Nisenoff, M. & Savage, C. M. Effects of dispersion and focusing on the production of optical harmonics. *Physical Review Letters* **8**, 21 (1962).

[55] Burnham, D. C. & Weinberg, D. L. Observation of simultaneity in parametric production of optical photon pairs. *Physical Review Letters* **25**, 84 (1970).

[56] Eisaman, M. D., Fan, J., Migdall, A. & Polyakov, S. V. Invited Review Article: Single-photon sources and detectors. *Review of Scientific Instruments* **82**, 071101 (2011).

[57] Lounis, B. & Orrit, M. Single-photon sources. *Rep. Prog. Phys.* **68**, 1129 (2005).

[58] Buckley, S., Rivoire, K. & Vukovi, J. Engineered quantum dot single-photon sources. *Rep. Prog. Phys.* **75**, 126503 (2012).

[59] Aharonovich, I., Englund, D. & Toth, M. Solid-state single-photon emitters. *Nature Photonics* **10**, 631 (2016).

[60] Kuhn, A., Hennrich, M. & Rempe, G. Deterministic Single-Photon Source for Distributed Quantum Networking. *Phys. Rev. Lett.* **89**, 067901 (2002).

[61] Hijlkema, M., Weber, B., Specht, H. P., Webster, S. C., Kuhn, A. & Rempe, G. A single-photon server with just one atom. *Nature Physics* **3**, 253 (2007).

[62] Higginbottom, D. B., Slodika, L., Araneda, G., Lachman, L., Filip, R., Hennrich, M. & Blatt, R. Pure single photons from a trapped atom source. *New J. Phys.* **18**, 093038 (2016).

[63] Lounis, B. & Moerner, W. E. Single photons on demand from a single molecule at room temperature. *Nature* **407**, 491 (2000).

[64] Chu, X.-L., Götzinger, S. & Sandoghdar, V. A single molecule as a high-fidelity photon gun for producing intensity-squeezed light. *Nature Photonics* **11**, 58 (2017).

[65] Bernien, H., Childress, L., Robledo, L., Markham, M., Twitchen, D. & Hanson, R. Two-Photon Quantum Interference from Separate Nitrogen Vacancy Centers in Diamond. *Phys. Rev. Lett.* **108**, 043604 (2012).

[66] Benedikter, J. *et al.* Cavity-Enhanced Single-Photon Source Based on the Silicon-Vacancy Center in Diamond. *Phys. Rev. Applied* **7**, 024031 (2017).

[67] Riedel, D. *et al.* Deterministic Enhancement of Coherent Photon Generation from a Nitrogen-Vacancy Center in Ultrapure Diamond. *Phys. Rev. X* **7**, 031040 (2017).

[68] Wan, N. H. *et al.* Efficient Extraction of Light from a Nitrogen-Vacancy Center in a Diamond Parabolic Reflector. *Nano Lett.* **18**, 2787–2793 (2018).

[69] Ding, X. *et al.* On-Demand Single Photons with High Extraction Efficiency and Near-Unity Indistinguishability from a Resonantly Driven Quantum Dot in a Micropillar. *Phys. Rev. Lett.* **116**, 020401 (2016).

[70] Somaschi, N. *et al.* Near-optimal single-photon sources in the solid state. *Nat Photon* **10**, 340–345 (2016).

[71] Thoma, A. *et al.* Exploring Dephasing of a Solid-State Quantum Emitter via Time- and Temperature-Dependent Hong-Ou-Mandel Experiments. *Phys. Rev. Lett.* **116**, 033601 (2016).

[72] Loredo, J. C. *et al.* Scalable performance in solid-state single-photon sources. *Optica, OPTICA* **3**, 433–440 (2016).

[73] Kiransk, G. *et al.* Indistinguishable and efficient single photons from a quantum dot in a planar nanobeam waveguide. *Phys. Rev. B* **96**, 165306 (2017).

[74] Loudon, R. *The quantum theory of light.* Oxford science publications (Oxford University Press, Oxford; New York, 2000), 3rd ed edn.

[75] A photon checks into a hotel and the porter asks him if he has any luggage. The photon replies: "No, I'm travelling light." (2013). URL `http://www.independent.co.uk/news/science/how-many-surrealists-does-it-take-to-screw-in-a-light-bulb-a-fish-the-most-highbrow-jokes-in-the-8691191.html`.

[76] Pelton, M., Santori, C., Vuckovi, J., Zhang, B., Solomon, G. S., Plant, J. & Yamamoto, Y. Efficient Source of Single Photons: A Single Quantum Dot in a Micropost Microcavity. *Phys. Rev. Lett.* **89**, 233602 (2002).

[77] Englund, D., Majumdar, A., Faraon, A., Toishi, M., Stoltz, N., Petroff, P. & Vukovi, J. Resonant Excitation of a Quantum Dot Strongly Coupled to a Photonic Crystal Nanocavity. *Phys. Rev. Lett.* **104**, 073904 (2010).

[78] Barclay, P. E., Fu, K.-M. C., Santori, C., Faraon, A. & Beausoleil, R. G. Hybrid Nanocavity Resonant Enhancement of Color Center Emission in Diamond. *Phys. Rev. X* **1**, 011007 (2011).

[79] Weston, M. M. *et al.* Efficient and pure femtosecond-pulse-length source of polarization-entangled photons. *Opt. Express, OE* **24**, 10869–10879 (2016).

[80] Spring, J. B. *et al.* Chip-based array of near-identical, pure, heralded single-photon sources. *Optica, OPTICA* **4**, 90–96 (2017).

[81] Barz, S., Cronenberg, G., Zeilinger, A. & Walther, P. Heralded generation of entangled photon pairs. *Nature Photonics* **4**, 553–556 (2010).

[82] Tanida, M., Okamoto, R. & Takeuchi, S. Highly indistinguishable heralded single-photon sources using parametric down conversion. *Optics express* **20**, 15275–15285 (2012).

[83] Kaneda, F., Christensen, B. G., Wong, J. J., Park, H. S., McCusker, K. T. & Kwiat, P. G. Time-multiplexed heralded single-photon source. *Optica, OPTICA* **2**, 1010–1013 (2015).

[84] Eckstein, A., Christ, A., Mosley, P. J. & Silberhorn, C. Highly Efficient Single-Pass Source of Pulsed Single-Mode Twin Beams of Light. *Physical Review Letters* **106** (2011).

[85] Harder, G., Ansari, V., Brecht, B., Dirmeier, T., Marquardt, C. & Silberhorn, C. An optimized photon pair source for quantum circuits. *Optics express* **21**, 13975–13985 (2013).

[86] Jin, R.-B. *et al.* Spectrally resolved Hong-Ou-Mandel interference between independent photon sources. *Opt. Express, OE* **23**, 28836–28848 (2015).

[87] Mosley, P. J. *Generation of Heralded Single Photons in Pure Quantum States.* Doctor of Philosophy, University of Oxford (2007).

[88] Mosley, P. J., Lundeen, J. S., Smith, B. J., Wasylczyk, P., URen, A. B., Silberhorn, C. & Walmsley, I. A. Heralded Generation of Ultrafast Single Photons in Pure Quantum States. *Physical Review Letters* **100** (2008).

[89] Luo, K.-H. *et al.* Direct generation of genuine single-longitudinal-mode narrowband photon pairs. *New J. Phys.* **17**, 073039 (2015).

[90] Montaut, N., Sansoni, L., Meyer-Scott, E., Ricken, R., Quiring, V., Herrmann, H. & Silberhorn, C. High-Efficiency Plug-and-Play Source of Heralded Single Photons. *Phys. Rev. Applied* **8**, 024021 (2017).

[91] Atzeni, S. *et al.* Integrated sources of entangled photons at the telecom wavelength in femtosecond-laser-written circuits. *Optica, OPTICA* **5**, 311–314 (2018).

[92] Söller, C., Cohen, O., Smith, B. J., Walmsley, I. A. & Silberhorn, C. High-performance single-photon generation with commercial-grade optical fiber. *Physical Review A* **83** (2011).

[93] Clark, A. *et al.* Intrinsically narrowband pair photon generation in microstructured fibres. *New Journal of Physics* **13**, 065009 (2011).

[94] Spring, J. B. *et al.* On-chip low loss heralded source of pure single photons. *Optics express* **21**, 13522–13532 (2013).

[95] Preble, S. F., Fanto, M. L., Steidle, J. A., Tison, C. C., Howland, G. A., Wang, Z. & Alsing, P. M. On-Chip Quantum Interference from a Single Silicon Ring-Resonator Source. *Phys. Rev. Applied* **4**, 021001 (2015).

[96] Ramelow, S., Farsi, A., Clemmen, S., Orquiza, D., Luke, K., Lipson, M. & Gaeta, A. L. Silicon-Nitride Platform for Narrowband Entangled Photon Generation. *arXiv:1508.04358 [physics, physics:quant-ph]* (2015).

[97] Silverstone, J. W., Bonneau, D., OBrien, J. L. & Thompson, M. G. Silicon Quantum Photonics. *IEEE Journal of Selected Topics in Quantum Electronics* **22**, 390–402 (2016).

[98] Harris, N. C. *et al.* Quantum transport simulations in a programmable nanophotonic processor. *Nature Photonics* **11**, 447 (2017).

[99] Carolan, J. *et al.* Universal linear optics. *Science* **349**, 711–716 (2015).

[100] Wang, J. *et al.* Multidimensional quantum entanglement with large-scale integrated optics. *Science* eaar7053 (2018).

[101] Metcalf, B. J. *et al.* Multiphoton quantum interference in a multiport integrated photonic device. *Nature Communications* **4**, 1356 (2013).

[102] Metcalf, B. J. *et al.* Quantum teleportation on a photonic chip. *Nature Photonics* **8**, 770 (2014).

[103] Crespi, A. *et al.* Suppression law of quantum states in a 3d photonic fast Fourier transform chip. *Nature Communications* **7**, 10469 (2016).

[104] Eckstein, A. *Mastering quantum light pulses with nonlinear waveguide interactions*. Doctor of Philosophy, Friedrich-Alexander-Universität Erlangen-Nürnberg (2012).

[105] Mosley, P. J., Christ, A., Eckstein, A. & Silberhorn, C. Direct measurement of the spatial-spectral structure of waveguided parametric down-conversion. *Phys. Rev. Lett.* **103**, 233901 (2009).

[106] URen, A. B., Silberhorn, C., Banaszek, K. & Walmsley, I. A. Efficient Conditional Preparation of High-Fidelity Single Photon States for Fiber-Optic Quantum Networks. *Physical Review Letters* **93** (2004).

[107] Christ, A. & Silberhorn, C. Limits on the deterministic creation of pure single-photon states using parametric down-conversion. *Physical Review A* **85** (2012).

[108] Li, Y., Humphreys, P. C., Mendoza, G. J. & Benjamin, S. C. Resource Costs for Fault-Tolerant Linear Optical Quantum Computing. *Phys. Rev. X* **5**, 041007 (2015).

[109] Pittman, T. B., Jacobs, B. C. & Franson, J. D. Single photons on pseudodemand from stored parametric down-conversion. *Phys. Rev. A* **66**, 042303 (2002).

[110] Migdall, A. L., Branning, D. & Castelletto, S. Tailoring single-photon and multiphoton probabilities of a single-photon on-demand source. *Phys. Rev. A* **66**, 053805 (2002).

[111] Nunn, J. *et al.* Enhancing Multiphoton Rates with Quantum Memories. *Phys. Rev. Lett.* **110**, 133601 (2013).

[112] Bennett, C. H. & Brassard, G. Quantum cryptography: Public key distribution and coin tossing. In *IEEE International Conference on Computers, Systems and Signal Processing*, vol. 1, 175–179 (IEEE, Bangalore India, 1984).

[113] Fisher, K. A. G. *et al.* Quantum computing on encrypted data. *Nature Communications* **5** (2014).

[114] Yuan, Z. *et al.* 10-Mb/s Quantum Key Distribution. *Journal of Lightwave Technology* **36**, 3427–3433 (2018).

[115] This is not a master piece but a DPhil thesis.

[116] Boyd, R. W. *Nonlinear optics* (Academic Press, Amsterdam, 2008), 3rd ed edn.

[117] Spring, J. B. *Single Photon Generation and Quantum Computing with Integrated Photonics*. Doctor of Philosophy, University of Oxford (2014).

[118] U'Ren, A. B. *Multi-Photon State Engineering for Quantum Information Processing Applications*. Doctor of Philosophy, University of Rochester (2004).

[119] Quesada, N. & Sipe, J. E. Why you should not use the electric field to quantize in nonlinear optics. *Opt. Lett., OL* **42**, 3443–3446 (2017).

[120] Christ, A., Brecht, B., Mauerer, W. & Silberhorn, C. Theory of quantum frequency conversion and type-II parametric down-conversion in the high-gain regime. *New Journal of Physics* **15**, 053038 (2013).

[121] Quesada, N. & Sipe, J. E. Effects of time ordering in quantum nonlinear optics. *Physical Review A* **90**, 063840 (2014).

[122] Loudon, R. & Knight, P. Squeezed Light. *Journal of Modern Optics* **34**, 709–759 (1987).

[123] Armstrong, J. A., Bloembergen, N., Ducuing, J. & Pershan, P. S. Interactions between light waves in a nonlinear dielectric. *Physical Review* **127**, 1918 (1962).

[124] Dosseva, A., Cincio, . & Braczyk, A. M. Shaping the joint spectrum of down-converted photons through optimized custom poling. *Phys. Rev. A* **93**, 013801 (2016).

[125] Rogers, H. L. *Direct UV-written Bragg gratings for waveguide characterisation and advanced applications*. Doctor of Philosophy, University of Southampton (2013).

[126] Malitson, I. H. Interspecimen Comparison of the Refractive Index of Fused Silica. *J. Opt. Soc. Am., JOSA* **55**, 1205–1209 (1965).

[127] Koechner, W. *Solid-State Laser Engineering* (Springer, New York, 2006), 6th edn.

[128] U'Ren, A. B., Silberhorn, C., Erdmann, R., Banaszek, K., Grice, W. P., Walmsley, I. A. & Raymer, M. G. Generation of pure-state single-photon wavepackets by conditional preparation based on spontaneous parametric downconversion. *Laser Physics* **15**, 146–161 (2005).

[129] Garay-Palmett, K. *et al.* Photon pair-state preparation with tailored spectral properties by spontaneous four-wave mixing in photonic-crystal fiber. *Opt. Express, OE* **15**, 14870–14886 (2007).

[130] Law, C. K., Walmsley, I. A. & Eberly, J. H. Continuous frequency entanglement: effective finite Hilbert space and entropy control. *Physical Review Letters* **84**, 5304 (2000).

[131] Christ, A., Laiho, K., Eckstein, A., Cassemiro, K. N. & Silberhorn, C. Probing multimode squeezing with correlation functions. *New Journal of Physics* **13**, 033027 (2011).

[132] Brown, R. H. & Twiss, R. Q. Correlation between Photons in two Coherent Beams of Light. *Nature* **177**, 27 (1956).

[133] Glauber, R. J. The Quantum Theory of Optical Coherence. *Phys. Rev.* **130**, 2529–2539 (1963).

[134] Tapster, P. R. & Rarity, J. G. Photon statistics of pulsed parametric light. *Journal of Modern Optics* **45**, 595–604 (1998).

[135] Mauerer, W., Avenhaus, M., Helwig, W. & Silberhorn, C. How colors influence numbers: Photon statistics of parametric down-conversion. *Phys. Rev. A* **80**, 053815 (2009).

[136] Hong, C. K., Ou, Z. Y. & Mandel, L. Measurement of subpicosecond time intervals between two photons by interference. *Physical Review Letters* **59**, 2044 (1987).

[137] Legero, T., Wilk, T., Kuhn, A. & Rempe, G. Time-resolved two-photon quantum interference. *Appl. Phys. B* **77**, 797–802 (2003).

[138] Metcalf, B. J. *Silica-on-silicon waveguide circuits and superconducting detectors for integrated quantum information processing.* Doctor of Philosophy, University of Oxford (2014).

[139] Chen, L.-K. *et al.* Observation of ten-photon entanglement using thin BiB_3O_6 crystals. *Optica, OPTICA* **4**, 77–83 (2017).

[140] Collins, M. J. *et al.* Integrated spatial multiplexing of heralded single-photon sources. *Nature Communications* **4**, 2582 (2013).

[141] Mendoza, G. J. *et al.* Active temporal and spatial multiplexing of photons. *Optica, OPTICA* **3**, 127–132 (2016).

[142] Francis-Jones, R. J. A., Hoggarth, R. A. & Mosley, P. J. All-fiber multiplexed source of high-purity single photons. *Optica, OPTICA* **3**, 1270–1273 (2016).

[143] Shapiro, J. H. & Wong, F. N. On-demand single-photon generation using a modular array of parametric downconverters with electro-optic polarization controls. *Opt. Lett., OL* **32**, 2698–2700 (2007).

[144] Xiong, C. *et al.* Active temporal multiplexing of indistinguishable heralded single photons. *Nature Communications* **7**, 10853 (2016).

[145] Makino, K., Hashimoto, Y., Yoshikawa, J.-i., Ohdan, H., Toyama, T., van Loock, P. & Furusawa, A. Synchronization of optical photons for quantum information processing. *Science Advances* **2**, e1501772–e1501772 (2016).

[146] Hoggarth, R. A., Francis-Jones, R. J. A. & Mosley, P. J. Resource-efficient fibre-integrated temporal multiplexing of heralded single photons. *J. Opt.* **19**, 125503 (2017).

[147] Kaneda, F. & Kwiat, P. G. High-efficiency single-photon generation via large-scale active time multiplexing. *Science Advances* **5**, eaaw8586–eaaw8586 (2019).

[148] Grimau Puigibert, M. *et al.* Heralded Single Photons Based on Spectral Multiplexing and Feed-Forward Control. *Phys. Rev. Lett.* **119**, 083601 (2017).

[149] Joshi, C., Farsi, A., Clemmen, S., Ramelow, S. & Gaeta, A. L. Frequency multiplexing for quasi-deterministic heralded single-photon sources. *Nature Communications* **9**, 847 (2018).

[150] Kato, K. Parametric oscillation at 3.2 mu;m in KTP pumped at 1.064 mu;m. *IEEE Journal of Quantum Electronics* **27**, 1137–1140 (1991).

[151] Gurzadian, G. G. *Handbook of nonlinear optical crystals.* Springer series in optical sciences ; v. 64 (Springer, Berlin ; London, 1997), 2nd, rev. and updated ed. edn.

[152] Avenhaus, M., Eckstein, A., Mosley, P. J. & Silberhorn, C. Fiber-assisted single-photon spectrograph. *Opt. Lett., OL* **34**, 2873–2875 (2009).

[153] Cumming, R. The Serrodyne Frequency Translator. *Proceedings of the IRE* **45**, 175–186 (1957).

[154] Davis, A. O. C., Saulnier, P. M., Karpiski, M. & Smith, B. J. Pulsed single-photon spectrometer by frequency-to-time mapping using chirped fiber Bragg gratings. *Opt. Express, OE* **25**, 12804–12811 (2017).

[155] Wright, L. J., Karpiski, M., Söller, C. & Smith, B. J. Spectral Shearing of Quantum Light Pulses by Electro-Optic Phase Modulation. *Phys. Rev. Lett.* **118**, 023601 (2017).

[156] Aull, B. F., Loomis, A. H., Young, D. J., Heinrichs, R. M., Felton, B. J., Daniels, P. J. & Landers, D. J. Geiger-mode avalanche photodiodes for three-dimensional imaging. *Lincoln Laboratory Journal* **13**, 335–349 (2002).

[157] Natarajan, C. M., Tanner, M. G. & Hadfield, R. H. Superconducting nanowire single-photon detectors: physics and applications. *Supercond. Sci. Technol.* **25**, 063001 (2012).

[158] Engel, A., Renema, J. J., Ilin, K. & Semenov, A. Detection mechanism of superconducting nanowire single-photon detectors. *Supercond. Sci. Technol.* **28**, 114003 (2015).

[159] Marsili, F. *et al.* Detecting single infrared photons with 93% system efficiency. *Nature Photonics* **7**, 210–214 (2013).

[160] Anant, V., Kerman, A. J., Dauler, E. A., Yang, J. K. W., Rosfjord, K. M. & Berggren, K. K. Optical properties of superconducting nanowire single-photon detectors. *Opt. Express, OE* **16**, 10750–10761 (2008).

[161] Dauler, E. A. *et al.* Photon-number-resolution with sub-30-ps timing using multi-element superconducting nanowire single photon detectors. *Journal of Modern Optics* **56**, 364–373 (2009).

[162] Bourdeauducq, S. A 26 ps RMS time-to-digital converter core for Spartan-6 FPGAs. *arXiv:1303.6840 [physics]* (2013).

[163] Tiedau, J. *Frequency Multiplexing for Heralded Single Photon Generation.* Master's Thesis, Leibniz Universität Hannover, Institut für Quantenoptik (2015).

[164] Riaziat, M., Virshup, G. & Eckstein, J. Optical wavelength shifting by traveling-wave electrooptic modulation. *IEEE Photonics Technology Letters* **5**, 1002–1005 (1993).

[165] Alferness, R. C. Waveguide Electrooptic Modulators. *IEEE Transactions on Microwave Theory and Techniques* **30**, 1121–1137 (1982).

[166] Gordon, J. P. Theory of the soliton self-frequency shift. *Optics Letters* **11**, 662 (1986).

[167] Santhanam, J. & Agrawal, G. P. Raman-induced spectral shifts in optical fibers: general theory based on the moment method. *Optics Communications* **222**, 413–420 (2003).

[168] Eckstein, A. *et al.* High-resolution spectral characterization of two photon states via classical measurements. *Laser & Photonics Reviews* **8**, L76–L80 (2014).

[169] Clements, W. R. *Components and Applications of Linear Quantum Optics.* Doctor of Philosophy, University of Oxford (2018).

[170] Klyshko, D. N. Utilization of vacuum fluctuations as an optical brightness standard. *Sov. J. Quantum Electron.* **7**, 591 (1977).

[171] Beck, M. Comparing measurements of $g^{(2)}(0)$ performed with different coincidence detection techniques. *J. Opt. Soc. Am. B, JOSAB* **24**, 2972–2978 (2007).

[172] Migdall, A., Polyakov, S., Fan, J. & Bienfang, J. (eds.) *Single-photon generation and detection: experimental methods in the physical sciences.* No. volume 45 in Experimental methods in the physical sciences (Elsevier/AP, Academic Press is an imprint of Elsevier, 2013). OCLC: ocn844308244.

[173] Ma, X.-S., Zotter, S., Kofler, J., Jennewein, T. & Zeilinger, A. Experimental generation of single photons via active multiplexing. *Phys. Rev. A* **83**, 043814 (2011).

[174] Meany, T. *et al.* Hybrid photonic circuit for multiplexed heralded single photons. *Laser & Photonics Reviews* **8**, L42–L46 (2014).

[175] Garay-Palmett, K., Jeronimo-Moreno, Y. & URen, A. B. Theory of cavity-enhanced spontaneous four wave mixing. *Laser Phys.* **23**, 015201 (2013).

[176] Posner, M. T. *Optical integrated circuits for large-scale quantum networks - ePrints Soton.* Doctoral, University of Southampton, University of Southampton (2017).

[177] Politi, A., Matthews, J., Thompson, M. & O'Brien, J. Integrated Quantum Photonics. *IEEE Journal of Selected Topics in Quantum Electronics* **15**, 1673–1684 (2009).

[178] Agrawal, G. P. *Nonlinear Fiber Optics* (Academic Press, San Diego, 2001), 3rd edn.

[179] Adikan, F. *Direct UV-Written Waveguide Devices.* Doctor of Philosophy, University of Southampton (2007).

[180] Hiemstra, T. *Integrated Sources of Pure Single Photons at Telecommunication Wavelengths.* Master's thesis, Technische Universität Darmstadt (2014).

[181] Posner, M. T. *et al.* High-birefringence direct UV-written waveguides for use as heralded single-photon sources at telecommunication wavelengths. *Opt. Express, OE* **26**, 24678–24686 (2018).

[182] Vaccaro, L., Cannas, M. & Boscaino, R. Luminescence features of nonbridging oxygen hole centres in silica probed by site-selective excitation with tunable laser. *Solid State Communications* **146**, 148–151 (2008).

[183] Poem, E., Hiemstra, T., Eckstein, A., Jin, X.-M. & Walmsley, I. A. Free-space spectro-temporal and spatio-temporal conversion for pulsed light. *Optics Letters* **41**, 4328 (2016).

[184] Lita, A. E., Miller, A. J. & Nam, S. W. Counting near-infrared single-photons with 95% efficiency. *Optics express* **16**, 3032–3040 (2008).

[185] Miller, A. J., Nam, S. W., Martinis, J. M. & Sergienko, A. V. Demonstration of a low-noise near-infrared photon counter with multiphoton discrimination. *Applied Physics Letters* **83**, 791 (2003).

[186] Miller, A. J., Lita, A. E., Calkins, B., Vayshenker, I., Gruber, S. M. & Nam, S. W. Compact cryogenic self-aligning fiber-to-detector coupling with losses below one percent. *Optics express* **19**, 9102–9110 (2011).

[187] Humphreys, P. C. *et al.* Tomography of photon-number resolving continuous-output detectors. *New J. Phys.* **17**, 103044 (2015).

[188] Kasap, S. & Capper, P. *Springer handbook of electronic and photonic materials* (Springer, New York; London, 2006).

[189] Fulconis, J., Alibart, O., OBrien, J. L., Wadsworth, W. J. & Rarity, J. G. Nonclassical Interference and Entanglement Generation Using a Photonic Crystal Fiber Pair Photon Source. *Physical Review Letters* **99** (2007).

[190] Francis-Jones, R. J. A. & Mosley, P. J. Characterisation of longitudinal variation in photonic crystal fibre. *Opt. Express, OE* **24**, 24836–24845 (2016).

[191] Kimble, H. J. The quantum internet. *Nature* (2008).